Lorentz Force Velocimetry at High Magnetic Reynolds Numbers

Dissertation

zur Erlangung des akademischen Grades

Doktoringenieur
(Dr.-Ing.)

vorgelegt der
Fakultät für Maschinenbau der
Technischen Universität Ilmenau

von Herrn
M.Sc. Igor Sokolov

geboren am 13.06.1989 in Nowosibirsk, Russland

Datum der Einreichung: 09.11.2015
Datum der wissenschaftlichen Aussprache: 25.02.2016

1. Gutachter: Prof. Dr. André Thess
2. Gutachter: Prof. Dr. Jörg Schumacher
3. Gutachter: Prof. Dr. Peter Frick

urn:nbn:de:gbv:ilm1-2016000172

Kurzfassung

Die Lorentzkraft-Anemometrie (LKA) ist ein berührungsloses elektromagnetisches Strömungsmessverfahren. Das Grundprinzip dieses Verfahrens kann wie folgt beschrieben werden: befindet sich ein Magnet in der Nähe einer sich bewegenden, elektrisch leitfähigen Flüssigkeit so erfährt dieser die Lorentzkraft. Diese Kraft ist von der Strömungsgeschwindigkeit der Flüssigkeit linear abhängig. Da dieses Messverfahren berührungslos ist, ist es gut geeignet für industrielle Anwendungen wo mit heißen und aggressiven Metallenschmelzen gearbeitet wird. Dennoch gibt es einen grundsätzlichen physikalischen Effekt der bei hohen magnetischen Reynoldszahlen Re_m auftritt und den Anwendungsbereich einschränkt. Dieser Effekt äußert sich zum Beispiel dadurch, dass das vom Magneten erzeugte Magnetfeld verzerrt wird, wenn die Strömungsgeschwindigkeit der Flüssigkeit hoch ist. Dadurch ist der Zusammenhang zwischen Kraft und Geschwindigkeit nicht mehr linear und es kommt zu Meßfehlern. Das Ziel der Promotion besteht darin, die grundsätzlichen Aspekte dieses physikalischen Effektes theoretisch und experimentell zu untersuchen und zu beschreiben. Somit wird auch eine wichtige Voraussetzung geschaffen, die es ermöglicht, das Anwendungsspektrum des LKA-Verfahrens zukünftig zu erweitern. Die vorliegende Arbeit besteht aus fünf Kapiteln. Im ersten Kapitel werden eine Einführung zur Thematik gegeben und die wesentlichen Aspekte des LKA-Verfahrens bei mittleren Werten für Re_m erläutert. Im darauffolgenden Kapitel wird ein theoretisches quasi-2D Modell entwickelt, welches die Erzeugung der Lorentzkraft in einem elektrisch leitfähigen Festkörper veranschaulicht. Im dritten Kapitel werden die dazugehörigen Modellexperimente mit metallischen Festkörpern beschrieben und die dazugehörigen Messergebnisse analysiert. Das vierte Kapital umfaßt Versuche mit flüssigem Natrium das mit Geschwindigkeiten von bis zu 30 m/s am Magneten vorbeiströmt. Derartige Experimente zur Lorentzkraft-Anemometrie wurden weltweit erstmalig durchgeführt. Bei den Versuchen wurden die Lorentzkraft und das Magnetfeld lokal gemessen. Die Ergebnisse bilden eine wichtige Grundlage für zukünftige Anwendungen des LKA-Verfahrens und komplementieren die gesammelten Erfahrungen zu dieser Technologie bei niedrigen magnetischen Reynoldszahlen. Im letzten Kapital werden die Ergebnisse der Arbeit zusammengefaßt.

Abstract

Lorentz force velocimetry is a contactless velocity measurement technique. The main idea behind this method can be expressed as follows: a magnet which is placed near a moving conducting fluid experiences the Lorentz force which is proportional to the conductor velocity. Since such measurements are non-intrusive they are especially appealing for industrial applications where people deal with hot and aggressive liquid metal flows. However, there is a fundamental restriction which limits an application area of the Lorentz force velocimetry. The restriction stems from the fact that at high velocities the magnetic field imposed by the magnet is expelled from the conducting media. As a result, the linear dependence of the Lorentz force on velocity is violated that leads to measurement errors. The aim of this work is to reveal fundamental aspects of the problems of this kind by conducting theoretical and mainly experimental research.

The thesis consists of five main chapters. In the first one the topic of magnetohydrodynamics is introduced to a reader as well as the nuances of the Lorentz force velocimetry at finite magnetic Reynolds numbers Re_m are explained. Next chapter presents a theoretical approach where the quasi-two dimensional model of the Lorentz force generation in a conducting slab is developed. The third chapter is concerned with the modeling experiment where a liquid metal flow is substituted with conducting solid rods. The results prove that if the magnetic field evolution is mainly controlled by advection, it leads to the statistical error in the Lorentz force measurements. The fourth chapter embraces the most important part of the work - experiments with a high-speed liquid sodium flow. Here for the first time the Lorentz force velocimetry was applied to study the flow whose velocity reaches 30 m/s. The experiment comprises both Lorentz force measurements and induced magnetic field measurements. Remarkably, a strong non-linear magnetic field expulsion was observed at $Re_m > 4$. These data go in accordance with the Lorentz force saturation that occurs also at $Re_m \approx 4$. This study forms the basis of the Lorentz force velocimetry of the future and complements well already gained experience of measurements at low magnetic Reynolds numbers. The last chapter stresses the most important achievements in the actual research.

Contents

93 pages, 65 figures, 6 tables.

1 Introduction

> *An expert is a person who has made all the mistakes that can be made in a very narrow field.*
>
> – Niels Henrik David Bohr

This work addresses a problem of the Lorentz force velocimetry application at non-stationary and high speed conducting flows. We use theoretical and experimental approaches to study the relation between the Lorentz force and the induced magnetic field. This link is proved to play a key role in the Lorentz force effects when the magnetic Reynolds number becomes finite or high.

1.1 Short introduction into magnetohydrodynamics

There are many ways to define the word *magnetohydrodynamics*. Here we go for the following definition: magnetohydrodynamics (MHD) is the study of mutual interaction between magnetic field and electrically conducting fluid. In other words, we consider a conductor at any state of matter that moves through any magnetic field. The best way to anchor these words to a mathematical background is to recall a simplified form of the Ohm's law [1]

$$\vec{j} = \sigma(\vec{\varepsilon} + \vec{V} \times \vec{B}) \tag{1}$$

Here $\vec{j}$ stands for the electrical current density, $\vec{\varepsilon}$ is the electrical field density, $\vec{V}$ is the conductor velocity and $\vec{B}$ denotes the magnetic field. The $\vec{V} \times \vec{B}$ term plays a key role in MHD because it gives rise to electrical currents in a conducting media. These currents interact with the applied field and generate their own magnetic fields, they can affect a fluid motion or change the energy balance of a system. All that leads to a fascinating game between currents, fields and velocities making MHD tasks very interesting to study. Indeed, magnetohydrodynamics phenomena can be widely observed in Nature and in different engineering applications. Here we touch upon just a few of them.

Magnetohydrodynamics in Nature:

- *Accretion disks.* MHD plays a central role in transport of angular momentum and mass in accretion disks which surround nuclei of active galaxies [2]. Such disks emit jets along their polar axes (fig.1a). This phenomena is still not well understood.

- *The Sun.* Our Sun is a brilliant example of an extremely complicated MHD system. Although the history of the solar physics research began 4000 years ago [3], it has a lot of open questions nowadays.

- *Magnetic field of the Earth.* Now it is well-known that the Earth is not a permanent magnet because the temperature inside it is above the Curie point [4]. The field is generated through convective flows of iron alloys in the outer core. This phenomenon is called *geomagnetic dynamo* and is being now actively investigated.

Magnetohydrodynamics in engineering applications:

- *MHD-stirring.* If there is a hot liquid metal alloy which has a non-uniform density distribution, all density gradients can be removed by stirring using a rotating magnetic field [4].
- *MHD-propulsion.* The product $\vec{V} \times \vec{B}$ gives rise to the Lorentz force $\vec{j} \times \vec{B}$ which can be used to propel ships and spacecrafts [5]. These engines are promising since they do not have moving parts.
- *Electromagnetic flow measurements.* Motion of a conducting flow inside a channel in a magnetic field results in a potential difference at the channel walls [6]. By measuring this difference once can straightforwardly obtain a flow rate.
- *MHD-weapon.* Surprisingly, the principles of magnetohydrodynamics can be used to build a weapon [7]. The Lorentz force $\vec{j} \times \vec{B}$ can accelerate bodies up to 10 km/s if the current density $\vec{j}$ is high enough (fig.1b).

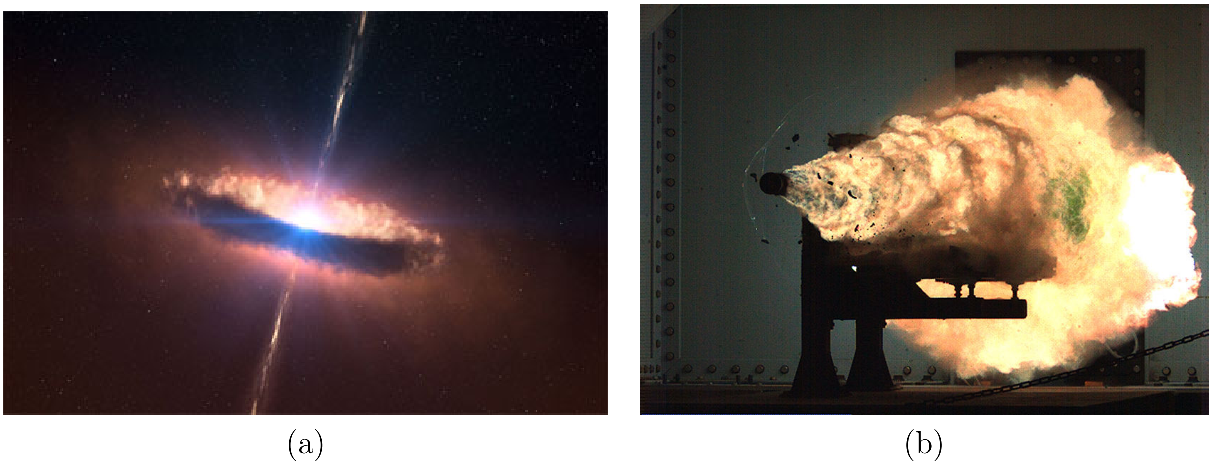
(a) (b)

Figure 1: MHD phenomena in Nature and in engineering applications: (a) a jet of the accretion disk in space (courtesy of ESO, L. Calcada and M. Kornmesser); (b) "railgun" testing in Naval Surface Warfare Center in January 2008 (courtesy of U.S. Navy).

In spite of the fact that MHD can be found in a wide variety of fields, all of them can be characterized by a set of dimensionless parameters (which will be defined in Chapter 2): Reynolds number Re, Interaction parameter N, Hartmann number Ha, Lundquist number Lu, magnetic Reynolds number Re_m and many others. The parameter Re_m is of great importance for the current work.

1.2 Magnetohydrodynamics at high magnetic Reynolds numbers

Like heat or vorticity, magnetic field has two mechanisms of propagation. The first one is diffusion. It means that one can not switch the field on instantaneously in a media. After it is imposed on boundaries, it starts to diffuse towards material with a certain speed. The second mechanism is advection. In this case the field moves together with material as if it was frozen in it. Practically, both mechanisms drive the field at the same time and the ratio between magnetic field advection and magnetic field diffusion is represented by magnetic Reynolds number Re_m [8]. To give a reader a feeling about this parameter, a full range of Re_m values in Nature is shown in fig.2. Usually, it is either much less or much bigger than unity. Under laboratory or industrial conditions $Re_m \ll 1$. It means that the magnetic field evolution is completely governed by diffusion. In contrast, in space $Re_m \gg 1$ that points to advection dominated regimes.

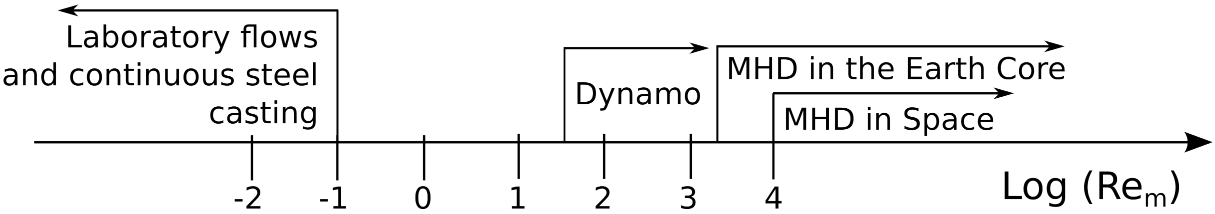

Figure 2: Range of Re_m values in Nature.

Another important physical interpretation of Re_m is connected with the *induced* magnetic fields. According to the Ohm's law (1), motion of a conductor through a transverse magnetic field gives rise to electrical current. Every current loop carries its own magnetic field [1], which is called the induced magnetic field b. Interestingly that a magnitude of b is directly connected with magnetic Reynolds number. The higher the Re_m, the stronger the induced fields. To be more precise, the ratio between induced and imposed magnetic fields approximately equals to Re_m. Although it is not true sometimes, people use this rule of thumb very often.

We say that the magnetic Reynolds number is high when $Re_m \gg 1$. Flows at such Re_m have big velocities and dimensions and therefore they are usually turbulent. The induced fields are so strong that they change the distribution of the imposed field inside and outside a conductor. In particular, the imposed field behaves as though it is frozen in a conducting media. In this case magnetic field lines are often compared with stretched strings. By the way, these strings as any other strings can oscillate and transmit energy [9]! The corresponding waves are called *Alfvén waves* and their generation is controlled by Lundquist number [10]. Although it is directly related to the topic of high Re_m flows, *Alfvén waves* are not considered here since they are of rather fundamental than engineering interest. A general question is what makes the magnetic field frozen? Through which mechanism does the flow drag the magnetic field lines? One way is to consider a predominance of advection over diffusion [8]. Diffusion works such that in time t the field goes $L_d \sim \sqrt{\lambda t}$. Here $\lambda = 1/\mu\sigma$ is the magnetic diffusivity and $\mu = 4\pi \cdot 10^{-7}\ H \cdot m^{-1}$ is the magnetic permeability of vacuum. For example, $\lambda \sim 1\ m^2/s$ for a typical liquid metal flow. A characteristic diffusion speed is limited whereas advection velocity is not. Consequently, for any conductivity of liquid metal there is a certain advection velocity at which diffusion becomes too slow and the field runs away with the flow. Another approach is to consider a direction of the strongest component of the induced magnetic field in a three-dimensional flow [6]. A product of $\vec{V} \times \vec{B}$ gives rise to electrical current $\vec{j}$ that carries the induced magnetic field $\vec{b}$. At $Re_m \gg 1$ the field $\vec{b}$ becomes very high and its strongest component coincides with the main flow direction. Therefore the substantial effect of bending takes place in the direction of $\vec{V}$.

Indeed, the majority of phenomena where $Re_m \gg 1$ occurs in astrophysics. But a general problem of high magnetic Reynolds numbers is important not only for MHD in galaxies, in the Sun and in the Earth core. For example, high-speed trains use high Re_m effects to reduce the drag force [11]. In some cases in industry the flow velocity changes fast and the error in velocity measurements due to the rapid change of the flow rate is also connected with the high value of Re_m. All in all, there are still a lot of unresolved engineering and fundamental issues. One of them concerns a method which is called Lorentz force velocimetry.

1.3 Lorentz force velocimetry at high magnetic Reynolds numbers

In 1832, M. Faraday tried for the first time to determine the velocity of the River Thames by measuring the voltage between two electrodes immersed in the river [12]. Although this attempt was unsuccessful, it opened the era of electromagnetic flow measurements giving rise to many rapidly developing methods. One of the state-of-the-art techniques is called *Lorentz force velocimetry (LFV)* [6, 13]. The principle of LFV is based on the fact that a magnet which is placed near a moving conductor experiences the Lorentz force. The key point is that this force is proportional to the conductor velocity:

$$F = k \cdot \sigma V B^2, \tag{2}$$

where σ stands for conductivity, V is the conductor velocity and B is the applied magnetic field. Since the exact analytical expression for the force does not exist, we incorporate the factor k. Basically, k feels all of the subtle measurement nuances keeping the formula (2) transparent for a reader. So, to built the simplest measurement system we need a magnet and a force sensor (fig.3). Looking ahead it is worth pointing out that under laboratory or industrial conditions a typical Lorentz force value varies in the range 10..100 mN. Nowadays there is a plenty of force sensors and data acquisition (DAQ) systems which allow engineers to successfully record signals of such amplitude. It is reasonable to point out the advantages and disadvantages of the LVF method:

Advantages:

- *The method is completely non-intrusive.* It means that there is no need to immerse a probe in a harsh environment disturbing the flow. This feature is especially appealing to industrial applications where operating conditions are extremely demanding.
- *No necessity for optical access to the flow.* The flow can be completely opaque because the role of a sensing probe is taken by the magnetic field that penetrates fluids with any transparency. This fact is used by scientists to study liquid metal flows where optical methods can not be applied.

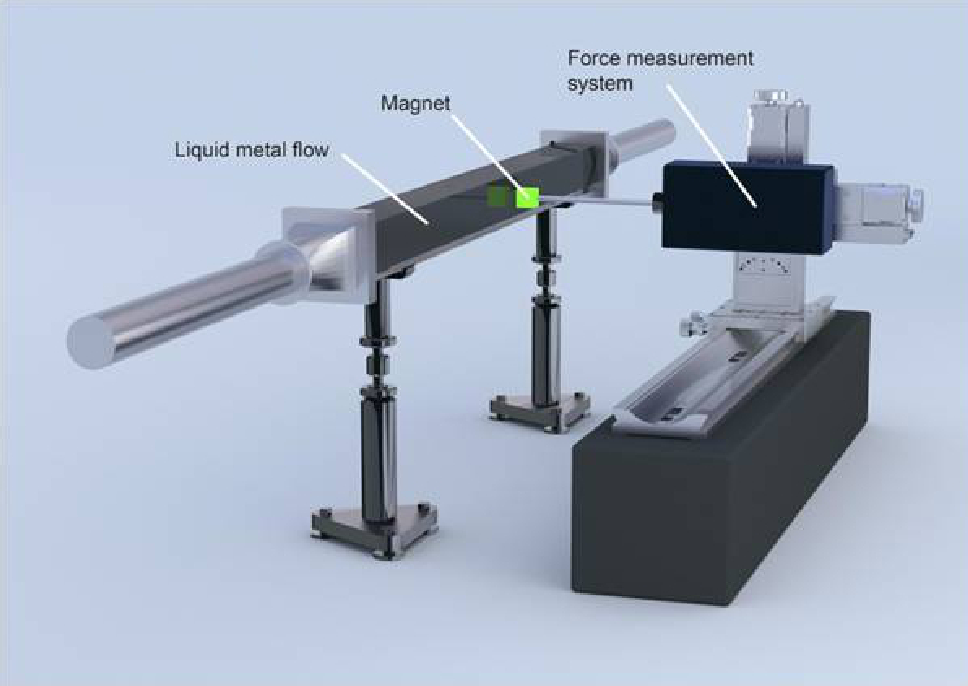

Figure 3: Simplified Lorentz force measurement system.

- *Linear dependence of the Lorentz force on velocity.* The linear law between velocity and force simplifies a device calibration. Some other methods like hot-wire anemometry lack this very nice feature [14].

- *Availability of the measurement system components.* Today there is a great choice of cheap magnets and force sensors on the market. For example, in PIV methods [15] it is necessary to buy a laser and a high-speed camera that increases expenditures on the measurement system.

Disadvantages:

- *The flow must be conductive.* Indeed, the higher the conductivity of the flow, the better LFV works. It can be seen from the Ohm's law (1) where a controlling parameter is conductivity.
  Comments: Generally speaking, it is a question of a force sensor resolution. Low conductivity will lead to a low Lorentz force. If the measurement system is very sensitive, it is possible to resolve really tiny forces. Recently LFV techniques have been developed to measure the velocity of water [16]!

- *No exact expression for the Lorentz force.* This problem stems from the fact that the factor k can not be analytically calculated. To do that one has to conduct non-contact simultaneous measurements of magnetic field and flow profile in a large volume. Even having all cutting-edge equipment nowadays this task is far from being easy.
  Comments: Usually k can be estimated by carrying out dry tests when a fluid flow is replaced by a solid bar with the same cross-section.

- *Strong dependence on temperature.* This problem is one of the most difficult ones to overcome. From (2) it is clear that the Lorentz force depends on the distance between magnet and flow. Once the distance is changed because of temperature expansion of housing materials, the force will be also affected. Even though the setup geometry can be kept unchanged, a variation of magnetic field because of a temperature change has to be also taken into account.
  Comments: To solve this problem a system with a dummy weight is installed in parallel with a real measuring system. Since both of them are equally affected by temperature, a desired signal can be extracted from two simultaneous measurements.

Despite all these problems several working prototypes of Lorentz force flowmeters have been developed [17]. The design concept is aimed to meet industrial conditions where pipe and open channel flows are frequently met (fig.4).

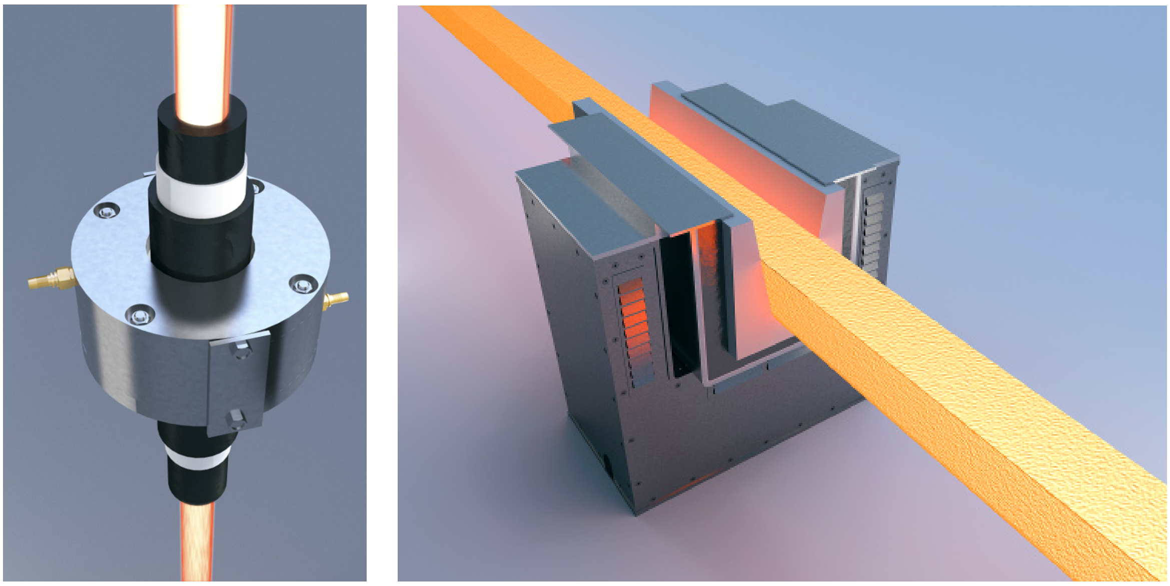

(a) (b)

Figure 4: Prototypes of Lorentz force flowmeters: (a) for a vertical pipe flow; (b) for a horizontal open channel flow.

The phenomena described in Section 1.2 lead to difficulties in application of LFV to high-speed flows. At small Re_m a conductor does not influence the imposed magnetic field (fig.5a). Once it diffused into a material, it does not evolve in time anymore unless one varies $\vec{B}$ at the boundaries. But if Re_m becomes moderate or high the situation changes dramatically (fig.5b). Due to a mutual interaction between $\vec{V}$ and $\vec{B}$, magnetic field lines start to bend towards direction of the flow. Moreover, the higher the velocity, the stronger the bending. Physically, fig.5b reflects the inability of magnetic field diffusion to recover the field to its initial unperturbed state because of a permanent advection by the flow. So, the key feature of LFV at high Re_m is that $\vec{B}$ *is altered by the conductor motion*, i.e. $\vec{B} = f(\vec{V})$. A linear change of $\vec{V}$ results in a non-linear change of $\vec{V} \times \vec{B}(V)$. This is a fundamental problem because magnetic field links the velocity of the fluid to the measured force. If the imposed magnetic field is changed, our tool stops working properly that causes difficulties in direct applications of LFV-methods to high-speed flows. Remarkably, not

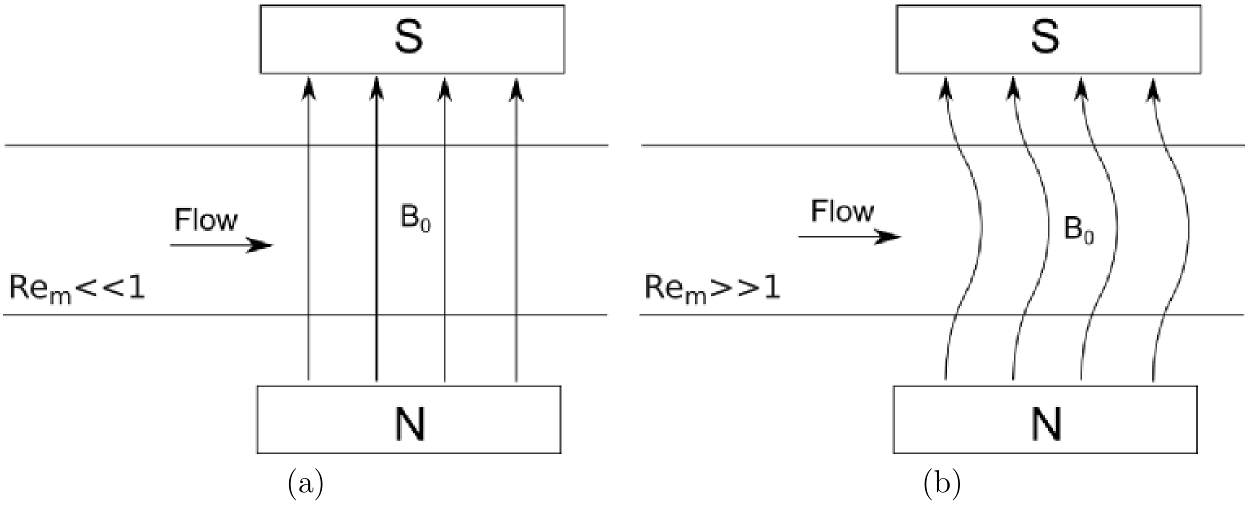

Figure 5: Difference between low Re_m and high Re_m flows: (a) the flow does not distort the imposed magnetic field if Re_m is small; (b) the imposed field is deformed because of the flow motion in case of high Re_m.

only affects the flow the magnetic field, but a reversal effect takes place. The reason is that the Lorentz force is a braking force and it brakes the flow non-uniformly because of a complex electrical currents distribution. Then a non-uniformly braked flow changes the imposed field distribution also in a complex way. That is to say, there is a mutual interaction between the magnetic field and the fluid flow that mathematically speaking results in $\vec{V}$-$\vec{B}$ coupling. This coupling can be resolved well neither analytically nor numerically that underlines the necessity of the experimental study.

1.4 Research objectives and hypotheses

The research objectives which result from our previous discussion can be summarized as follows:

1. To develop a theoretical model that describes Lorentz force response to a transient velocity input at finite Re_m taking into account the bending of the imposed magnetic field. The model should address the cases of a stepwise velocity signal, an exponential velocity signal and oscillatory motion.

2. To conduct experiments where the influence of high Re_m effects on the Lorentz force generation in solid aluminium and copper rods is modeled. To show that in this case the velocity of the rods should change faster than a characteristic magnetic field diffusion time.

3. To link the observed dynamics of the Lorentz force in solid conductors at $Re_m > 1$ with imposed field sweeping by measuring the induced magnetic field in the vicinity of the rods.

4. To set up an experiment where the Lorentz force velocimetry is applied to a high-speed liquid sodium flow at $Re_m \gg 1$. To perform simultaneous measurements of the flow velocity, the Lorentz force and the induced magnetic field in order to prove that the linear relationship between the force and the velocity is not valid at $Re_m > 1$. Apart from that, to show that this deviation from the linear dependence is explained by the magnetic field expulsion.

The following hypotheses are proved in the work:

1. A problem of the Lorentz force response to a velocity signal in solid conductors at finite Re_m is mathematically equivalent to the quasi-two dimensional heat diffusion problem with time-varying boundary conditions. The developed model gives an accurate prediction of the Lorentz force signal in case of non-stationary conductor motion while considering magnetic field lines bending.

2. Effects of high Re_m take place in a solid conductor when its velocity changes faster than a characteristic magnetic field diffusion time. In such cases the Lorentz force measurements suffer from the additional systematic error that stems from the predominance of advection over diffusion in the magnetic field evolution. In particular, not only has the Lorentz force the reduced values in comparison to low Re_m cases, but it also reacts faster to the velocity change.

3. The method of the Lorentz force velocimetry can be used in order to measure the velocity of a non-stationary turbulent liquid metal flow at high Re_m. In experiments with liquid sodium, the dependence of the Lorentz force on sodium velocity deviates from the linear law at $Re_m > 4$. This fact is directly connected with the magnetic field expulsion that results in the non-linear relationship between the induced and the imposed magnetic fields.

2 Theoretical study of the Lorentz force response

2.1 MHD equations and dimensionless parameters

Before undertaking an experiment it is always reasonable to conduct a theoretical study of the problem. The interaction between a magnetic field and a fluid flow is described by a system of four non-dimensionalized equations [10]:

$$\nabla \cdot \vec{V} = 0 \tag{3}$$

$$\nabla \cdot \vec{B} = 0 \tag{4}$$

$$\frac{D\vec{V}}{Dt} = -\nabla P + \frac{1}{Re}\Delta \vec{V} + N\vec{j} \times \vec{B} \tag{5}$$

$$\frac{\partial \vec{B}}{\partial t} = \nabla \times (\vec{V} \times \vec{B}) + \frac{1}{Re_m}\Delta \vec{B} \tag{6}$$

Here $D/Dt = \partial/\partial t + \vec{V} \cdot \nabla$ stands for the substantial derivative. Equations (3) and (4) state that considered flow is incompressible and that magnetic field is solenoidal, i.e. the total magnetic flux through a closed surface is zero. Equation (5) is the well-known *Navier-Stokes* equation for incompressible fluid with additional Lorentz force term. It tells us how velocity field $\vec{V}$ evolves in time if the flow is driven by the pressure gradient ∇P in the presence of the Lorentz force $\vec{j} \times \vec{B}$. Electrical current $\vec{j}$ can be either induced according to the Ohm's law (1) or externally applied. Equation (6) is the magnetic field transport equation. It describes how magnetic field imposed on a moving conductor changes in time by advection (first term on the right) and diffusion (second term on the right). The last two equations are controlled by three nondimensional parameters. The first parameter is Reynolds number which shows the ratio between inertia and viscous forces:

$$Re = \frac{VL}{\nu}, \tag{7}$$

where ν is the kinematic viscosity, L and V are characteristic length and velocity correspondingly. Basically, high value of Re points to a turbulent regime. For example, it is widely admitted for a pipe flow that at $Re \lesssim 2100$ the flow is still laminar and at $Re > 4000$ the flow is fully turbulent [18]. In other types of flows a threshold value of Re can vary but the tendency is always the same. If the fluid velocity is small, the pressure gradient (e.g. created by a pump) simply drives the flow keeping all hydrodynamic perturbations very small. An increase of the pressure gradient makes velocity higher and higher and there is always a moment when the flow structure becomes chaotic by creating turbulent vortices. Thereby an excessive amount of energy is dissipated. The second controlling parameter is called *Stuart* number or interaction parameter:

$$N = \frac{\sigma B^2 L}{\rho V}, \tag{8}$$

where ρ is the conductor density and σ is the conductivity. The interaction parameter shows how big is magnetic energy compared to kinetic energy of the flow. If $N >> 1$ then the imposed field impacts on the velocity field dramatically, if $N << 1$ then the flow does not "feel" the field at all. And the third dimensionless group which was introduced in Chapter 1 is magnetic Reynolds number Re_m defined as:

$$Re_m = \mu\sigma VL \approx \frac{b}{B_0} \tag{9}$$

The physics hidden behind Re_m was already discussed. Once again, the magnetic Reynolds number shows how strong the magnetic field advection is compared to the magnetic field diffusion. At the same time, it shows how big the induced field b is in comparison to the imposed B_0. The last statement is valid only if $Re_m \ll 1$ and the reason is the following. To estimate $\vec{b}$ one has to refer to the Ampere's law [1], which links the electrical (or eddy) current to the field that it carries:

$$\mu\vec{j} = \nabla \times \vec{b} \tag{10}$$

Eddy currents can be calculated using the Ohm's law (1), where $\vec{j} \sim \sigma\vec{V} \times \vec{B}_0$. But if $Re_m >> 1$ the imposed field B_0 runs away with the flow. More generally, the higher the Re_m the less it makes sense to relate any field to B_0 [10].

So, (5) and (6) describe the mutual interaction between the flow and the magnetic field. It is sensible to describe this interaction step by step:

1. First of all, $\vec{V} \times \vec{B}_0$ leads to eddy current growth according to the Ohm's law (1)
2. Then, eddy currents give rise to the induced magnetic field $\vec{b}$ according to the Ampere's law (10)
3. The interaction between the total field and the eddy currents results in the Lorentz force $\vec{j} \times (\vec{B}_0 + \vec{b})$
4. The Lorentz force brakes the flow by reducing $\vec{V}$ and everything starts from the beginning until equilibrium is achieved.

It is very difficult to obtain analytical solutions for (5) and (6) because they form a coupled system of non-linear partial differential equations. It means that there is a need to simplify them. First of all, instead of a fluid flow we will consider a solid metal bar as a conductor. This simplifies the whole picture significantly because in that case we have no turbulence and the velocity field $\vec{V}$ is uniform. Secondly, let us assume that we can keep the velocity of the bar constant in spite of the braking Lorentz force. These two assumptions allow us not to consider (5) at all since $\vec{V}$ is given and totally controlled. As for the imposed field $\vec{B}_0$, it is uniform and also known. So, on the one hand we can not study turbulence in this approach, but on the other hand we can focus our attention on (6). The final remark is that our model will be quasi-two-dimensional. Although it might seem to be far-fetched, looking ahead one can say that there is a good agreement with experiments. It means that the model is simple enough to be solved analytically and is not too simple to give wrong unrealistic results. For convenience, we list all simplifications here:

- Specified uniform velocity field, no turbulence
- Specified uniform imposed magnetic field
- Quasi-2D model

2.2 Problem definition

The model is shown in fig.6. We assume a laterally infinite plate with thickness D. The plate is electrically conducting and its electrical conductivity is σ. An externally applied uniform magnetic field B_0 penetrates the plate. For $t < 0$ the plate is at rest and at time $t = 0$ the plate starts moving with a time-dependent velocity $V(t)$. We will consider 3 different cases. First of all, when the velocity is constant and equals to V_0 for $t > 0$. Then we will investigate the more general case when the plate is smoothly accelerated and reaches its asymptotic (constant) velocity V_0 for $t \to \infty$. And finally, we will discuss the problem, where the velocity changes periodically, i.e. $V(t) \sim cos(\omega t)$. The goal is to determine the Lorentz force $F(t)$ in $[N/m^2]$ and the Joule heat $Q(t)$ in $[W/m^2]$ generated inside the plate.

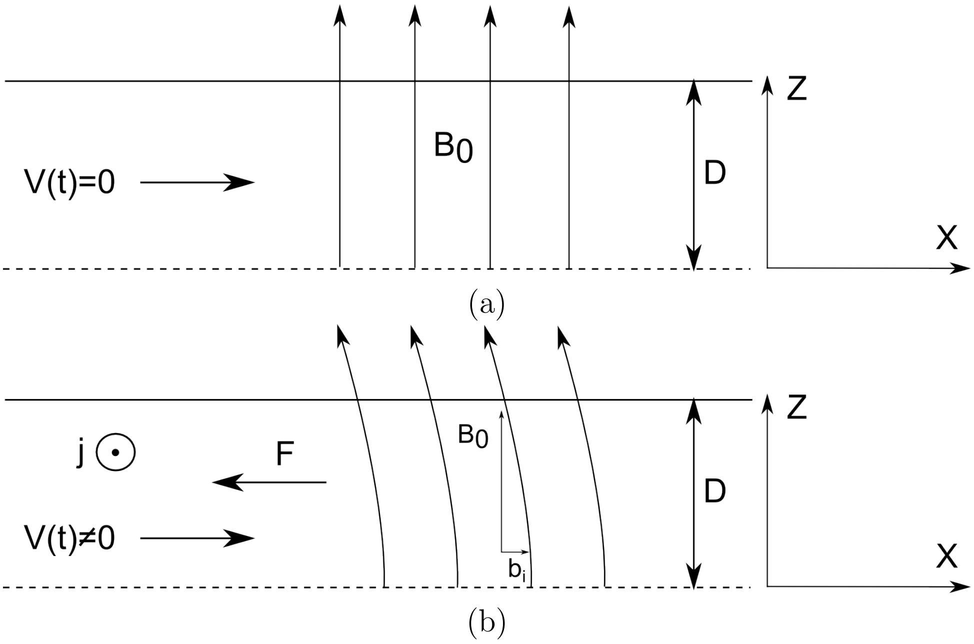

Figure 6: Definition of the model: interaction of a laterally unbounded electrically conducting plate with a homogeneous magnetic field B_0. Due to the symmetry a half of the plane is considered only. If the plate experiences no motion, the applied magnetic field B_0 is not distorted (a). In case of non-zero velocity, eddy currents j ensue that leads to a primary magnetic field disturbance by the induced magnetic field b. An interaction between the induced magnetic field and eddy currents gives rise to the Lorenz force F which opposes the flow (b).

Before considering (6), one has to note that velocity of the plate is non-dimensionalized by V_0, the space coordinate is referred to the thickness of the plate D and extends for symmetry reasons from $z = 0$ to $z = 1$. The time coordinate t is referred to the magnetic diffusion time $\tau_{diff} = \mu\sigma D^2$ as a characteristic time scale and $Re_m B_0$ is used to non-dimensionalize the induced magnetic field b. The reference values for F and Q are $\sigma D V_0 B_0^2$ and $\sigma^2 D V_0^2 B_0^2$ correspondingly. For convenience a complete list of reference parameters is shown in Table 1.

Physical value	Reference value	Description
$V, m/s$	V_0	Plate velocity
z, m	D	Plate thickness
t, s	$\mu\sigma D^2$	Diffusion time
b, T	$Re_m B_0$	Induced magnetic field
$F, N/m^2$	$\sigma D V_0 B_0^2$	Lorentz force per unit area
$Q, W/m^2$	$\sigma^2 D V_0^2 B_0^2$	Joule heat per unit area

Table 1: Reference parameters which are used in the current theoretical model.

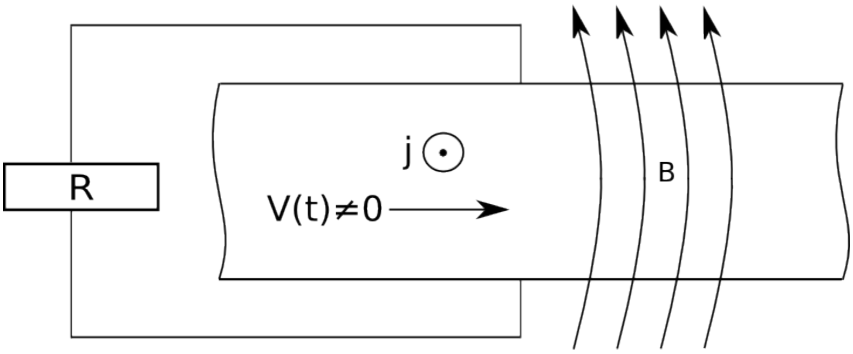

Figure 7: Current closing through an imaginary resistor.

One more important remark. Generally speaking, in the area of uniform magnetic field there are no eddy currents in a solid conductor because there is no possibility for them to be closed. The mutual interaction between $\vec{V}$ and $\vec{B}$ leads to a potential difference $\tilde{\phi}$ according to Poisson equation:

$$\bigtriangledown^2\tilde{\phi} = div(\vec{V} \times \vec{B}) \tag{11}$$

In reality the velocity field $\vec{V} = \vec{V}(x, y, z)$ and $\vec{B} = \vec{B}(x, y, z)$ and consequently ϕ and $\vec{j}$ have complex three-dimensional distributions. But if there are no boundary layers or fringing zones of magnetic field, $\tilde{\phi}$ is the same between any two virtual planes inside the bar and the currents can not flow. Therefore we implicitly suggest that the currents can close through an imaginary resistor (fig.7).

In order to determine the Lorentz force and the Joule heat we need to compute the distribution of the magnetic field inside the plate. To accomplish this task, we start with the observation that due to the motion of the plate a secondary magnetic field $\vec{b}$ is induced. This field is proportional to $Re_m B_0$ and perturbs the primary (applied) magnetic field. For our simple geometry it can be shown that $\vec{b}$ has only one nonzero component and depends only on z and on t. Hence we can write the velocity field and magnetic field as following [19]:

$$\vec{V} = V(t)\vec{e}_x \tag{12}$$

$$\vec{B} = \vec{e}_z + b(z, t)\vec{e}_x. \tag{13}$$

Taking these equations, inserting them into (6) and observing that outside the plate the secondary magnetic field is independent on z, it can be readily demonstrated that the distribution of the secondary magnetic field $b(z,t)$ in the moving plate is described by the one-dimensional diffusion equation

$$\frac{\partial b}{\partial t} = \frac{\partial^2 b}{\partial z^2} \tag{14}$$

with the initial condition $b(z,0) = 0$ and with the mixed boundary conditions [19]:

$$\left. b(z,t) \right|_{z=0} = 0 \tag{15}$$

$$\left. \frac{\partial b(z,t)}{\partial z} \right|_{z=1} = -V(t) \tag{16}$$

The first boundary condition involves the fact that the solution of the magnetic field is expected to be antisymmetric. The second boundary condition is a kind of matching condition and can be obtained by integrating (6) over an ϵ-neighborhood of the boundary. Here is the detailed derivation. Using the identity

$$\nabla \times (\vec{V} \times \vec{B}) = (\vec{B}\nabla)\vec{V} - (\vec{V}\nabla)\vec{B} + \vec{V}(\nabla\vec{B}) - \vec{B}(\nabla\vec{V}) \tag{17}$$

we obtain

$$\nabla \times (\vec{V} \times \vec{B}) = B_0 \frac{\partial \vec{V}}{\partial z} \tag{18}$$

Therefore one can verify that

$$\frac{\partial \vec{b}(z,t)}{\partial t} = B_0 \frac{\partial \vec{V}}{\partial z} + \lambda \frac{\partial^2 \vec{b}(z,t)}{\partial z^2} \tag{19}$$

The next step is to integrate (19) over an ϵ-neighborhood of the boundary:

$$\int_{D-\epsilon}^{D+\epsilon} \frac{\partial \vec{b}(z,t)}{\partial t} dz = \int_{D-\epsilon}^{D+\epsilon} \left(B_0 \frac{\partial \vec{V}}{\partial z} + \lambda \frac{\partial^2 \vec{b}(z,t)}{\partial z^2} \right) dz \tag{20}$$

Here two facts are important. First, the magnetic field and its time-derivative are assumed to be finite and therefore the integral tends to zero if ϵ is small enough. Second, the velocity field is non-zero only inside the domain, that is:

$$\vec{V}(z) = \begin{cases} \vec{V}(t), & \text{for } z \leq D \\ 0, & \text{for } z > D \end{cases} \tag{21}$$

These arguments simplify the integration and immediately bring us to the boundary condition:

$$\left. \frac{\partial b(z,t)}{\partial z} \right|_{z=D-\epsilon} = -V(t) \frac{B_0}{\lambda} \tag{22}$$

Notice that this problem is mathematically equivalent to the heat transfer problem in a plate which is cooled down from above with time-dependent cooling rate $-V(t)$ and having constant zero temperature on the other side. This analogy is neither new nor surprising, it is indeed well known in magnetohydrodynamics [8]. The nontrivial mathematical aspect of the present problem is in the fact that the determination of the Lorentz force and the Joule heat require the computation of non-standard quantities that are unknown in heat transfer problems. We thereby demonstrate that a wide variety of exact analytical solutions of one-dimensional heat transfer problems known from the literature (see [20] and references therein) can be easily converted into relations useful for Lorentz force velocimetry.

Once the magnetic field $b(z,t)$ has been determined, the dimensionless y-component of the electric current density is given by $j_y(z,t) = -\partial b/\partial z$. From these two quantities the x-component of the Lorentz force density can be derived as $f(z,t) = j(z,t)b(z,t)$ and the volumetric generation of Joule heat is $q(z,t) = j^2(z,t)$. By integrating these two quantities over the thickness of the plate, we obtain the dimensionless time-dependent total Lorentz force $\xi(t)$ and the total Joule heat $\psi(t)$ as

$$\xi(t) = b(1,t) \tag{23}$$

$$\psi(t) = \int_0^1 j^2(z,t)dz \tag{24}$$

Before proceeding to the discussion of the results, we shall write down the relations that are necessary to convert the dimensionless Lorentz force $\xi(t)$ and Joule heat $\psi(t)$ back into dimensional quantities that are necessary for practical purposes. The time-dependent Lorentz force per unit area (with unit N/m^2) is obtained from ξ as

$$F = -\sigma D V_0 B_0^2 \xi(\lambda t/D^2), \tag{25}$$

(where the time in ξ should be taken in seconds). The time-dependent Joule heat per unit area (with unit W/m^2) is obtained from ψ as

$$Q = \sigma^2 D V_0^2 B_0^2 \psi(\lambda t/D^2). \tag{26}$$

2.3 Case 1: Stepwise velocity signal

We start our discussion with the analytically solvable problem of a sudden jump of the plate velocity described by

$$V(t) = \begin{cases} 0, & \text{for } t \le 0 \\ 1, & \text{for } t > 0 \end{cases} \tag{27}$$

The solution of the corresponding heat transfer problem is known from the literature [21]. The magnetic field and eddy currents distribution are [19]:

$$b(z,t) = \left[-z + 2\sum_{n=0}^{\infty} \frac{(-1)^n}{\alpha_n^2} \sin(\alpha_n z)\, e^{-\alpha_n^2 t}\right] \tag{28}$$

$$j(z,t) = \left[1 - 2\sum_{n=0}^{\infty} \frac{(-1)^n}{\alpha_n} \cos(\alpha_n z)\, e^{-\alpha_n^2 t}\right], \tag{29}$$

$$\alpha_n = \frac{2n+1}{2}\pi \tag{30}$$

Fig.8a and 8b show b and j as a function of z for different instants of time. Although the solution itself is not new, its application to the problem of magnetic diffusion leads to new conclusions. The field is antisymmetric with respect to $z = 0$ whereas the eddy currents are symmetric. Both b and j are zero at $t = 0$. When the plate starts to move, the secondary magnetic field continuously increases during transient phase. Later, the distribution of b tends to a linear dependence on z that corresponds to the steady-state heat transfer from the heated top to the cooled bottom of the plate in the corresponding heat-transfer problem. After a time of approximately $t = 1.5$ the transient phase is completed and the magnetic field distribution as well as the eddy current distribution remain at a steady state. The eddy currents, which flow to oppose the magnetic flux change, reach a constant value after the transient phase and remain constant at steady state while the plate is moving with constant velocity.

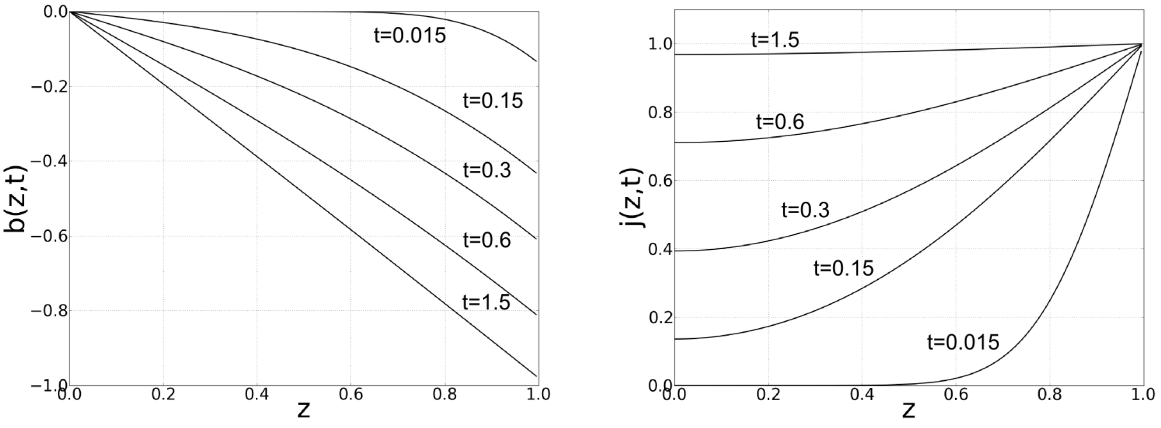

(a) (b)

Figure 8: Analytical solution of the induced magnetic field (a) and the eddy current density (b) for several instants of time as computed from (28) and (29).

Using (28) and (29) we compute the desired analytical expressions for the time dependent Lorentz force $\xi(t)$ and Joule heat $\psi(t)$ as

$$\xi(t) = \left[-1 + 2 \sum_{n=0}^{\infty} \frac{1}{\alpha_n^2} e^{-\alpha_n^2 t} \right] \tag{31}$$

$$\psi(t) = \left[1 - 4 \sum_{n=0}^{\infty} \frac{1}{\alpha_n^2} e^{-\alpha_n^2 t} \left(1 - \frac{1}{2} e^{-\alpha_n^2 t}\right) \right] \tag{32}$$

These quantities are shown in fig.9. Both are zero as long as the plate is at rest. After the jump of the conductor velocity the Lorentz force and the Joule heat increase and converge to their asymptotic values $\xi = \psi = 1$ as $t \to \infty$. It is interesting that the Joule heat grows slower than the Lorentz force which is a consequence of the fact that the Joule heat is a quadratic function of $\partial b/\partial z$ whereas the Lorentz force depends linearly on b. Notice that due to the diffusive character of the magnetic field the dissipated power Q is not equal to the instantaneous value of the product FV as would be intuitively expected on the basis of a quasi-static picture. From (31) and (32) one can infer that the different harmonics damp at different rate and it is sufficient to calculate only three terms in the

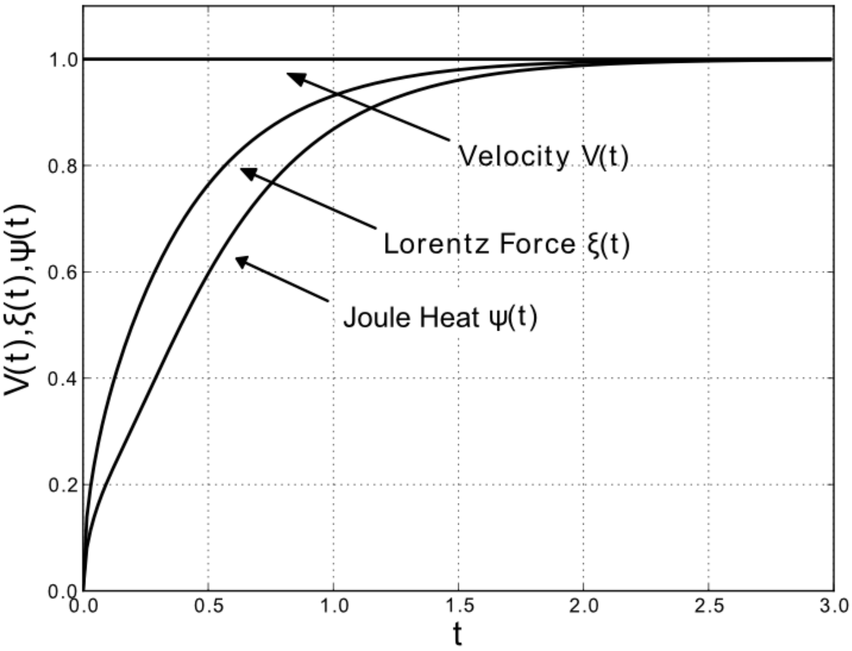

Figure 9: Analytical solution of the Lorentz force absolute value $|\xi(t)|$ and Joule heat $\psi(t)$ in case of stepwise velocity signal. Both functions approach unity as $t \to \infty$.

series. For dimensional time $t > \tau_{diff} = \mu\sigma D^2$ it is sufficient to calculate only the first term. Hence the fundamental time constant τ, which is the longest time constant of the series, is the controlling time constant in the diffusion process. The functions $\xi(t)$ and $\psi(t)$ allow us to determine the reaction times $T_{98\xi}$ and $T_{98\psi}$, which are defined via $\xi(T_{98\xi}) = 0.98$ and $\psi(T_{98\psi}) = 0.98$, i.e. as the time where the Lorentz force and the Joule heat have reached 98% of their asymptotic values. Our solution yields the dimensionless reaction times $T_{98\xi} = 1.48$ and $T_{98\psi} = 1.76$ which for practical purposes can be translated into dimensional reaction times by multiplying then by a factor $\mu\sigma D^2$. As described in [22] and [19], $T_{98\xi}$ can be directly used in the design of Lorentz force flowmeters for metallurgical applications where short reaction times are crucial.

2.4 Case 2: Exponential velocity signal

Practically stepwise velocity change can never be seen in a real experiment because it is impossible to change a conductor velocity with an infinite acceleration. Therefore, it is essential to investigate a problem where velocity is changed smoothly. Here we consider a second case, which is characterized by $V(t) = (1 - e^{-Re_{m(\tau)}t})$, where $Re_{m(\tau)} = \mu\sigma D^2/\tau$ is magnetic Reynolds number based on the time τ during which the velocity is changed. To obtain an analytical solution for that case, we refer to Duhamel's principle [23]. It says that if $P(t)$ is a time-varying boundary condition, then this value can be considered to be composed of an infinite number of infinitesimal step functions that switch on at different times. Thereby we can construct a system response to an input which varies continuously in time by adding together the responses to each of these step units. If

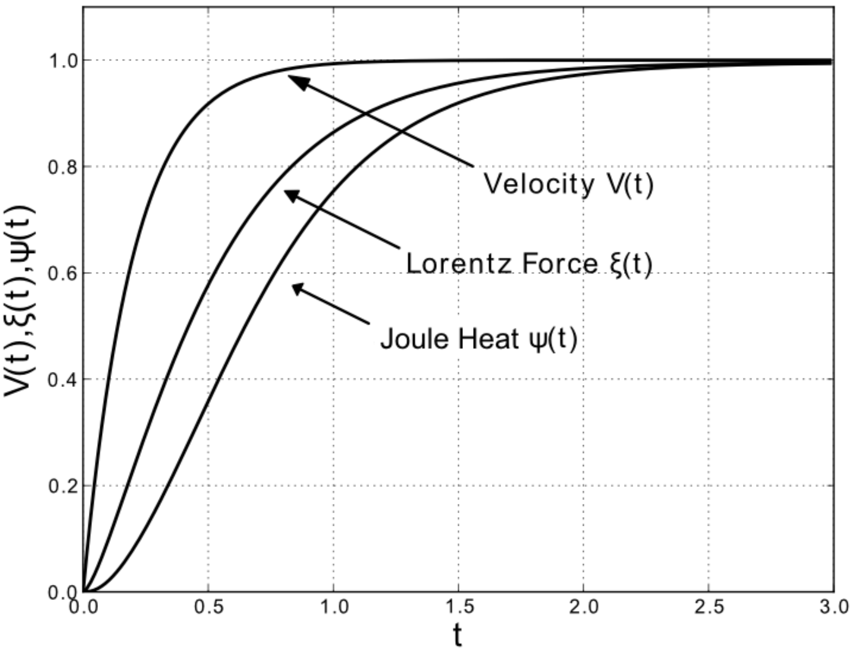

Figure 10: Analytical solution of Lorentz force $\xi(t)$ and Joule heat $\psi(t)$ in case of $V(t) = 1 - \exp(Re_{m(\tau)}t)$, where $Re_{m(\tau)} = 5$. Since the velocity increases more slowly than in the case with stepwise velocity signal, $T_{98\xi}$ is bigger than 1.48 at any $Re_{m(\tau)}$.

$b^{(0)}(z,t)$ is a response of a system to the unit step, a corresponding solution for non-stationary problem would be:

$$b(z,t) = \int_0^t P(\tau)\frac{\partial b^{(0)}(z,t-\tau)}{\partial t}d\tau \tag{33}$$

Since the function $b^{(0)}(z,t)$ has been found in Section 2.3, we are able to find an exact solution for any velocity signal, which can be analytically integrated. Applying Duhamel's principle we obtain:

$$\begin{aligned}
b(z,t) &= 2\sum_{n=0}^{\infty}(-1)^n \sin(\alpha_n z)\,\gamma(t, Re_{m(\tau)}, \alpha_n) && (34)\\
j(z,t) &= 2\sum_{n=0}^{\infty}(-1)^{n+1}\alpha_n \cos(\alpha_n z)\,\gamma(t, Re_{m(\tau)}, \alpha_n) && (35)\\
\xi(t) &= 2\sum_{n=0}^{\infty}\gamma(t, Re_{m(\tau)}, \alpha_n) && (36)\\
\gamma(t, Re_{m(\tau)}, \alpha_n) &= \exp\left[\frac{1-e^{-\alpha_n^2 t}}{\alpha_n^2} + \frac{e^{-Re_{m(\tau)}t} - e^{-\alpha_n^2 t}}{Re_{m(\tau)} - \alpha_n^2}\right] && (37)
\end{aligned}$$

The response of the Lorentz force and the Joule heat for finite acceleration is shown in fig.10. A general shape of velocity resembles one in the first case, but here a function growth is slower with $T_{98\xi} = 1.74$. See Table 2 for the detailed response characteristics.

$Re_{m(\tau)}$	T_{98v}	$T_{98\xi}$	$T_{98\psi}$	$T_{98v}/T_{98\xi}$
1	3.91	4.34	5.03	0.9
2	1.96	2.55	2.92	0.77
3	1.30	2.05	2.35	0.63
4	0.98	1.85	2.13	0.53
5	0.78	1.74	2.02	0.45
∞	0	1.48	1.76	0

Table 2: Reaction time for several $Re_{m(\tau)}$ of a motion setup using finite accelerations expressed with an exponential function.

2.5 Case 3: Periodical velocity signal

The case of sinusoidal motion is of great importance, because it reveals a process of the magnetic field penetration into a material. In our third case we assume that the time dependent velocity satisfies $V(t) = \cos(Re_{m(\omega)}t)$, where $Re_{m(\omega)} = \mu\sigma D^2\omega$ is magnetic Reynolds number based on the plate oscillation frequency ω. Using Duhamel's principle, the result for the induced field, eddy currents density, the Lorentz force and Joule heat is:

$$b(z,t) = 2\sum_{n=0}^{\infty}(-1)^{n+1}\sin(\alpha_n z)\,\varepsilon(t, Re_{m(\omega)}, \alpha_n) \tag{38}$$

$$j(z,t) = \pi\sum_{n=0}^{\infty}(-1)^{n}(2n+1)\cos(\alpha_n z)\,\varepsilon(t, Re_{m(\omega)}, \alpha_n) \tag{39}$$

$$\xi(t) = -2\sum_{n=0}^{\infty}\varepsilon(t, Re_{m(\omega)}, \alpha_n) \tag{40}$$

$$\psi(t) = 2\sum_{n=0}^{\infty}\alpha_n^2\varepsilon^2(t, Re_{m(\omega)}, \alpha_n), \tag{41}$$

$$\varepsilon(t, Re_{m(\omega)}, \alpha_n) = \frac{Re_{m(\omega)}\sin(Re_{m(\omega)}t) + \alpha_n^2\cos(Re_{m(\omega)}t)}{Re_{m(\omega)}^2 + \alpha_n^4} \tag{42}$$

Here we neglected an influence of the initial conditions (additional term $(-\alpha_n^2 e^{-\alpha_n^2 t})/(Re_{m(\omega)}^2 + \alpha_n^4)$ in the function ε), because an asymptotic solution is of our primary interest. Fig.11 shows Lorentz force and Joule heat as a function of time. There are some remarkable facts. The first one is a doubled frequency of the Joule heat. This is due to the quadratic dependence on eddy current density and subsequently on the square of the velocity signal. Second, there is a phase shift $\Delta\phi_\xi$ between the velocity of the plate and the Lorentz force $\xi(t)$ as well as the phase shift $\Delta\phi_\psi$ between velocity signal and Joule heat $\psi(t)$. Moreover the amplitudes of the Lorentz force A_ξ and the Joule heat A_ψ must depend on the frequency of the moving plate. Therefore (40) and (41) can be expressed in a more descriptive way:

$$\xi(t) = A_\xi(Re_{m(\omega)})\cdot\cos(Re_{m(\omega)}t + \Delta\phi_\xi) \tag{43}$$

$$\psi(t) = A_\psi(Re_{m(\omega)})\cdot\cos(Re_{m(\omega)}t + \Delta\phi_\psi) \tag{44}$$

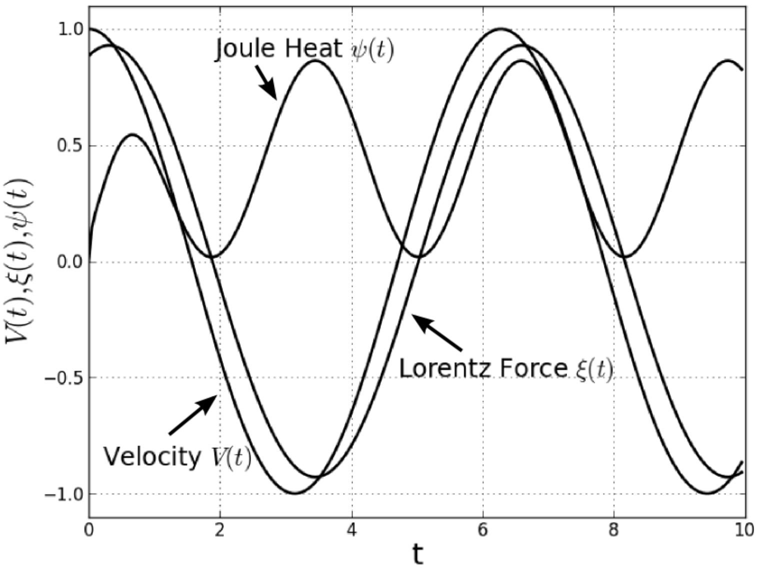

Figure 11: Analytical solution of Lorentz force $\xi(t)$ and Joule heat $\psi(t)$ in case of $V(t) = \cos(Re_{m(\omega)}t)$, where $Re_{m(\omega)} = 1$. There is a certain phase shift between $V(t)$ and $\xi(t)$, which tends to $\pi/2$ when $Re_{m(\omega)} \to \infty$.

With (40), one can analytically obtain an expression for the phase shift $\Delta\phi_\xi$.

$$\Delta\phi_\xi(t \to \infty) = \arctan \frac{\sum_{n=0}^{\infty} \frac{Re_{m(\omega)}}{Re^2_{m(\omega)} + \alpha_n^4}}{\sum_{n=0}^{\infty} \frac{\alpha_n}{Re^2_{m(\omega)} + \alpha_n^4}} \tag{45}$$

Then it can be shown that

$$\lim_{Re_{m(\omega)} \to 0} \Delta\phi_\xi = 0 \qquad \lim_{Re_{m(\omega)} \to \infty} \Delta\phi_\xi = \frac{\pi}{2} \tag{46}$$

It stands for the fact that the phase shift vanishes if $Re_{m(\omega)} \to 0$ and the force exactly follows the velocity signal. On the other hand, if $Re_{m(\omega)} \to \infty$ the phase shift $\Delta\phi \to \pi/2$ while the Lorentz force amplitude tends to zero because of the skin-effect [1]. Therefore the amplitude A_ξ decays approximately as $1/Re_{m(\omega)}$ and reads:

$$A_\xi = -2 \sum_{n=0}^{\infty} \frac{1}{\sqrt{1+\Psi^2}} \frac{\Psi Re_{m(\omega)} + \alpha_n^2}{Re_{m(\omega)} + \alpha_n^4}, \tag{47}$$

where

$$\Psi = \frac{\sum_{n=0}^{\infty} \frac{Re_{m(\omega)}}{Re^2_{m(\omega)} + \alpha_n^4}}{\sum_{n=0}^{\infty} \frac{\alpha_n^2}{Re^2_{m(\omega)} + \alpha_n^4}} \tag{48}$$

The same tendencies can be observed with the function $\psi(t)$. This is illustrated on fig.12. The absence of the phase shift between the velocity signal and the force response in case of small $Re_{m(\omega)}$ is clear. Since the oscillation frequency is small, the magnetic field has enough time to diffuse before being advected that allows the force to react quickly to a velocity change.

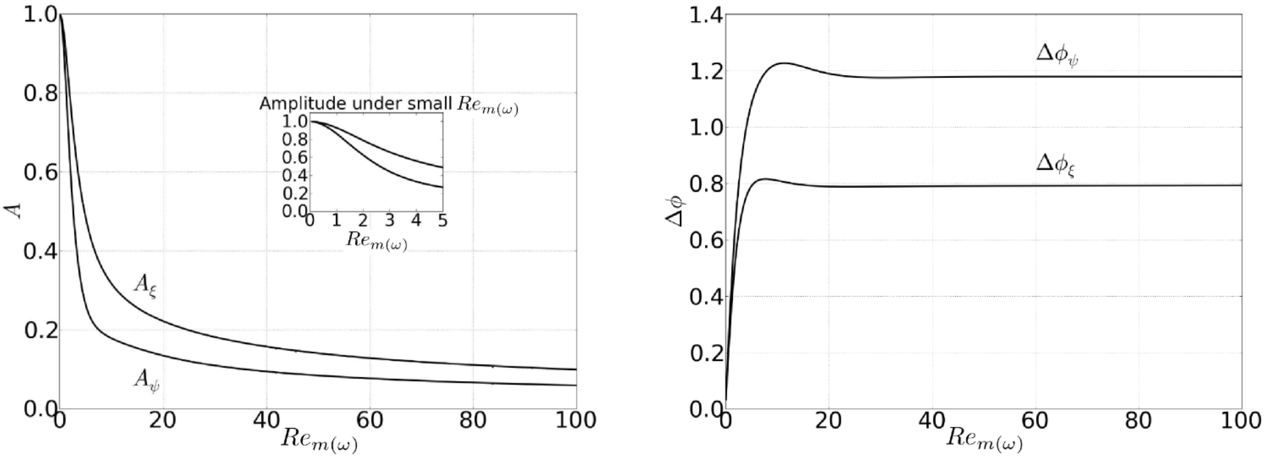

a) b)

Figure 12: Amplitudes A_ξ and A_ψ (a) and phase shifts $\Delta\phi_\xi$ and $\Delta\phi_\psi$ (b) as a function of $Re_{m(\omega)}$. The behavior of these curves agrees well with an assumption that under high $Re_{m(\omega)}$ magnetic filed lines become frozen into a conductor and there is no relative movement anymore that leads to the absence of the Lorentz force.

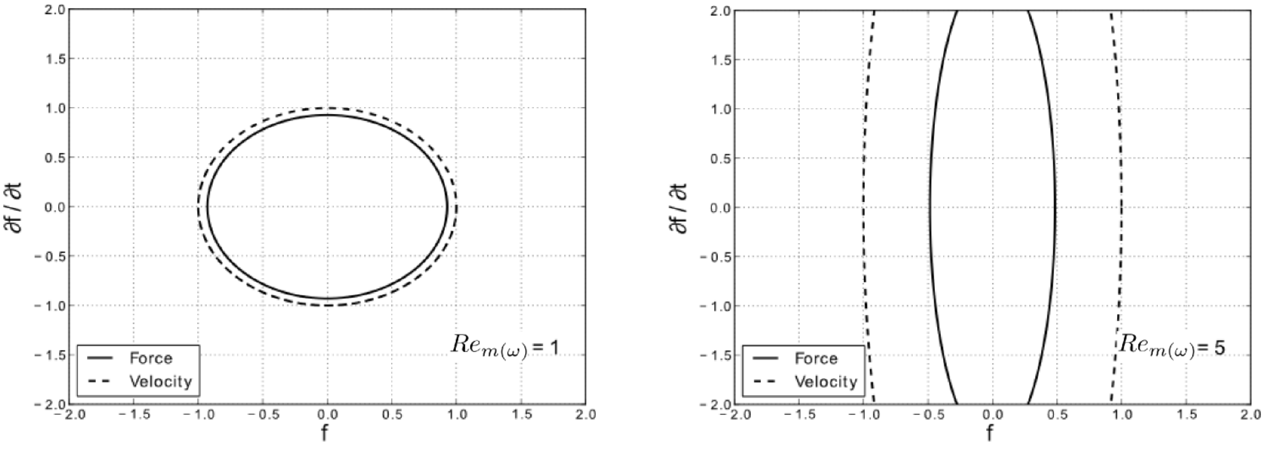

a) b)

Figure 13: (a) Elliptic phase trajectories of $V(t)$ and $\xi(t)$ when $Re_{m(\omega)} = 1$. The ellipses are very close to each other that denotes the small phase shift between the functions; (b) when $Re_{m(\omega)} \geq 5$ both ellipses deform significantly. An amplitude of the major axis of V-ellipse remains constant, whereas it diminishes in case of ξ-ellipse owing to the skin-effect.

The case with infinitely high $Re_{m(\omega)}$ has to be explained more detailed. To understand why the time shift dependency approaches a constant value, it is helpful to consider a phase space. Phase trajectories of velocity and force functions are ellipses, whose geometrical characteristics strongly depend on $Re_{m(\omega)}$. The $V(t)$ and $\xi(t)$ phase curves at $Re_{m(\omega)} = 1$ are shown in fig.13a. Due to the fact that ellipsis are close to each other, there is no phase shift between two functions as it was mentioned above. But the shape of the ellipses is significantly deformed at $Re_{m(\omega)} \geq 3$ (fig.13b). The major axis of the ξ-ellipse becomes smaller because of the skin-effect, whereas the amplitude of a minor axis tends to infinity as well as the minor axis of V-ellipse. At the same time, the major axis of V-ellipse remains constant. This tendency results in the fact, that wherever points on the ellipses have been before deformation, afterwards the phase angle will be $\pi/2$. Also this fact has to do with the following physical interpretation: even under high oscillation frequency there are thin skin layers at both sides of the plate where an equilibrium between advection and diffusion is achieved. If $Re_{m(\omega)} \to \infty$ the skin layer thickness tends to zero while increasing the distance between the layers, that leads to their mutual insensitivity. This fact plays a key role in a phase shift phenomenon.

2.6 Numerical solution

In order to investigate the time-dependent Lorentz force and Joule heat for arbitrary velocity signals $V(t)$ we use a simple second-order finite difference code. This code is state of the art and needs no further verification (see [20], [24]).

$$\frac{b_i^{k+1} - b_i^k}{\triangle t} = \lambda \frac{b_{i+1}^k - 2b_i^k + b_{i-1}^k}{\triangle z^2} \tag{49}$$

$$b_i^{k+1} = (1 - 2\Gamma) b_i^k + b_{i-1}^k + \Gamma b_{i+1}^k \tag{50}$$

$$\Gamma = \lambda \frac{\triangle t}{\triangle z^2} \tag{51}$$

The explicit method has been selected because it is less numerically intensive in comparison with other finite difference methods such as the implicit method or the Crank-Nicolson method. In addition, it is numerically stable and convergent whenever $\Gamma \leq 1/2$ [20]. The excitation in the form of an error function represents a realistic case of accelerated motion, for instance, a linear drive with motion controller. The error-function is in the form

$$V(t) = erf\left[Re_{m(\tau)}^{err} t\right] \tag{52}$$

$Re_{m(\tau)}^{err}$	T_{98v}	$T_{98\xi}$	$T_{98\psi}$	$T_{98v}/T_{98\xi}$
1	1.65	2.36	2.64	0.70
2	0.82	1.83	2.10	0.45
3	0.55	1.70	1.98	0.32
4	0.41	1.64	1.92	0.25
5	0.33	1.61	1.88	0.20
∞	0	1.48	1.76	0

Table 3: Reaction time for several $Re_{m(\tau)}^{err}$ of the error function in (52).

If $Re^{err}_{m(\tau)} = \infty$ the error function shows identical characteristic as the step function. For small values of $Re^{err}_{m(\tau)}$ the error-function has a smaller slope and the Lorentz force and the Joule are almost able to follow the input signal without delay (Table 3).

	D=20 mm	D=40 mm	D=60 mm	D=80 mm	D=100 mm
Cu	44 / 52	176 / 209	395 / 470	702 / 835	1097 / 1305
Al	27 / 32	107 / 127	241 / 287	429 / 510	670 / 796
Steel	10 / 12	42 / 50	94 / 111	167 / 198	260 / 310

Table 4: Reaction time T_{98} in ms calculated from fig.(14) for Cu ($\sigma = 59\ MS/m$), Al ($\sigma = 36\ MS/m$) and steel ($\sigma = 14\ MS/m$) for different cylinder diameters. A time step was 1 ms and initial magnetic field $B_0 = 0.3\ T$. A value before slash corresponds to the Lorentz force, the one after - to the Joule heat.

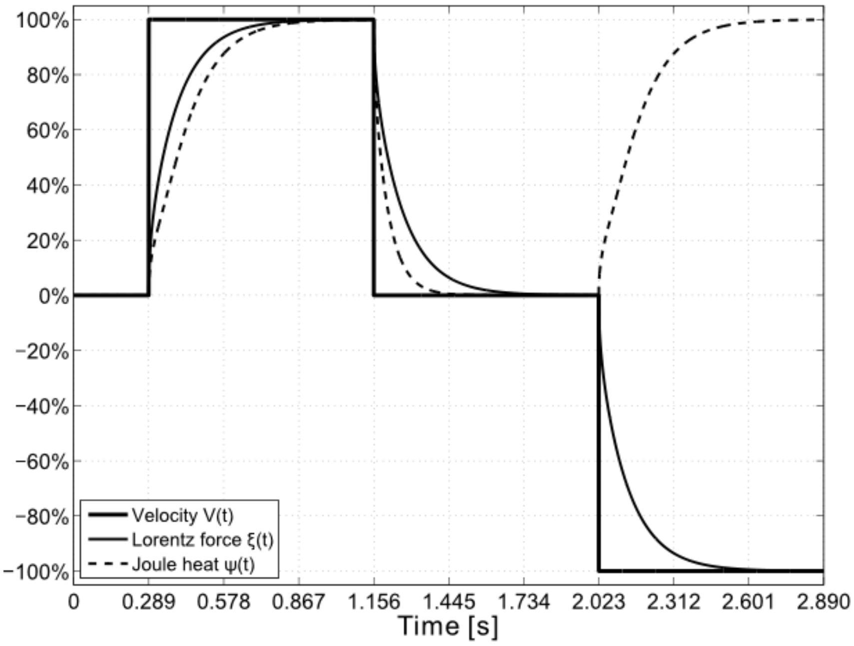

Figure 14: Time response of Lorentz force and Joule heat for an arbitrary velocity signal $V(t)$. The calculation are performed for an aluminum sheet with an electrical conductivity of 36 MS/m and a total thickness of 80 mm. The maximum velocity is 1 m/s and the primary magnetic field B_0 has a magnitude of 0.3 T [19].

Fig.(14) shows a simple example of a real production process including positive and negative changes in the velocity signal $V(t)$. It can be seen that the Lorentz force can be also positive or negative depending on the moving direction of the plate. In contrast, the Joule heat is always positive and does not depend on the moving direction of the plate. For the considered case of a 0.08 m thick aluminum plate with an electrical conductivity of $\sigma = 36 \cdot 10^6\ S/m$ one can obtain the dimensional reaction time of the Lorentz force and

Joule heat. Table 4 shows real physical values of T_{98} for the Joule heat and the Lorentz force. Also one remarkable fact must be mentioned here. As one can see on fig.14, T_{98} for the Lorentz force is identical for both velocity changes - from 0% to 100% and back from 100% to 0%. But it is not the case for the Joule heat, whose T_{98} is smaller when velocity drops down than when it rises up. In other words, the Joule heat reaches its maximum more slowly than it comes back to zero. Unfortunately, we can explain only a mathematical background of this phenomenon, leaving a physical interpretation unclear. Analytically one can see that the boundary condition for the case of rising velocity is not the same as the condition for the inverse transition. Recalling the analogy with thermal diffusion, the first case implies heating a plate from the one side and cooling it down from another one, whereas in the second case we start with already stationary temperature distribution and let the system evolve in time, while keeping the zero heat flux at the boundaries. This difference in boundary conditions explains inequality of values T_{98} for Joule heat. On the other hand, one can verify that temperature at the boundaries obeys the same equation in both cases. That is, whatever the direction of velocity change is, the value at the boundaries will evolve equally. Since the Lorentz force $\xi(t)$ is basically a value of magnetic field at the boundary, it has the same T_{98} for both transitions.

2.7 Conclusions

When a conducting flow enters a region with a transverse magnetic field, eddy currents are generated inside the conductor. On the one hand, these currents generate the induced magnetic field which changes the initial distribution of the imposed field. On the other hand, eddy currents give rise to the Lorentz force which brakes the flow. The mutual interaction between the fluid flow and the magnetic field is described by (5) and (6) which is a coupled system of two non-linear equations. To solve them analytically we considered the motion of a solid bar with a given time-dependent velocity through the homogeneous magnetic field. These simplifications allow us to boil down (6) to one-dimensional diffusion equation with velocity-dependent boundary conditions. The analytical solution has been obtained for three motion setups: stepwise, exponential and periodical velocity signals. It turns out that both Lorentz force and Joule heat strongly depend on time during transient phase, which causes a remarkable delay compared to the velocity of the plate. In case of stepwise velocity signal the dimensionless reaction time of the Lorentz force $T_{98\xi} = 1.48$ is smaller than the reaction time of the Joule heat $T_{98\psi} = 1.76$. As it was expected, different velocity signals cause different shapes of the time response function. The case of an oscillating motion of the plate is remarkable because the Lorentz force shows a drop in the amplitude and the phase shift approaches a constant value at $Re_{m(\omega)} \to \infty$. Both the force and the phase shift depend on the plate oscillation frequency. This fact is strongly related to skin layers which appear due to the oscillating motion of the plate. Also the Joule heat doubles the oscillation frequency, because of the quadratic dependence on the eddy current density.

3 Experiments with aluminium and copper solid conductors

Although the theoretical approach in Section 2 is a good attempt to describe the generated Lorentz force, the used model does not reveal all the physics even in case of no turbulence. The reason is that we considered quasi-two dimensional case whereas eddy current loops form very complicated three-dimensional paths inside a conductor. Moreover, even if a uniform magnetic field is applied, it can not extend infinitely. As a consequence, there are always areas where the magnetic field decays. Eddy current distribution there is different to the distribution in the homogeneous area that complicates a theoretical analysis [10]. Usually finite Re_m effects are attributed to high-speed flows. However, effects of the perturbation of the imposed magnetic field by the induced one can be observed even at typical flow velocities. That leads to measurement errors because the Lorentz force responses differently to the same velocity change in the case when the imposed field B_0 is perturbed. Errors in velocity measurements in metallurgical applications might lead to an excessive or insufficient amount of an alloy ingredient and consequently to undesirable properties of metal slabs. It emphasizes the importance of an experimental research.

3.1 Problem definition

The problem is sketched on fig.15. A solid electrically conducting rod which moves through a transverse magnetic field B_0 with a time-dependent velocity $V(t)$ is considered. Initially the rod is placed at rest into a nonhomogeneous magnetic field created by two permanent magnets. At $t = t_0$ rod starts to move that according to the Ohm's law (1) gives rise to eddy currents j which are generated in fringing areas of magnetic field. The currents close in areas before and behind magnets where the magnetic field is absent (fig.16a). The interaction between j and the sum of B_0 and b results in the Lorentz force $\vec{F} = \int \vec{j} \times (\vec{B}_0 + \vec{b}) dV$ which, on the one hand, acts on the magnets and, on the other hand, brakes the rod. Magnetic field b carried by eddy currents can be strong enough to deform the initial distribution of B_0 so that magnetic field lines are bent. We underline that although the evolution concerns the induced field only, the total field $\vec{B}_0 + \vec{b}$ contributes to the Lorentz force. The evolution of the total magnetic field is divided into two phases. The first phase is transient. It starts at $t = t_0 + dt$ and characterized by the nondimensional magnetic Reynolds number Re_m^τ based on the advection time τ [25]:

$$Re_m^\tau = \frac{\partial \vec{B}/\partial t}{\lambda \Delta \vec{B}} \sim \frac{D^2}{\lambda \tau}, \tag{53}$$

where $\lambda = 1/\mu\sigma$ is a magnetic diffusivity, $\mu = 4\pi \cdot 10^{-7} H \cdot m^{-1}$ is the magnetic permeability, σ is a an electrical conductivity and D stands for a characteristic length. Within this phase magnetic field lines are being dragged with conductor until the equilibrium between magnetic field advection and diffusion is achieved. Once it happens, the second phase starts. This phase is stationary ($t \gg t_0$) and is described by the magnetic Reynolds number Re_m^V based on the conductor velocity V [25]:

$$Re_m^V = \frac{\nabla \times (\vec{V} \times \vec{B})}{\lambda \Delta \vec{B}} \sim \mu\sigma V D \tag{54}$$

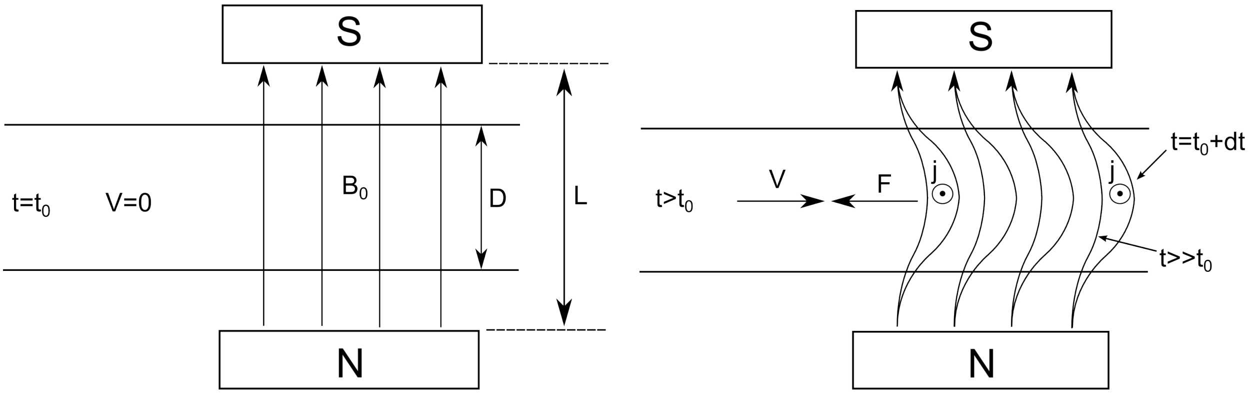

(a) Before onset of the motion (b) After onset of the motion

Figure 15: Sketch of the problem: (a) the imposed magnetic field diffused initially into rod before it starts to move; (b) after onset of the motion eddy currents j ensue that leads to an appearance of Lorentz force F and induced magnetic field b. The initial distribution of the imposed magnetic field starts to change at $t = t_0$ and its evolution in time is divided into two phases: transient phase($t = t_0 + dt$) and stationary phase ($t \gg t_0$).

These two magnetic Reynolds numbers must not necessarily have the same order of magnitude. A ratio Re_m^V/Re_m^τ is determined by two key values: a time of velocity change and a final value of that velocity. We give a short note about eddy currents which circulate in the conductor. Since a size of magnets is finite, there are areas where the imposed magnetic field is homogeneous and nonhomogeneous. A conductor motion through the area of nonhomogeneous magnetic field leads to the eddy currents j_1 and j_2 [6]. The induced magnetic field created by these currents opposes or enhances the external field B_0 (fig.16a) resulting in a formation of B_0-lines bending (fig.15b). These end-currents contribute to the Lorentz force, whose response to a time-dependent velocity is also nonstationary (fig.16b). In a fluid flow, there are additional currents in the uniform area of B_0 whose circulation plane is normal to a velocity vector [10]. Since we consider a solid rod, only a potential difference is generated in the zone of uniform magnetic field because there are no boundary layers to let currents be closed through them. The charges are distributed through an extremely thin layer on a conductor surface. They constantly leak from the area of uniform magnetic field to a fringing area but this leakage is always compensated by the induced electric field $\vec{V} \times \vec{B}$.

The aim is to study Lorentz force response $F(t)$ to the velocity input $V(t)$ at different magnetic Reynolds numbers Re_m^τ that have finite values due to a rapid change of the conductor velocity (fig.16b).

3.2 Experimental setup

The experimental setup (fig.17, fig.18a) consists of two 10 mm aluminium plates with a piezoelectric force sensor PCB 208C01 mounted inbetween (fig.18b). At the top plate, there is a magnetic Halbach array [26] which creates a constant transverse magnetic field in the range from 0 to 1 T depending on distance between magnets. A hole 20 cm in diameter has been made in the center of the plates so that a thick massive conducting aluminium or copper rod 4 cm to 8 cm in diameter (Table 5) can easily go through. An array of 7

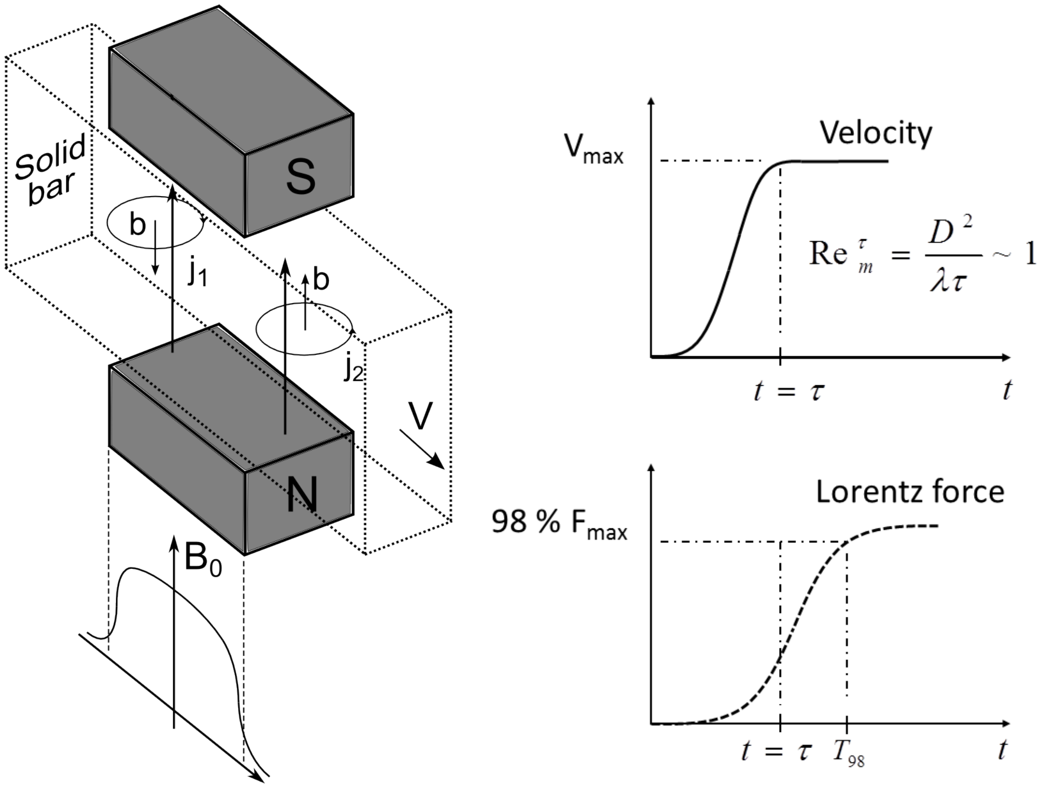

(a) (b)

Figure 16: (a) Circulation of eddy currents j_1 and j_2 in the fringing areas, induced secondary magnetic fields b and absence of current generation in a uniform part of B_0; (b) time delay between conductor velocity signal and corresponding Lorentz force response (schematic drawing).

Hall sensors CYTHS124 is installed in the area between the magnets and the rod for the induced magnetic field measurements. Due to a specific arrangement of magnetization vectors a field distribution has 4 zones with sharp gradients that leads to a higher Lorenz force amplitude. The sensors were mounted equidistantly, two of them are outside the initial field and five are within the area where B_0 was imposed. To connect sensors to the electronic board low-temperature welding was applied. A three-phase synchronous motor is used to rotate the spindel which is connected through the cantilever to the rod. This mechanical system converts spindel rotation velocity to the rod linear velocity. In order to test different rods, 30-40 cm center orifices with inner threads are made. A shaft with outer thread goes through the cantilever and is screwed in the rods. A pair of counter-rotating nuts is used to fix the rod and prevent it from spinning. After the rod is mounted, it is vertically aligned that a distance between magnets and the rod surface does not change during motion. For the detailed description of the setup and drive mechanism see [22]. The rotation velocity of the spindel is controlled by a computer with 1 kHz frequency so that the rod can be accelerated up to 130 mm/s within the advection time $\tau \approx 80\ ms$. A condition $Re_m^{\tau} \sim 1$ was always met because τ has an order of diffusion time $t_{diff} = \mu\sigma D^2$. Signals are acquired by 8-channels data logger Graphtec GL 900 with 50 kHz sampling frequency.

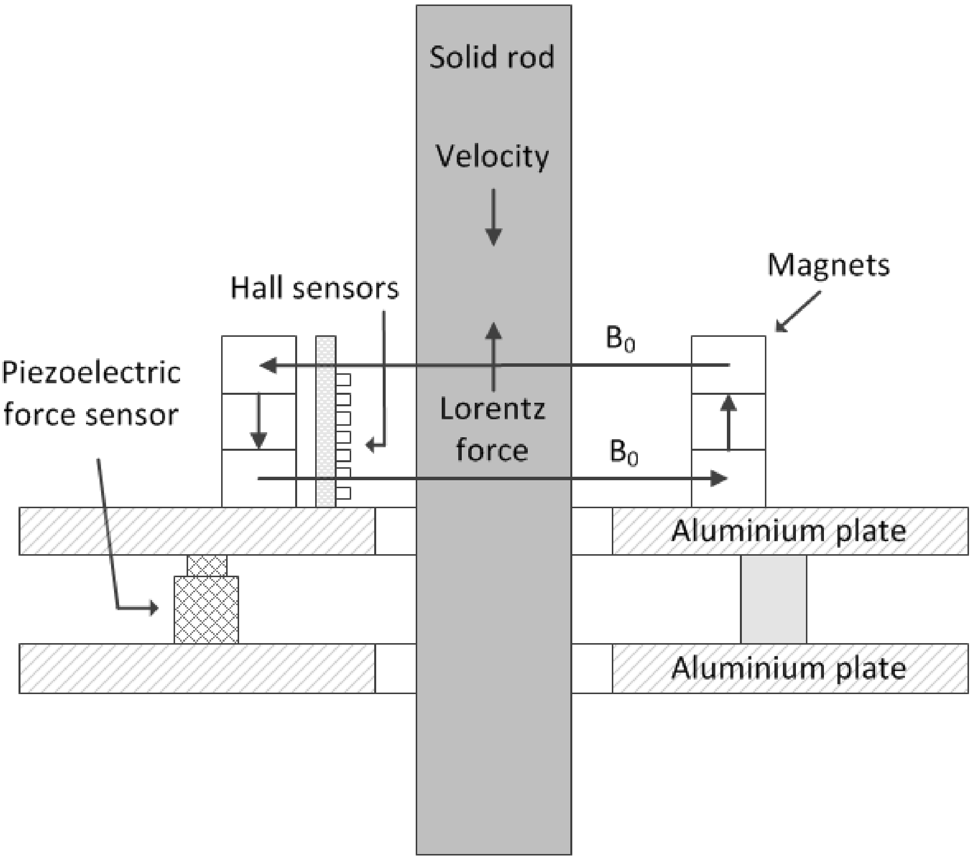

Figure 17: Sketch of the setup: a solid electrically conducting rod moves through a transverse magnetic field created by a linear Halbach array. Sharp gradients of the imposed field lead to the high Lorentz force. To perform dynamic force measurements piezoelectric force sensor PCB 208C01 is used. The variation of the imposed magnetic field is measured by an array with Hall sensors CYTHS124.

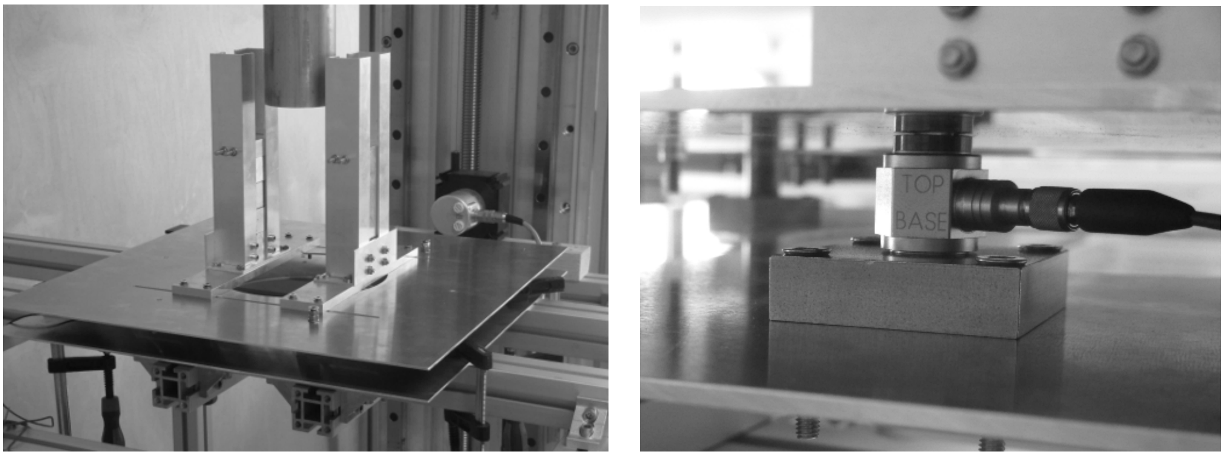

(a) (b)

Figure 18: Photo of the setup: (a) the initial assembly. After vibration tests, thin aluminium plates were replaced by thick ones with the thickness 10 mm. Additionally rubber damping sheets were installed between the bottom plate and the frame to get rid of low frequency vibrations; (b) the piezoelectric force sensor measures the Lorentz force acting on the magnet system and on the top plate.

	Aluminium alloy, $\sigma = 20\ MS/m$					Copper, $\sigma = 58\ MS/m$		
D, mm	40.17	50.08	60.21	70.62	79.94	40.1	50.05	60.1
D*	0.61	0.66	0.70	0.73	0.75	0.61	0.66	0.70
Re_m^τ	0.59	0.94	1.29	1.82	2.42	1.78	2.72	3.97

Table 5: Diameter D of the rods, aspect ratio $D^* = D/L$ (fig.15a) used in experiment and calculated magnetic Reynolds number Re_m^τ.

3.2.1 Piezoelectric force sensor PCB 208C01

The piezoelectric sensor is the key measurement tool in this experiment. Thus it is necessary to discuss its performance in detail. Indeed they are many force sensors available on the market. But the sensors with piezoelectric transducers stand out in applications where one has to conduct dynamic measurements. The deflection of the sensing element is always very small so that the sensor has a large natural frequency and shows a very fast response to the applied force. However, a serious drawback is that piezoelectric sensors are not suitable for static measurements. If the applied load is constant the output signal immediately starts to decay because of a charge leakage [27]. A decay rate is characterized by a discharge time constant t_D. The higher the t_D, the longer it takes for an output signal to go to zero. Very often a rule of thumb is applied: a signal goes down from 100% to 0% within 5 t_D. According to the manuals $t_D \geq 50s$ (Appendix A). However the actual measurements show that it is not true (fig.19).

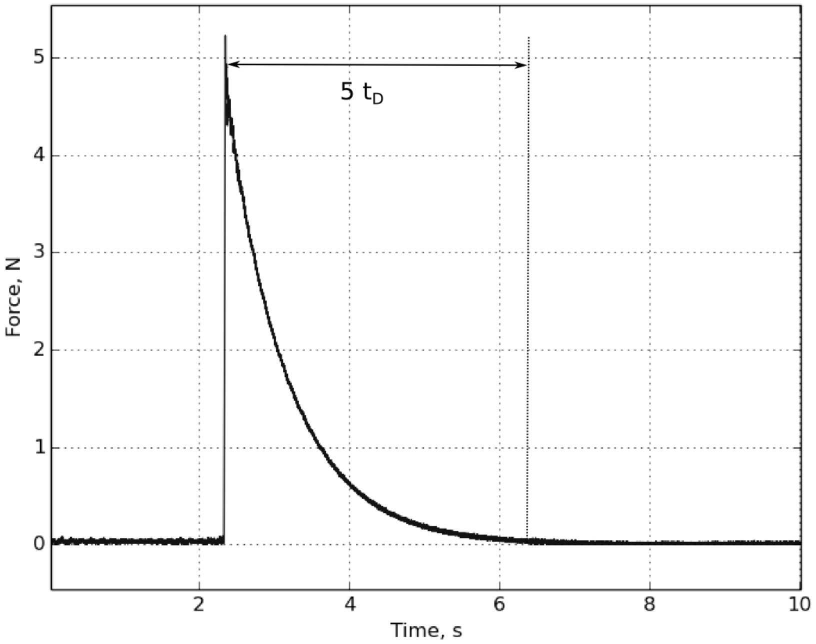

Figure 19: Calculation of time discharge constant t_D: due the charge leakage the output signal goes to zero within $5t_D$.

The load was created by applying a mass of approximately 500 g. It was observed that the signal decays completely within 4 s that means $t_D = 0.8\ s$. Having calculated this parameter, one can estimate the error due the charge leakage. The charge amplification is governed by (55) [27].

$$\dot{U}_{out} + \frac{U_{out}}{t_D} = S_v \dot{U}_{in}, \tag{55}$$

where S_v is the voltage sensitivity, U_{in} and U_{out} stand for input and output signals correspondingly. It has a particular solution for any transient signal:

$$U_{out}(t) = S_v e^{-t/t_D} \int_0^t e^{\zeta/t_D} \dot{U}_{in}(\zeta) d\zeta, \tag{56}$$

where ζ is the variable of time integration. Using (56) we obtain that the relative error caused by the charge leakage $\eta \sim 5\%$. To eliminate this error the measured force is multiplied by the factor of 1.05.

3.2.1.1 Damping The actual measurements are dynamic because conducting rods change their velocity rapidly and the Lorentz force has a corresponding dynamic response. Acceleration of the rods leads to undesirable vibrations of the whole aluminium construction that reduces the quality of an acquired force signal. The solution of this problem is to damp the vibrations. G+H MAFUND rubber sheets were used for that purpose (fig.20a). First of all, the sheets were placed between the parts of the setup to which the rods are connected. Secondly, the whole setup was isolated by the sheets from vibrations coming through the ground. As a result, low-frequency vibrations were diminished (fig.20b).

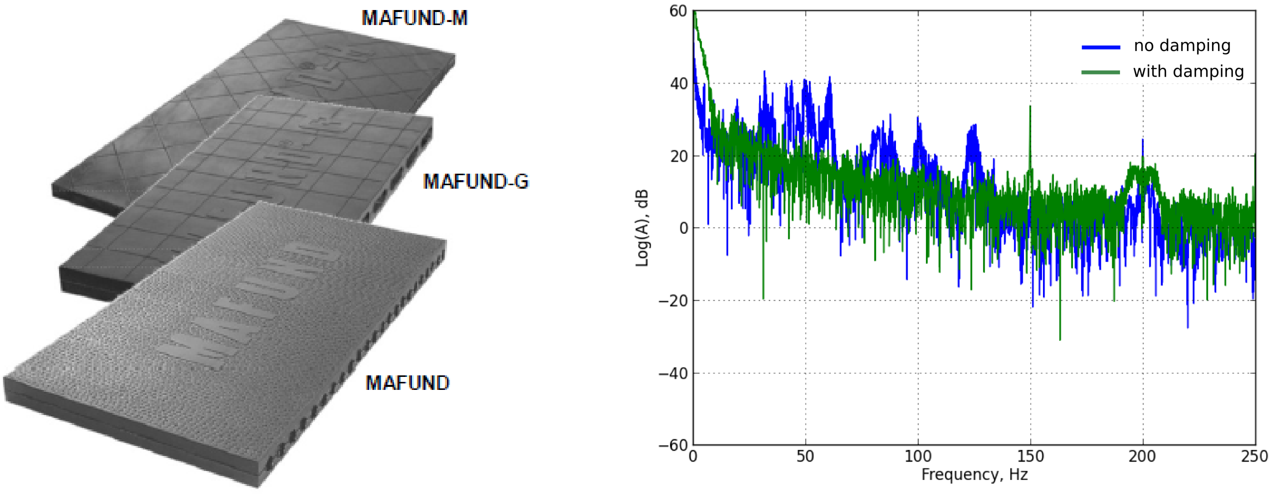

(a) (b)

Figure 20: (a) MAFUND rubber sheets for vibration isolation and structure-borne noise reduction. The sheets were inserted between aluminium frames of the stand and between the stand and the ground. The photo courtesy of G+H Isolierung Group; (b) spectrum of a typical force signal in two cases: with and without damping rubber sheets. One can clearly see that the frequencies below 200 Hz are noticeably damped.

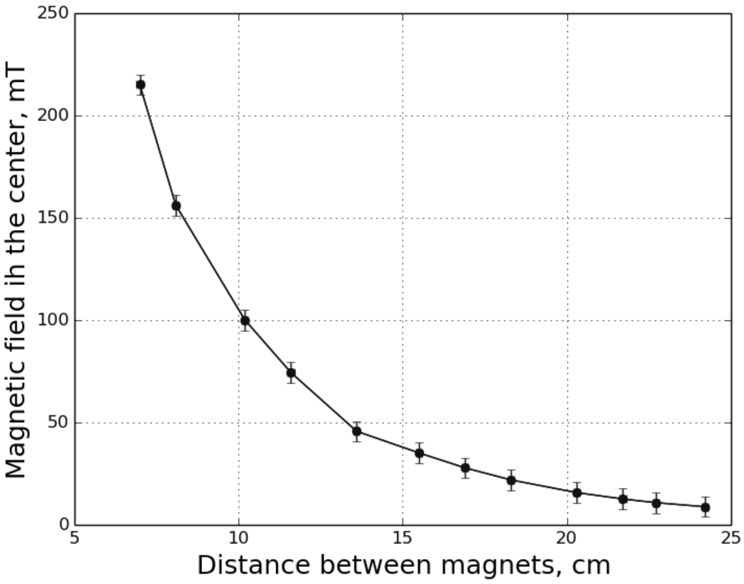

Figure 21: Measurements of the imposed magnetic field: the value of B_0 in the center of the linear Halbach assembly.

3.3 Results

3.3.1 Imposed magnetic field measurements

The field created by the linear Halbach assembly was measured by Lakeshore 475 DSP Gaussmeter with the precision $\pm 5mT$. The value of the field in the center depends on the distance between magnets and this dependency is shown in fig.21.

3.3.2 Lorentz force measurements

The velocity signal $V(t)$ is received directly from the motor which drives the rod. We performed measurements at 5 different velocity signals (fig.22a) having the acceleration time always about 80 ms. The Lorentz force $F(t)$ as a response (fig.22b) to these velocity inputs is measured at different magnetic Reynolds numbers Re_m^τ for copper and aluminium rods and force maxima versus corresponding velocity peaks are plotted on fig.23a. As expected, there is a linear dependence between F_{max} and V_{max} because $Re_m^\tau \ll 1$ (e.g. for Cu rod with $\sigma = 59\ MS/m$ and $D = 80\ mm$ we have $Re_m^V = 0.06$) and therefore

$$F_{max} \sim \sigma V_{max} B_0^2 D^2 l_1, \tag{57}$$

where l_1 - is a magnet length.

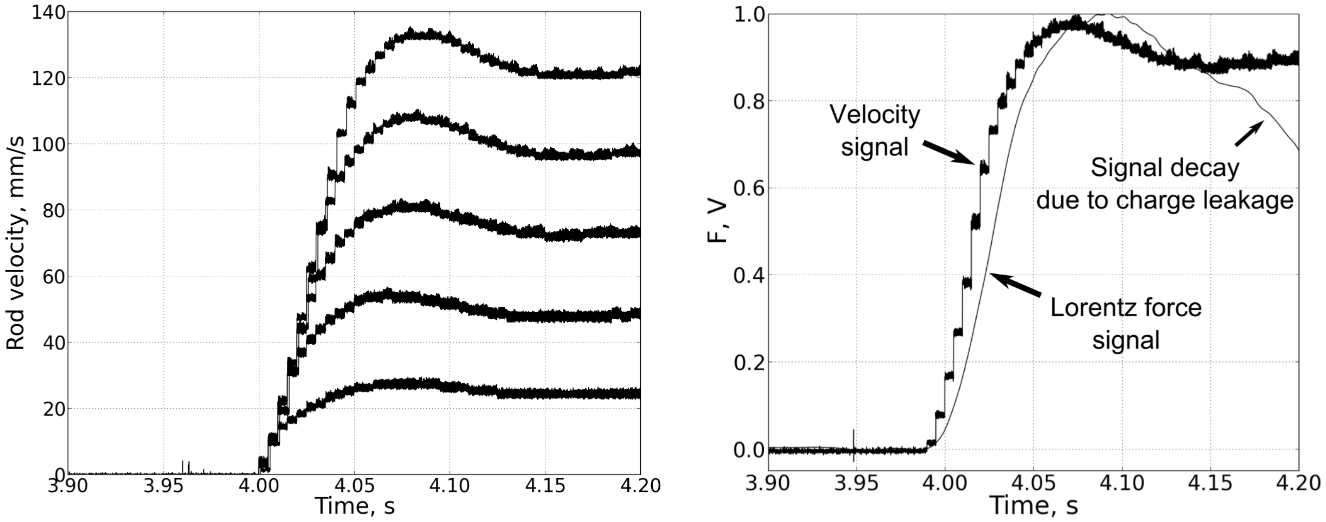

(a) (b)

Figure 22: Velocity input signals and corresponding force response: (a) Five different velocities at which Lorentz force is measured. The acceleration (advection) time τ was always about 80 ms; (b) Typical normalized Lorentz force response. In case of a constant velocity a signal decay due to a charge leakage takes place.

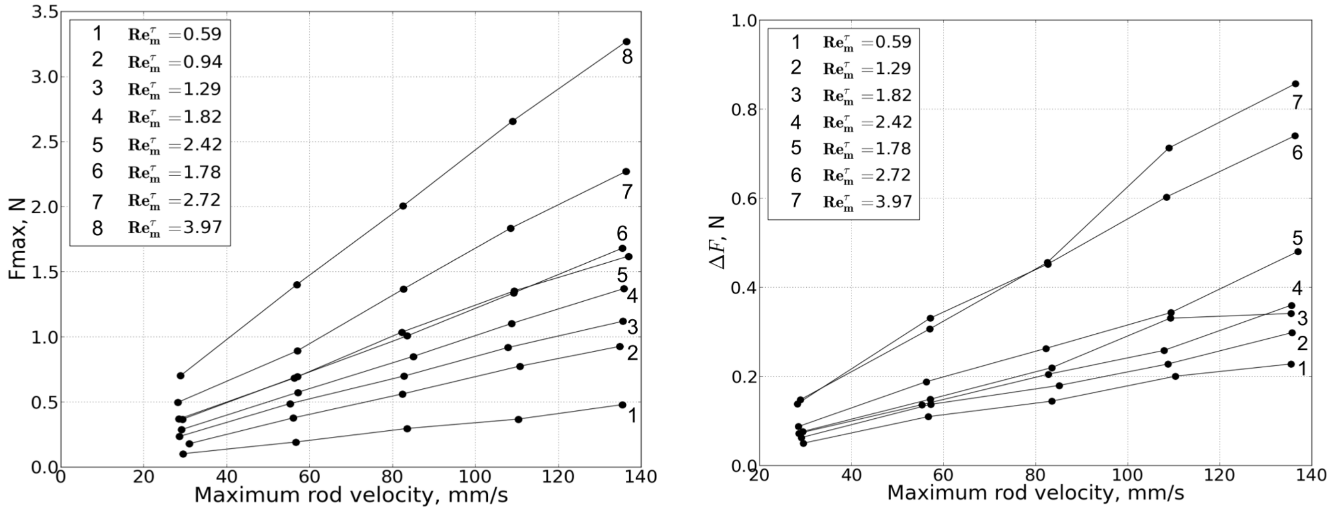

(a) (b)

Figure 23: Lorentz force measurements: (a) Maximum value of the force acting on the rod as a function of velocity at different Re_m^τ; (b) The Lorentz force difference between low Re_m^τ and finite Re_m^τ cases. We note that conventional magnetic Reynolds number $Re_m^V \sim 0.06$.

A presence of the transient phase in the response results in a fact that measured Lorentz force at finite Re_m^τ is smaller than the force obtained at the same velocity at low Re_m^τ (fig.23b). The data in low Re_m^τ case have been obtained in exactly the same way as for the finite Re_m^τ case, but the acceleration of the rod was small enough to have $Re_m^\tau \ll 1$. The difference $\Delta F = F_{Re_m^\tau \ll 1} - F_{Re_m^\tau \sim 1}$ is explained by interaction between B_0 and induced magnetic field b. Apart from a general perturbation of B_0, magnetic field lines are dragged with the conductor leading to a decrease of the product $\vec{V} \times \vec{B}_0$ which is responsible for the generation of the eddy currents. Fig.24a shows that nondimensional Lorentz force F^* decreases as number $\widetilde{Lu}$ becomes higher. F^* is defined as the ratio F/F_{max}, where F_{max} is taken from (57) and parameter $\widetilde{Lu}$ is an analogue of Lundquist number in MHD. It represents a ratio between diffusion time t_{diff} and dissipation time t_{dissip} which a magnetic field needs to convert mechanical energy into Joule heat [10]:

$$\widetilde{Lu}^2 = (\sigma B_0 D \sqrt{\frac{\mu}{\rho}})^2 = \frac{t_{diff}}{t_{dissip}} \tag{58}$$

This points to an idea that by means of Lorentz force it is possible to measure energy which is dissipated inside a conductor and estimate the value of eddy currents [8]:

$$\frac{d}{dt}\int \rho V^2 d\Omega = -\frac{1}{\sigma}\int j^2 d\Omega \sim F \cdot V, \tag{59}$$

Taking $F \sim 1$ N, $V \sim 80$ mm/s, $D \sim 50$ mm, magnet height $l_2 \sim 30$ mm and $\Omega = l_2 \pi D^2/4$, the estimation gives $j \sim 10^5 A/m^2$. We also note that higher Re_m^τ leads to a smaller time response of the system. The response is measured by nondimensional reaction time T_{98}^* (fig.16b) which shows how fast Lorentz force rises from 0 to 98% of its asymptotic value. It was shown that T_{98}^* strongly decreases as a function of Re_m^τ (fig.24b). This stems from a general concept of a frozen state of magnetic field lines in a conductor [8], i.e. an increase in Re_m^τ makes the system "conductor-magnetic field" more stiff and as a consequence nondimensional saturation time T_{98}^* becomes less.

Concluding this paragraph, we would like to note that there is an excellent agreement between measured Lorentz force and the force that was obtained analytically in Section 2 (fig.25). Just to remind, the theory was based on 1D-model of a conducting plate moving through a homogeneous magnetic field with a time-dependent velocity. The considered problem was mathematically equivalent to the heat diffusion problem because the advection term in magnetic field induction equation vanishes. We note that under 1D-approach the Lorentz force dynamics is completely governed by Re_m^τ excluding a possibility to study finite Re_m^V effects. Although, a time response of the Lorentz force can be calculated thereby, its theoretically predicted amplitude needs further experimental verification.

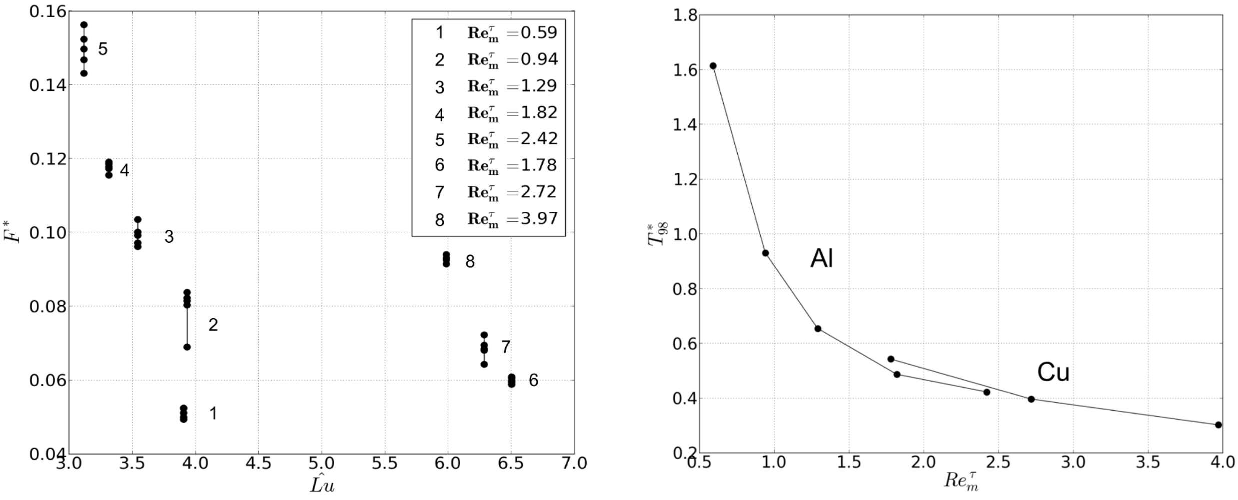

(a) (b)

Figure 24: Nondimensional characteristics of the Lorentz force response: (a) F^* decreases as a function of Lundquist number analogue $\widetilde{Lu}$ since Lorentz force value is proportional to t_{dissip}; (b) reaction time T^*_{98} decreases when magnetic Reynolds number Re^τ_m becomes higher.

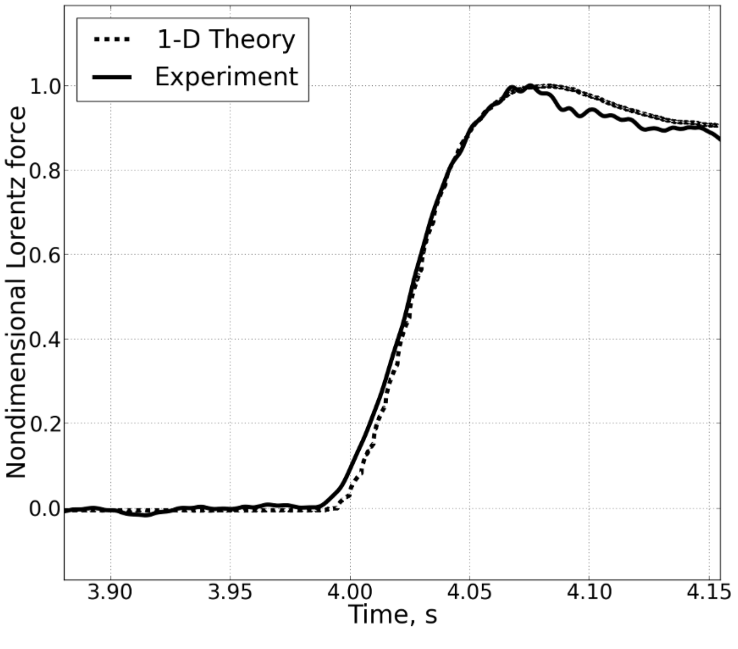

Figure 25: Comparison between experimental and theoretical Lorentz force response (see Chapter 2). A discrepancy between the curves after the end of acceleration phase is explained by the charge leakage in the piezoelectric force sensor that leads to a signal decay [28].

3.3.3 Induced magnetic field measurements

Lorentz force dynamics is based on the magnetic field evolution inside and outside a conductor. Therefore it is important to understand how the conductor changes the initial distribution of B_0. Actually, a perturbation of an imposed magnetic field by a flow motion has been already observed in [29] and [30], but this phenomenon has never been considered as a reason for a Lorentz force measurement error. In order to study this relationship we used a rectangular copper bar (5 x 10 cm) instead of rods. In that case a surface of the conductor is flat and therefore we position magnets closer that improves the signal-to-noise ratio.

Warm-up Experiment Before running a big experiment, it is helpful to check if the used Hall sensors are capable to measure the induced magnetic field of the expected amplitude. For that purpose a simple warm-up experiment has been conducted (fig.26). A testing Hall sensor (denoted as H on fig.26a) was attached to NeFeB 0.1 T magnet and this sensing probe was dragged as a whole with velocity up to 10 cm/s. The Hall voltage as a function of time is shown in fig.27. The induced field appears when the velocity is non-zero. Although the level of noise is high, it is very easy to apply a simple filtering and to extract the desired signal. Since a signal can be clearly seen, it proves that a typical sensor sensitivity of 1 mV/mT is enough to measure the induced field and one can use these sensors in the main experiment.

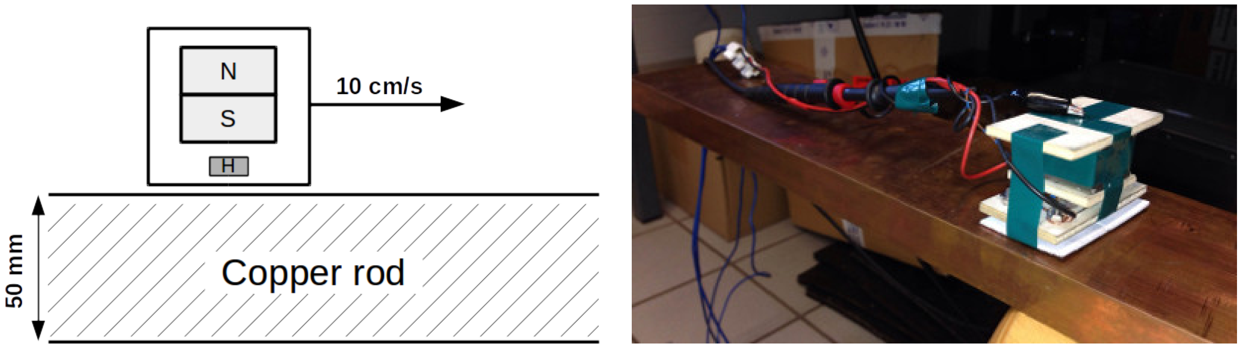

(a) (b)

Figure 26: Sketch (a) and photo (b) of the warm-up experiment. A magnet (0.1 T) with attached testing Hall sensor was dragged along the copper bar with velocity up to 10 cm/s. While moving along the bar the induced magnetic field is expected to be non-zero. The goal is to check if the sensor is sensitive enough to measure the induced field.

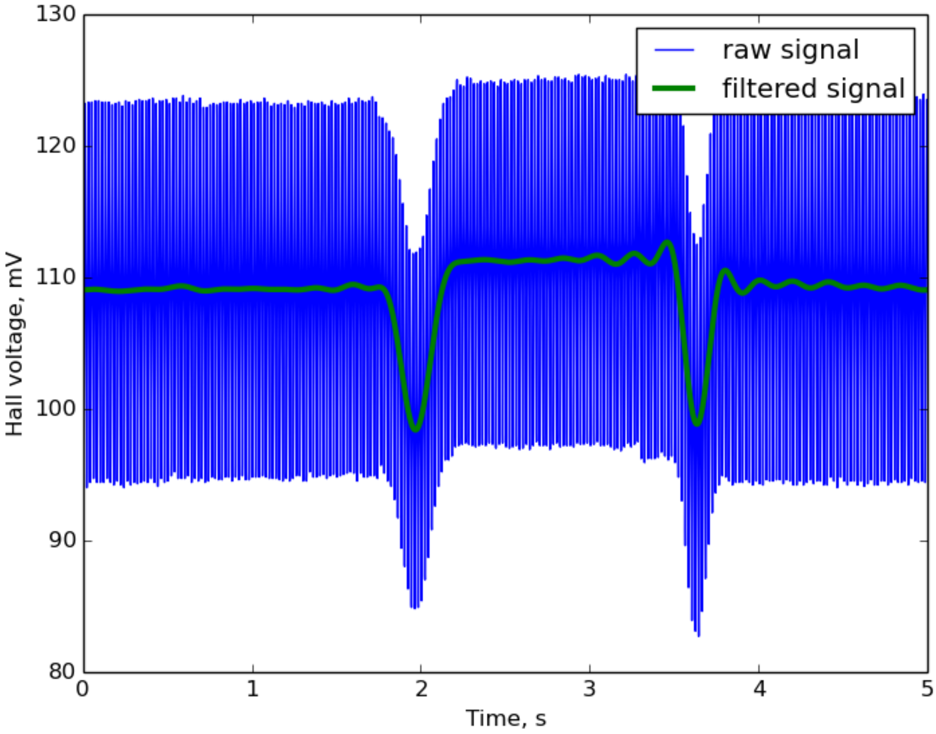

Figure 27: The output signal from the Hall sensor that measures the induced magnetic field in the warm-up experiment. The noise primarily comes from the power grid and can be easily filtered.

Sensor	$V_{out}(B_0 = 0.53T)$, V	K_H, mV/mT
N1	1.83	3.45
N2	1.76	3.32
N3	1.79	3.38
N4	1.76	3.32
N5	1.82	3.43
N6	1.78	3.36
N7	1.85	3.49

Table 6: Calibration factors of the magnetic field sensors

First of all, by Hall sensors we have measured a normal component of $B(t)$ at 7 points along the traveling direction of the bar (fig.28). Calibration factors K_H for magnetic field sensors are listed in Table 6.

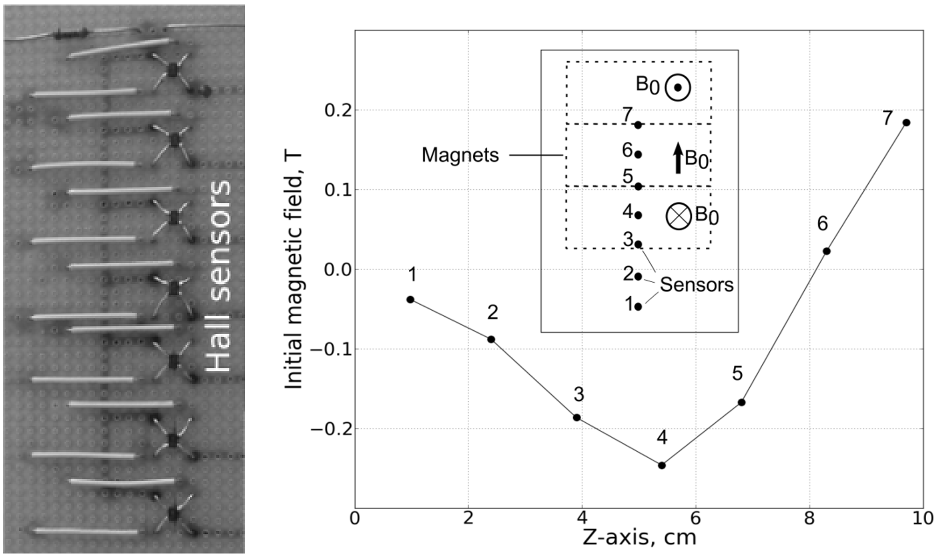

(a) (b)

Figure 28: (a) Photo of the Hall sensors array which is mounted between the rod and magnets to measure the induced magnetic field on the background of the imposed B_0; (b) value of the imposed (initial) magnetic field measured by the Hall sensors array. A relative position of the sensors is marked with black dots and the dotted line represents position of magnets. Z-axis is parallel to the axis of the rod (fig.17).

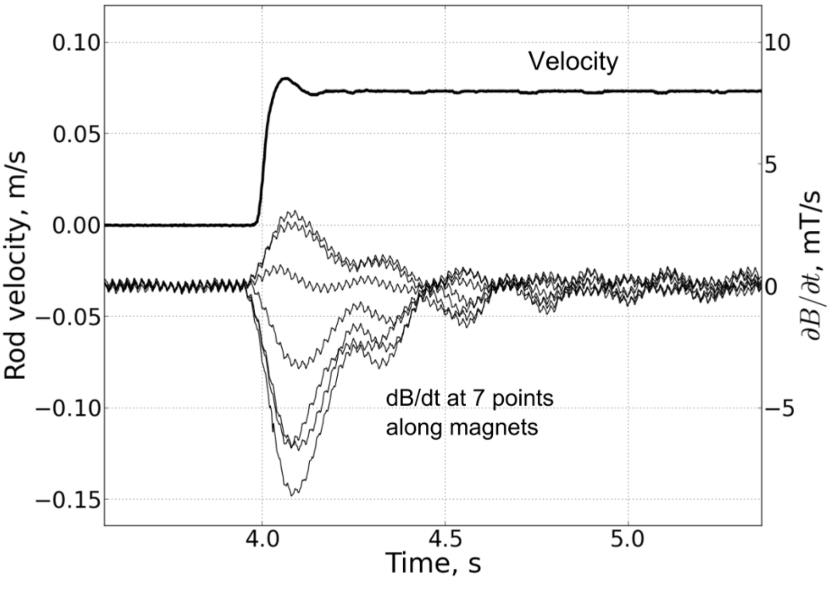

Figure 29: Induced magnetic field measurements using Hall sensors: the onset of motion leads to currents generation whose density is proportional to $\partial b/\partial t$

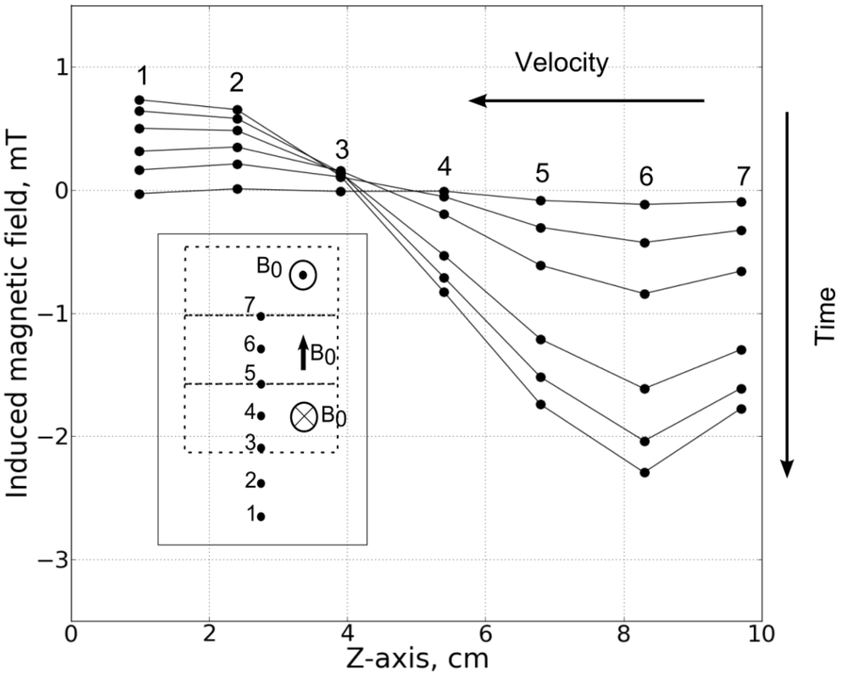

Figure 30: Induced magnetic field measurements using Hall sensors: the bar drags magnetic field lines changing the initial distribution of B_0.

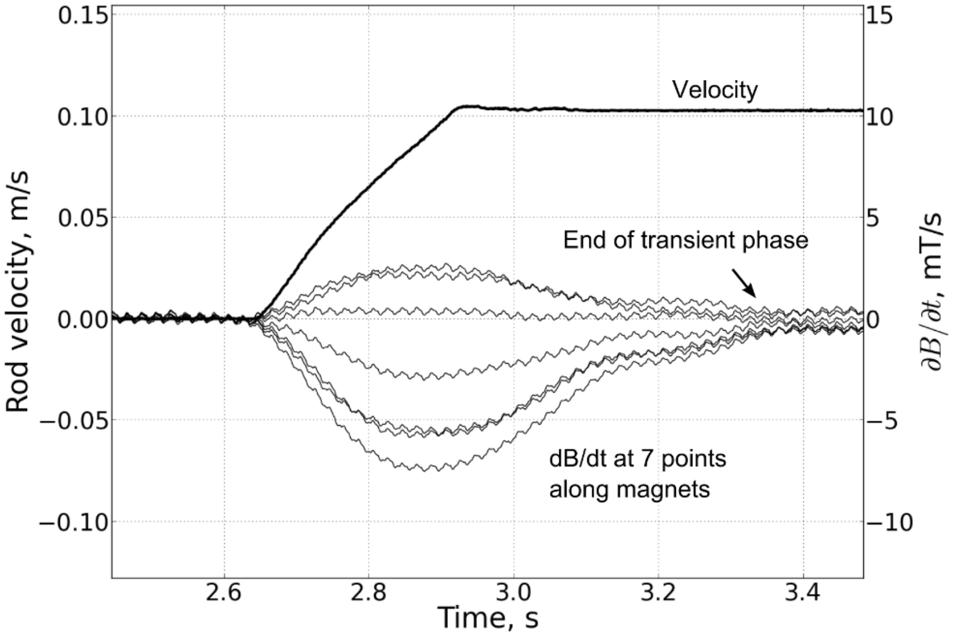

Figure 31: Change of magnetic field $\partial B/\partial t$ at acceleration time $\tau \approx 300$ ms. A generation of the induced magnetic field starts to decrease as soon as the advected imposed field diffuses back to its initial distribution.

Before the onset of the motion there is no current generation and consequently $\partial B/\partial t \approx 0$ (fig.29). But as soon as the bar starts to move (with $V_{max} \approx 80\ mm/s$), eddy currents ensue giving rise to the sweeping of the applied magnetic field (fig.30). We observed that B_0 increases "downstream" the rod motion and decreases "upstream" the rod motion according to fig.16a. As for oscillations of $\partial B/\partial t$, they result from vibrations of the whole construction when the rod is accelerated rapidly along Z-axis. We note that $\partial B/\partial t$ stops to rise at $t \sim t_{diff}$ (fig.31). By that time the magnetic field has already diffused into a material so that all nonstationary processes tend to vanish. Having measured $\partial B/\partial t$ we can verify the current estimation:

$$j = \sigma\varepsilon = -\frac{\sigma}{l_2}\frac{d\Phi}{dt} \tag{60}$$

$$\Phi = \int B dS, \tag{61}$$

where l_2 is thickness of the magnet and S is cross section area of the bar. Combining (60) and (61) and having $\partial b/\partial t \sim 5$ mT/s, $l_2 \sim 30$ mm and $S \sim 5$ cm × 10 cm we obtain $j \sim 5 \cdot 10^4 A/m^2$ that justifies the estimation approach (59).

Generally, an important question may arise here: is it possible to predict a drop in the Lorentz force having measured a change of the applied magnetic field outside a conductor? The answer is yes. Taking into account (57) and assuming the change of magnetic field $B = B_0 - b$ we obtain:

$$F = F_0\left(1 - \frac{b}{B_0}\right)^2, \tag{62}$$

where F_0 corresponds to unperturbed B_0. But for that we need to know the ratio b/B_0 inside a conductor. This ratio can be measured implicitly only. Assuming that b is carried by a current loop with a radius R and this loop circulates in the conductor at the distance z to a Hall sensor that measures b, the ratio between the fields inside and outside the conductor is [31]:

$$\frac{b_{in}}{b_{out}} = \left(1 + \frac{z}{R}\right)^{3/2} \tag{63}$$

In our case the distance z is not more than 5 mm and the radius R equals to a characteristic length of the B_0 decay along the traveling direction of the bar (fig.16). As a rule, this length has an order of magnitude of a gap between magnets and in our case equals to 6 cm that means:

$$b_{in} \approx b_{out} \tag{64}$$

Since the initial distribution of B_0 is well-known, we can estimate the Lorentz force drop according to (62). For copper rod 5 cm in diameter the estimation gives $\Delta F \approx 0.2N$ that is the same order of magnitude of measured values (fig.23b).

3.4 Error analysis

The measurements are affected both by random and statistical errors. Unfortunately, there is no general theory to calculate statistical errors and therefore this point will be discussed for each case separately. As for the random errors, they can be estimated by the standard deviation of the mean [32]:

$$\delta(\bar{X}) = \frac{\delta(X)}{\sqrt{N}}, \tag{65}$$

where N is the number of measurements and $\delta(X)$ is the standard deviation defined as:

$$\delta(X) = \sqrt{\frac{1}{N}\sum_{i=1}^{N}(X_i - \bar{X})^2}, \; \bar{X} = \frac{1}{N}\sum_{i=1}^{N} X_i \tag{66}$$

So, a measured value X can be represented as:

$$X = \bar{X} \pm \delta(\bar{X}) \tag{67}$$

It means that if the values X_i are normally distributed, one more single measurement X_{i+1} will be within the interval $\pm\delta(\bar{X})$ with the probability 68 % [32]. It is worth mentioning that nowadays there are debates over the best representation of the data scattering. Some authors prefer to use $N-1$ instead of N in the definition of standard deviation [33]. Likewise it is possible to show scattering by the *probable error* $PE = 0.67\delta(X)$. For the sake of consistency, traditional definitions (66) and (67) are used in the present work.

The propagation of uncertainty is calculated as follows. If y is a function of n variables x_i and each brings the random error *independently*, the total error $\delta(y)$ is:

$$\delta(y) = \sqrt{\sum_{i=1}^{n}\Big(\frac{\partial y}{\partial x_i}\delta(x_i)\Big)^2} \tag{68}$$

3.4.1 Lorentz force measurements

3.4.1.1 Random errors The Lorentz force was measured at different bar velocities and bar diameters. Fig.32 shows that the precision of the force measurement is not worse than $\pm 18mN$ and of the rod velocity is not worse than $\pm 0.8mm/s$. From (65) we obtain:

$$\delta(\bar{F}) = 5.7 \; mN, \; \delta(\bar{V}) = 0.3 \; mm/s \tag{69}$$

The measured force F was compared with the force calculated from the linear law $F_{lin} = kV$ which works well as long as $Re_m \ll 1$. The relative measurement uncertainty of the factor $k = F_{lin}/V$ is calculated using (68):

$$\eta(k) = \frac{\delta(\bar{k})}{k} = \sqrt{\Big(\frac{\delta(\bar{F})}{F}\Big)^2 + \Big(\frac{\delta(\bar{V})}{V}\Big)^2} \le 1.5\% \tag{70}$$

Then the relative uncertainty of F_{lin} is:

$$\eta(F_{lin}) = \sqrt{\eta(F)^2 + 2\eta(V)^2} \le 1.8\% \tag{71}$$

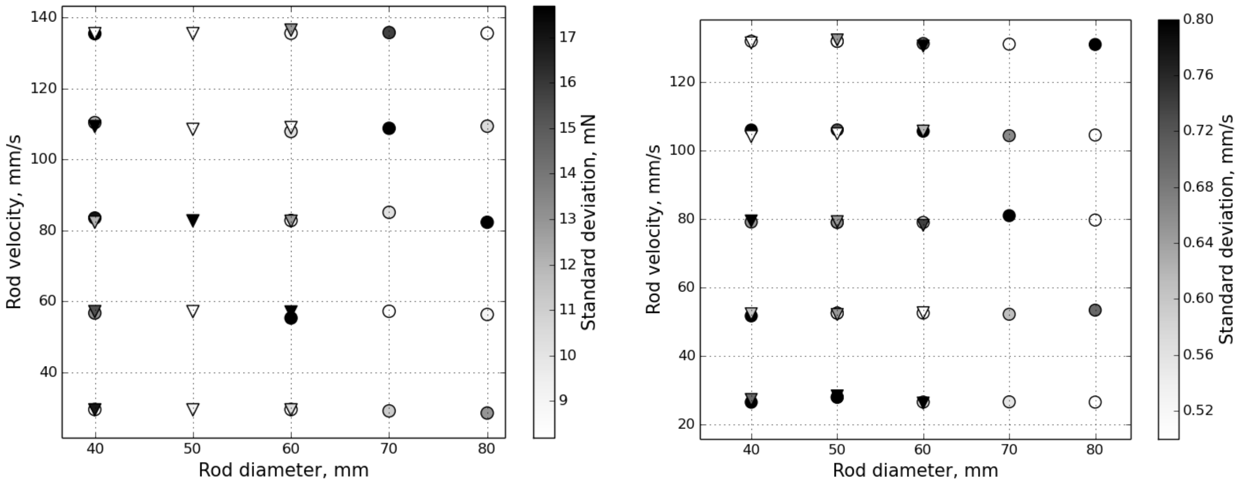

(a) (b)

Figure 32: Standard deviation of the Lorentz force (a) and velocity (b) measurements. Circles stand for aluminium rods, triangles - for cupper rods.

Finally, one can calculate the measurement error of $\Delta F = F - F_{lin}$:

$$\delta(\Delta F) = \sqrt{\delta(F_{lin})^2 + \delta(F)^2} \leq 10.7mN \tag{72}$$

3.4.1.2 Statistical errors Unfortunately, no additional reference measurement system was installed to reveal the statistical errors. Therefore we list the error sources only without accurate evaluation.

- *Charge leakage.* To eliminate this effect the measured value of the Lorentz force was multiplied by the factor 1.05 calculated from (56). However it does not guarantee the absence of the error because (55) is a modelling equation and the real performance can be different.
- *Temperature variation.* The accuracy of the measurements suffers from the fact that the imposed magnetic field depends on temperature:

  $$B(T) = B(T_0)(1 - \iota(T - T_0)) \tag{73}$$

  From [34] a corresponding coefficient $\iota \approx 10^{-3}K^{-1}$. Assuming that a maximum temperature variation within one measurement day was not bigger than 5 K, from (73) we obtain that the variation of magnetic field is less than 0.5%.
- *Sensor non-linearity and temperature coefficient of sensitivity.* These two error sources come directly from the sensor characteristics. According to the manuals the corresponding errors do not exceed 1%.

3.4.2 Induced magnetic field measurements

The induced magnetic field is measured by magnetic field sensor CYTHS124. As for the *random errors*, the uncertainty of the measurements $\delta(b) = 0.1mT$ that leads to the relative error $\eta(b) \leq 4\%$. The *statistical errors* caused by sensor non-linearity and temperature sensitivity are 2% and 0.6% correspondingly.

3.5 Conclusions

To summarize, when Lorentz force velocimetry is used to measure a flow velocity, a measurement error can be big in case of high speed or non-stationary flow. For example, in the considered case the error has the same order of magnitude with the measured values (fig.23). This problem has been studied in a model experiment where a difference in Lorentz force amplitude at low Re_m^τ and finite Re_m^τ was measured. Experimental setup comprises moving Al and Cu conducting solid rods ($\sigma = 20\ MS/m$ and $59\ MS/m$ correspondingly), which were accelerated up to 1.6 m/s^2 within 80 ms. The rods were initially placed in a transverse nonhomogeneous magnetic field up to 1 T. Due to a rapid velocity change a finite value of Re_m^τ was reached so that diffusion and advection of magnetic field became comparable and the linear dependence between Lorentz force and velocity was violated. This should be considered when evaluating the measurement error. Studied effects in solid conductors are similar to some extent to effects in a conducting fluid but with some distinctions. For example, in a fluid flow there are also electric currents induced in homogeneous part of magnetic field in a plane normal to the flow direction. These currents close through the Hartmann layers and layers which are parallel to the field. However, the main effects for solid conductors at finite Re_m numbers take place in both cases. Moreover, fringing effects contribute to the Lorentz force much higher than the effects in the area of homogeneous magnetic field. Therefore the discussed problem can be applied to velocity measurements of liquid nonstationary flows.

4 Experiments with liquid sodium

Experiments with solid conductors described in Chapter 3 have two big advantages. First, the velocity field is uniform and can be precisely controlled. Second, electrical conductivity is approximately 10 times higher than the conductivity of the liquid metals. Therefore it is easier to measure the Lorentz force and the induced magnetic fields. However, a serious drawback is that it is not a real MHD configuration. Everywhere, from stars to liquid metal batteries and continuous steel casting there is a liquid conducting medium in turbulent motion. Interaction with magnetic field gives rise to many interesting effects. If there is no turbulent fluid flow in a modeling experiment, these effects cannot be studied. Thus it is essential to have an experiment where a high-speed liquid metal flow can be obtained.

4.1 Problem definition

For convenience let us write down the basic equation of Lorentz force velocimetry [13,34–36] and state the main problem once again:

$$\vec{F}_L = \int_\Omega \vec{j} \times \vec{B}\, \mathrm{d}\Omega = k(Re_m, B)\sigma V B^2 \tag{74}$$

Here Ω stands for a characteristic volume where eddy currents j flow, B is an imposed magnetic field, $k(Re_m, B)$ is a calibration factor defined experimentally, V is a conductor velocity and σ is conductivity. If V is high the imposed field becomes distorted by the flow and the linear dependence between Lorentz force and velocity fails. This process is governed by magnetic Reynolds number Re_m. If $Re_m \ll 1$ then there is no deviation from the linear law for velocity (74). But if $Re_m \gg 1$ or even $Re_m \sim 1$, magnetic field lines become frozen in a moving conducting material that leads to a strong field expulsion [37]. This phenomenon is usually attributed to the strong induced (secondary) magnetic fields b in the flow. The field b carried by eddy currents can be high enough to alter significantly a distribution of the imposed field B by expelling it from the medium. If a magnetic field is in the expelled state, $\vec{j} \times \vec{B}$ product goes down and consequently the Lorentz force decreases. In order to check if the Lorentz force velocimetry is applicable for conducting fluids at high Re_m one has to obtain a high-speed liquid metal flow at laboratory conditions. Usually this is very difficult. From (54) it is clear that one should consider a liquid metal with a high conductivity and propel it with a high velocity. A promising solution is to study a non-stationary liquid sodium flow in a toroidal channel (e.g. [38]). The flow obtained in this setup has outstanding characteristics: the maximum magnetic Reynolds number $Re_m = 30$ and hydrodynamic Reynolds number $Re = 2.8 \cdot 10^6$. Although the flow is non-stationary, these conditions are very suitable to study LFV at high Re_m. Summing up, we want to measure two key values as a function of time and Re_m: the induced magnetic field and the Lorentz force. *The ultimate goal* is to obtain an experimental proof for the fact that the dependence of the Lorentz force on velocity deviates from the linear law at finite Re_m and to link this phenomenon with the experimentally observed magnetic field expulsion.

4.2 Experimental setup

4.2.1 Toroidal channel

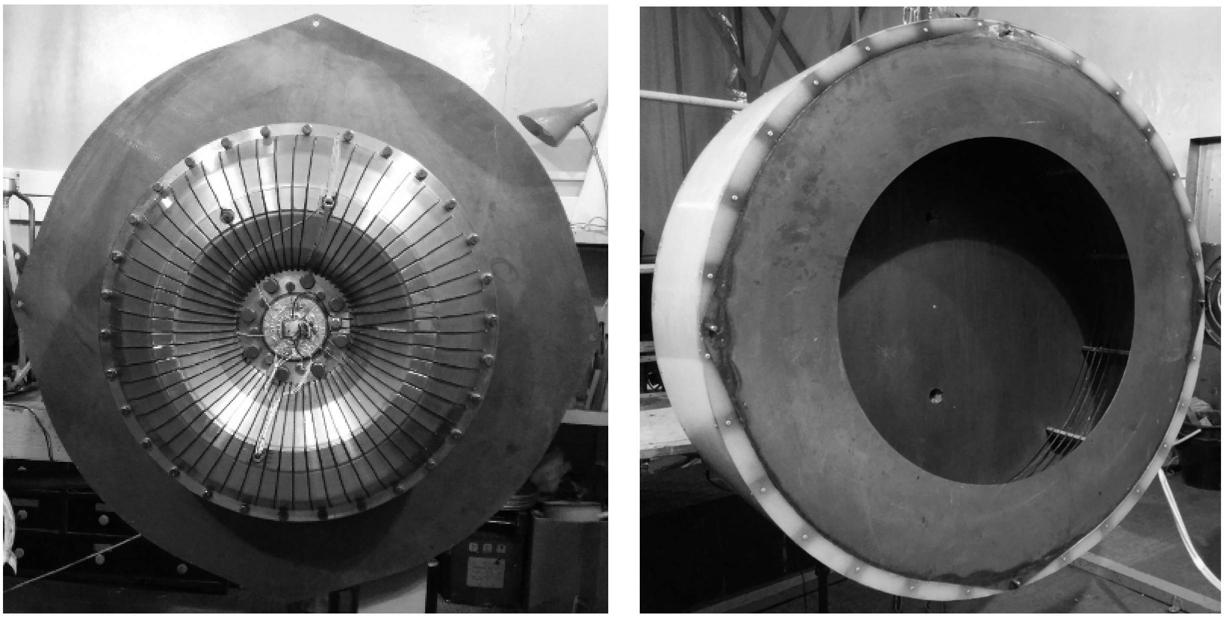

(a) (b)

Figure 33: Experimental setup: (a) Titanium toroidal channel filled with liquid sodium. Rotation axis is horizontally aligned. (b) Thermal insulation shell with heating coil inside.

The flow is obtained in the setup assembled in the Institute of Continuous Media Mechanics (Perm, Russia) [39] (fig.33). The toroidal channel is made of titanium alloy and filled with liquid sodium which is heated up to 107 ^oC. Liquid sodium has the following properties: melting temperature $T_{melt} = 97.3\ ^oC$, conductivity $\sigma = 10^7\ S/m$, density $\rho = 993\ kg/m^3$, kinematic viscosity $\nu = 0.87 \cdot 10^{-6}\ m^2/s$ [40]. The major and the minor radii of the torus are $R = 0.18\ m$ and $r_0 = 0.08\ m$ correspondingly (fig.34). The channel rotates inside an iron shell covered with thermal insulating material. This construction allows preventing undesirable heat and magnetic flux leakages. The torus is connected to a motor by a belting gear so that a generated power goes into the channel rotation. The motor has the power of 7 kW. Actually, 3 kW is already enough to have a rotation frequency of 40 Hz. However, an excessive power is needed to overcome 2 zones of resonance (20-25 Hz and 40-45 Hz). When a desired rotation frequency is reached the channel is braked by a hydraulic system. The braking time does not exceed 0.5 s and at the end of the braking phase the velocity of liquid sodium reaches its maximum that leads to high Re ($= Vr_0/\nu$) number and high Re_m ($= \mu\sigma V r_0$) number.

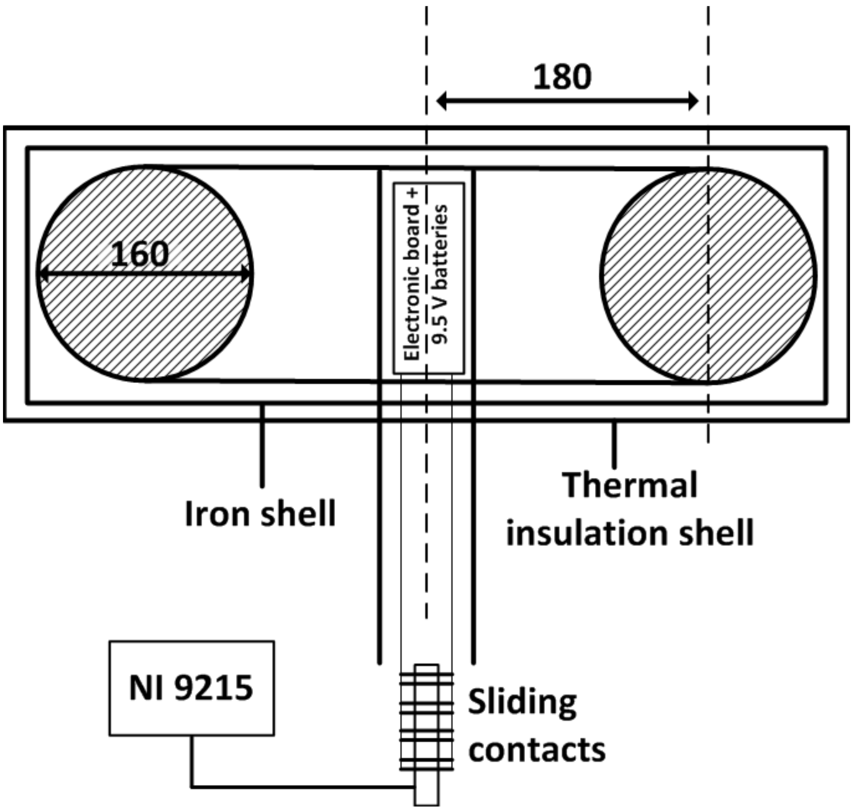

Figure 34: Sketch of the setup (driving mechanism is not shown). The titanium channel rotates inside static iron and thermal insulation shells. The electronic board is mounted inside the rotating shaft. All signals are acquired by the system of sliding contacts. Data acquisition system is NI 9215 with 100 kHz sampling rate.

4.2.2 Velocity measurements

The velocity signal is recorded by two-axis Vives probe installed on the channel wall [39]. It consists of a small 2 x 2 x 10 mm NdFeB magnet ($B = 0.4\ T$) and 4 electrodes made of tinned copper. The direct output voltage which is of the order of 100 $\mu V m^{-1} s$ is fed into a differential amplifier AD8221 with a gain of 100. The amplifier and a set of 9.5 V batteries are located inside the hollow rotating shaft. Since the Vives probe takes part in rotation an array of sliding contacts was used to connect the output signal to the data acquisition system. Before the brake the velocity of the liquid sodium equals to channel rotation velocity V_0, whereas after the brake this velocity is shared between toroidal V_{tor} and poloidal V_{pol} components. The initial kinetic energy is distributed such that $V_{tor} = 0.69V_0$ and $V_{pol}/V_{tor} = 0.18$ at the end of the braking phase. The velocity signals are recorded by 16-bit NI 9215 data acquisition system with sampling frequency 100 kHz.

4.2.3 Induced magnetic field measurements

As it was explained in Chapter 1, the induced magnetic fields play an important role in high Re_m flows. These fields can be strong enough to make the imposed field “frozen” in a conductor so that it runs away with the flow [41]. This phenomenon is called *magnetic field expulsion* and it plays a central role in the actual experiments. Fig.35b shows a concept of the experiment. There is a sensing probe that can take part in channel rotation. When the channel is braked, the sodium velocity rises up that leads to the generation of the induced magnetic field. This field is measured by the sensing probe shown in fig.35a. The probe consists of 2 single-axis high-temperature GaAs Hall-sensors CYTHS124 (fig.36) with sensitivity 0.5 V/T and a small cylindrical NdFeB magnet that imposes 0.45 T on its surface. Sensors were orthogonally aligned so that 2 magnetic field components can be measured simultaneously. Although the applied field created by the NdFeB magnet is strong, the induced field is expected to be several orders of magnitude smaller. In order to measure variations of the latter a multi-channel amplifier was manufactured (fig.37). This amplifier has adjustable gain and offset so that a small variation of the field can be acquired. The probe is mounted on the rotating channel by a conical thread R 1/4″ (fig.38). Its position is diametrically opposite to the location of the Vives probe. Sliding contacts are used to connect the output cables to the data acquisition system. Using this probe one can measure contactless b^{tor} and b^{pol} created by V_{tor} and V_{pol} correspondingly after the brake at different rotation frequencies. While channel is rotating all signal cables and mainly the probe experience a centrifugal force F_c which can be calculated as:

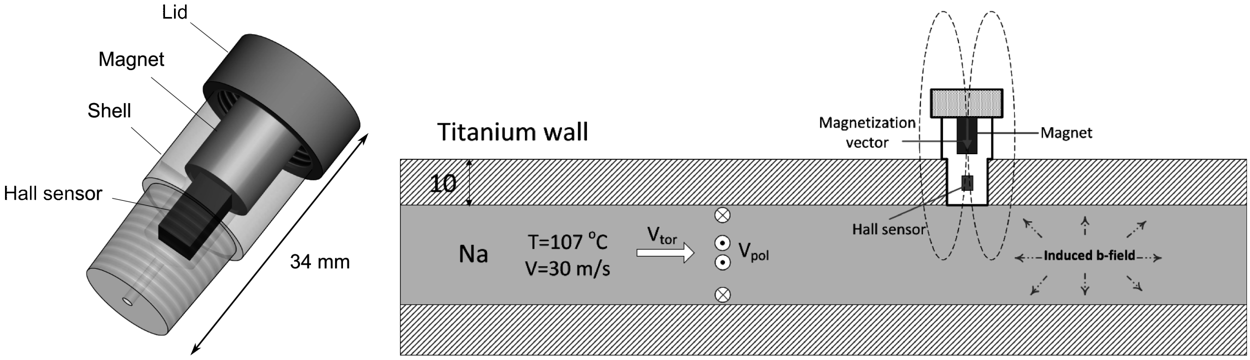

(a) (b)

Figure 35: Probe for induced magnetic field measurements. (a) 2D-Hall sensor and NdFeB magnet (10 x 15 mm) are placed inside 34 mm aluminium shell. The probe is mounted on the rotating channel; (b) after the brake the relative sodium velocity rises up to 30 m/s that leads to the generation of the induced magnetic field b. Both toroidal b^{tor} and poloidal b^{pol} components are measured.

$$F_c = m_p r_p 4\pi^2 f_{rot}^2 \approx 200\ N, \tag{75}$$

where $m_p = 20\ g$ is the mass of the probe, $r_p = 18\ cm$ is the distance between the torus center and the probe location and $f_{rot} = 40\ Hz$ stands for the maximal rotation frequency. During the brake the experienced force is:

$$F_b = m_p \frac{2\pi r_p f_{rot}}{t_b} \approx 2\ N, \tag{76}$$

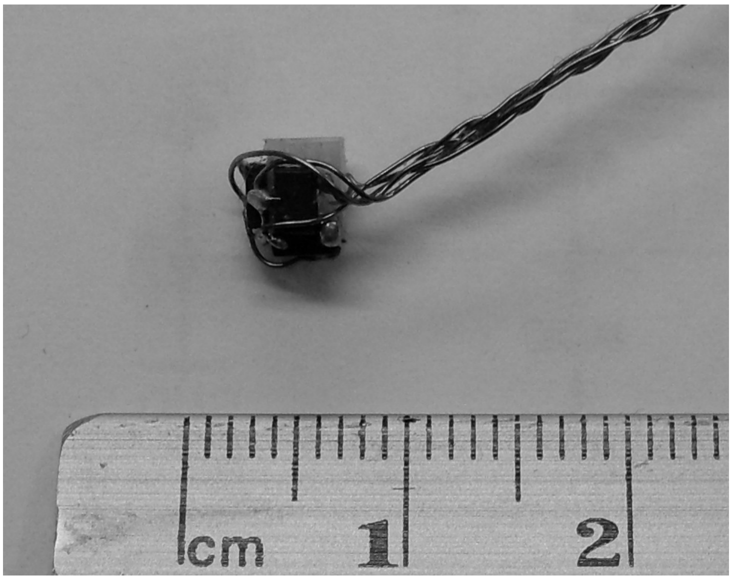

Figure 36: 2D Hall sensor for simultaneous measurements of the toroidal and the poloidal components of the induced magnetic field. The size of the sensor does not exceed 4 *mm*.

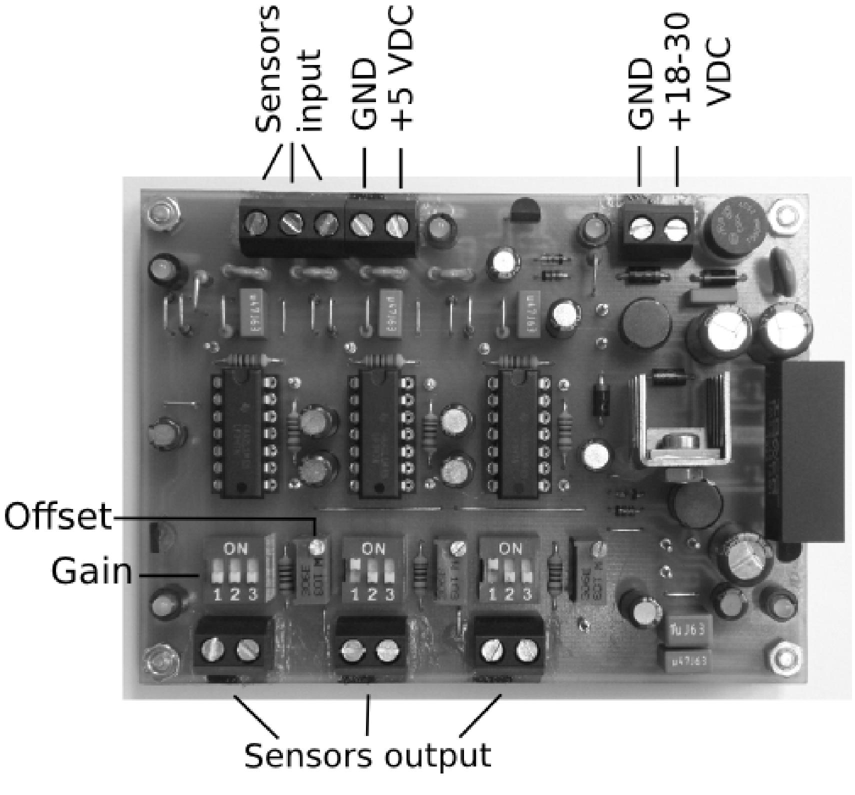

Figure 37: Multi-channel amplifier with adjustable gain and offset. It has three main tasks: to stabilize the supplying voltage for the Hall sensors, to subtract an offset caused by the strong imposed magnetic field and to amplify the signal which is proportional to the induced field.

where t_b is a typical breaking time which does not exceed 0.5 s. It easy to see that $F_b \ll F_c$. Therefore centrifugal forces have to be considered as a main possible reason of a break of the probe or its cables. Although the centrifugal load might not be thought as a serious threat, it can cause problems after many experimental runs. For example, the coil which is twisted around the titanium channel was stretched during rotation and touched a static thermocouple. As a consequence, the coil was damaged and one lost an opportunity to use an additional toroidal magnetic field. To diminish the probability of a failure the output cables of the probe were twisted around the external coil (fig.38).

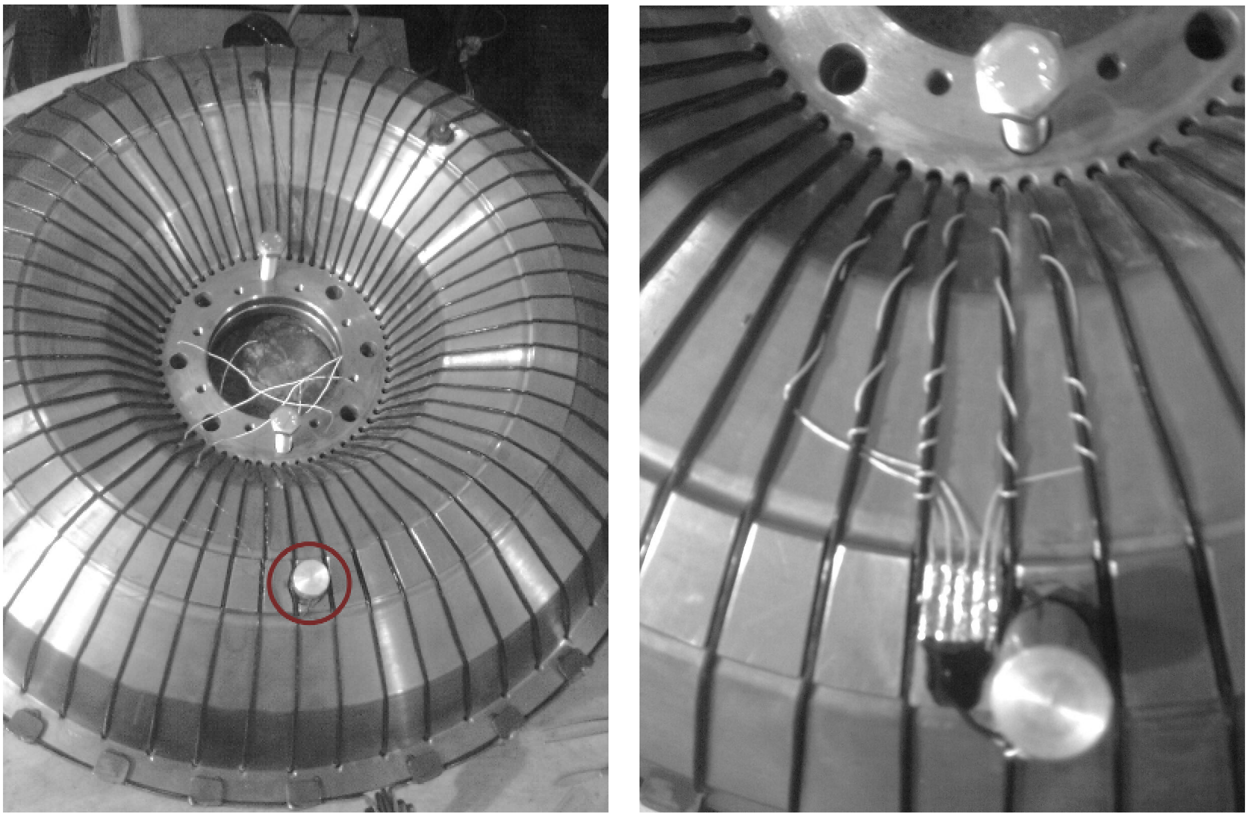
(a) (b)

Figure 38: (a) The probe (encircled by red line) is mounted directly on the titanium channel; (b) to prevent breaking of the wires, they were twisted around the external coil which is supposed to generate an additional toroidal magnetic field. The coil was damaged in an accident.

4.2.3.1 Probe installation The installation of the probe consists of several steps. A place on the channel where the probe must be installed is initially occupied by a dummy bolt. Since the bolt is partially immersed in the solidified sodium, to remove it one has to melt sodium locally. The melting process should go in an argon atmosphere. This prevents oxygen from falling into the remaining gap. Otherwise oxygen will react with sodium and titanium by creating oxides that worsens quality of the experiment. After the dummy probe is removed, the sensing probe is installed. Then a vacuum pump with nitrogen traps is used to remove atmosphere from the channel completely. This step is essential because after the sodium is heated up, pressure of remained gases reaches high values that might lead to an accident. Once the sodium is completely molten and all gases are pumped out, the channel can be used for experimental runs.

4.2.4 Lorentz force measurements

Lorentz force measurements are the most important part of these experiments. They will answer a question whether LFV-methods are applicable at high Re_m flows. The sketch of the experiment is shown in fig.39b. We need a probe that is capable to measure two components of the Lorentz force. To link the obtained results with the *expulsion* phenomenon one has to perform simultaneous measurements of the induced field at the same place where the force was measured. Also a box with sensors has to be properly protected from overheating because the ambient temperature is about 100 ^oC. Since it is not possible to mount a Lorentz force measurement system on the rotating channel because of huge centrifugal forces, a static non-rotating probe is used (fig.39a, fig.40a). This probe consists of a piezoelectric force sensor PCB 208C01, 2 single axis magnetic field sensors CYTHS124 (fig.40b), temperature sensor Pt 100, NdFeB cubic 30 mm magnet and the air cooling system. To get rid of the noise coming from 220 V AC grid power all sensors are supplied with 24 DC voltage from lead 9Ah batteries. To have an access to the rotating channel a square hole in the iron and thermal insulating shells was made (fig.41a). The probe is installed at the distance $L = 20$ mm from the channel (fig.39b). Unfortunately, it is not possible to come closer because of the pipeline through which the channel is filled with liquid sodium. A piezoelectric sensor is used because it fits dynamic measurements very well. Also one more interesting feature of these sensors is their insensitivity to all types of undesirable offsets and drifts which may be caused by temperature variations. The charge leakage always makes an offset zero without affecting a measured dynamic signal. The sensitivity of the sensor is 0.1 V/N and the output signal is fed into a ICP 682A02 signal conditioner.

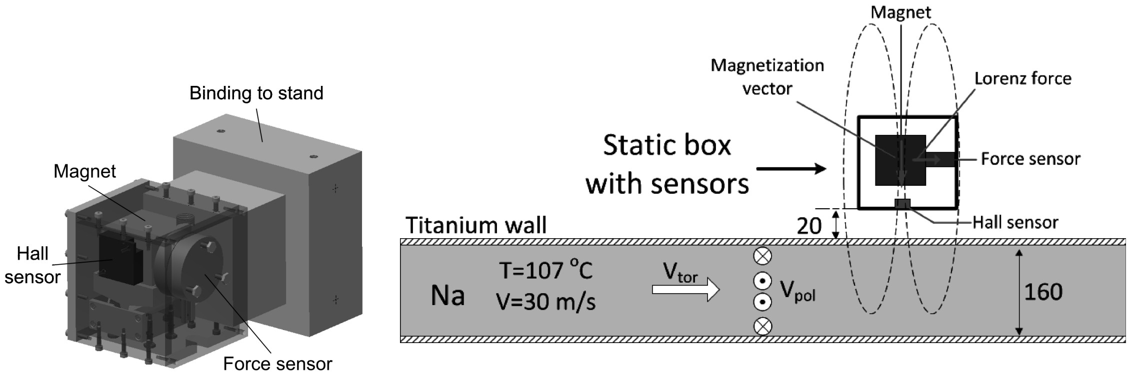

(a) (b)

Figure 39: Measurement probe installed in the vicinity of the rotating channel. (a) The probe consists of a temperature sensor, force sensor and 2 single-axis Hall sensors. The imposed field created by the cubic 30 mm NdFeB magnet is 0.45 T on the magnet surface; (b) sketch of the channel (side view) with the measurement probe. Rotating the probe by 90^o one can measure F_{tor} and F_{pol} components of the Lorentz force separately.

A few comments about temperature control. First of all, it is important to prevent liquid sodium from overcooling or overheating. On the one hand, if sodium temperature is too low vacuum bubbles appear inside the torus. These bubbles can flow in the vicinity of Vives probe while the velocity data are being acquired that results in a contaminated

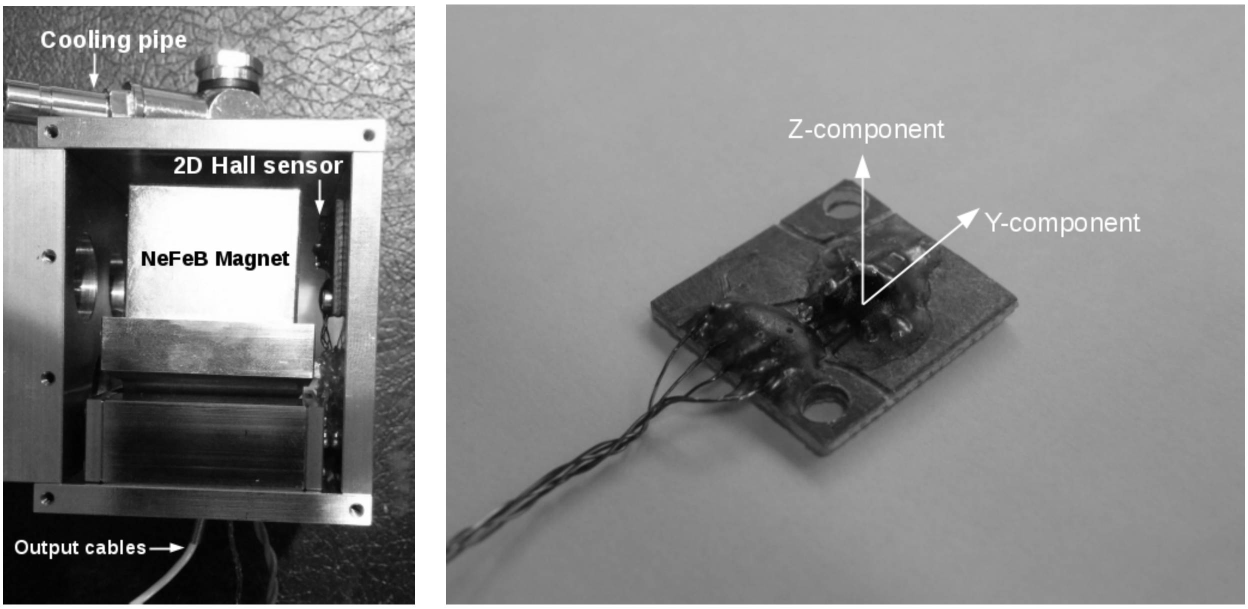

(a) (b)

Figure 40: (a) Photo of the probe for simultaneous measurements of the Lorentz force and the induced magnetic field (force sensor is hidden behind the magnet); (b) photo of the 2D Hall sensor which is installed inside the probe. Y-direction corresponds to the poloidal motion inside the channel, Z-component - to the rotation axis.

(a) (b)

Figure 41: (a) A square hole in the thermostatic shell was made to have an access to the rotating channel. (b) A probe is carried at the tip of a robust aliminium cantilever. A thick layer of basalt wadding is used to reduce the heat flux through the walls of the probe.

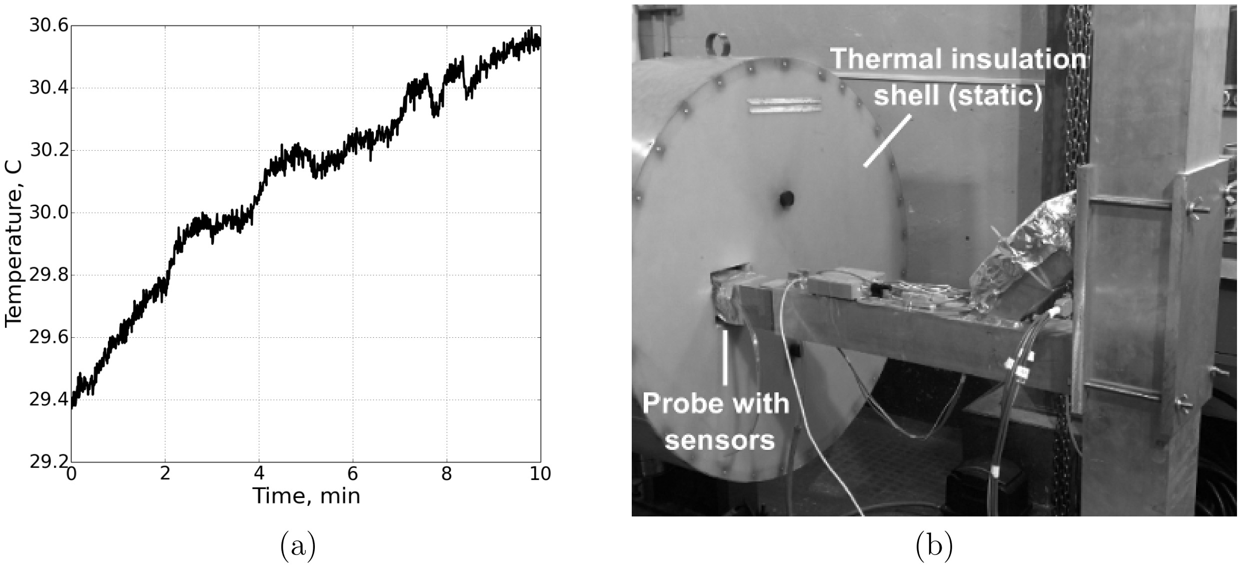

(a) (b)

Figure 42: (a) Temperature variations inside the probe for the Lorentz force measurements. By using an air cooling system and the basalt wadding two main goals are achieved: temperature remains almost constant with time and stays at sufficiently low value to prevent sensors from overheating. (b) Photograph of the stand carrying the probe.

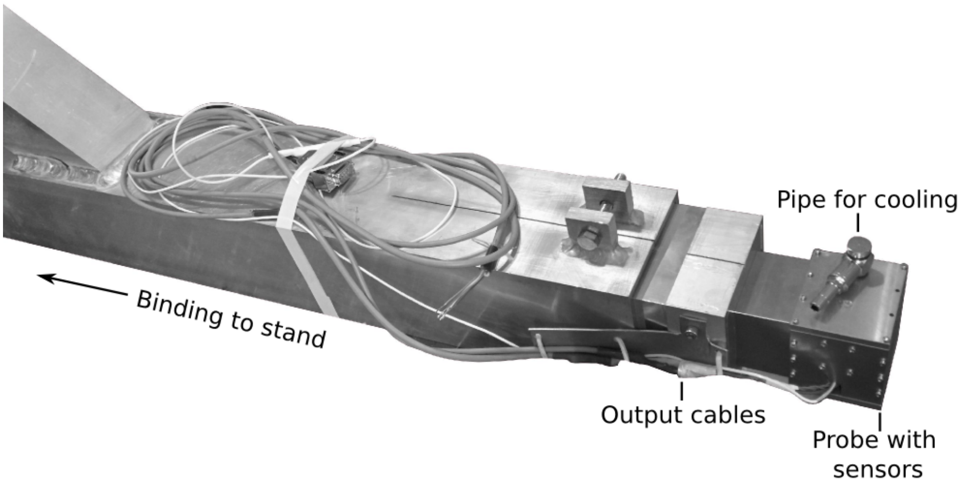

Figure 43: Aluminium cantilever which holds the probe with sensors. Air is supplied by the pump through the pipe mounted on the steel shell. The cantilever has an adjustable geometry and is connected with the stand by massive bindings.

signal. On the other hand, if temperature is too high, the sodium overexpansion takes place. It leads to a leakage of the hot metal at the end of the braking when the pressure inside the torus is maximum. Sodium temperature is measured by a thermistor immersed in the metal. The working temperature inside the channel varied in the range of 102-107 ^oC. Apart from that, it is necessary to keep the temperature inside the measurement probe constant. Although the force signal is not affected by the temperature variations, magnetic field values depend on them. Thermistor Pt 100 is installed inside the probe

(a) (b)

Figure 44: The stand is connected to the concrete ground by 4 massive anchor bolts. This solution is very effective because by adjusting the nuts one can align the stand horizontally and detach it from the vibrating steel layers adjacent to the ground.

for temperature control. It has the sensitivity 0.07 $V/^oC$ and can operate from 0 to 150 ^oC. To decrease the heat flux through the probe walls it was wrapped by a thick layer of basalt wadding (fig.41b). As a result, the temperature inside the box with sensors was almost constant. Fig.42a shows that temperature variation is about 0.8 ^oC within 10 min. Taking into account that each measurement takes 10 s, the influence of temperature on the output signal can be excluded from future analyzes. An aluminium stand (fig.42b) holds a rigid cantilever (fig.43) that carries the probe. The stand is fastened directly to the concrete floor by M12 anchor bolts shown in fig.44.

4.3 Organizational issues

This experiment has been conducted in the frame work of a collaboration between *Technical University Ilmenau* in Germany and *Institute of Continuous Media Mechanics (ICMM)* in Russia. The aluminium stand and all measurements probes have been designed and manufactured in TU Ilmenau and were brought to Russia. The stand was sent separately one month before the expected start of the measurements. For a successful export of the experimental equipment abroad the following documents have been prepared:

1. *Carnet* documents from custom office in Suhl (Germany)
2. Official statement about non-military project objectives
3. Official confirmation that TU Ilmenau agrees to pay for consumable materials bought in ICMM
4. Official document about collaboration between TU Ilmenau and ICMM
5. Export list with a corresponding project description for shipping company
6. Export list with a corresponding project description for airlines

4.4 Results

4.4.1 Velocity measurements

Each experimental run was repeated 10 times to have statistically reproducible data. Although the toroidal velocity depends on rotation direction whereas the poloidal velocity does not, one observed slight asymmetry between clockwise and counter-clockwise rotations. The reason is that the Vives probe was slightly turned around its rotation axis by the angle ϕ. Therefore the toroidal component contributes to the poloidal one. To modify velocity signals one has to solve the following equations:

$$\begin{bmatrix} V^+_{tor} \\ V^+_{pol} \end{bmatrix} = M(\phi) \times \begin{bmatrix} V_{tor} \\ V_{pol} \end{bmatrix}, \begin{bmatrix} -V^-_{tor} \\ V^-_{pol} \end{bmatrix} = M(\phi) \times \begin{bmatrix} -V_{tor} \\ V_{pol} \end{bmatrix} \tag{77}$$

$$M(\phi) = \begin{bmatrix} cos(\phi) & sin(\phi) \\ -sin(\phi) & cos(\phi) \end{bmatrix} \tag{78}$$

Here we look for odd and even solutions V_{tor} and V_{pol} correspondingly based on velocity signals obtained at clockwise (+) and counter-clockwise (-) rotation directions. After this correction the toroidal component becomes higher and the poloidal one becomes smaller because there is no kinetic energy transport between each other. The calculated angle $\phi \approx 10^o$ and the corrected velocity signals are shown in fig.45.

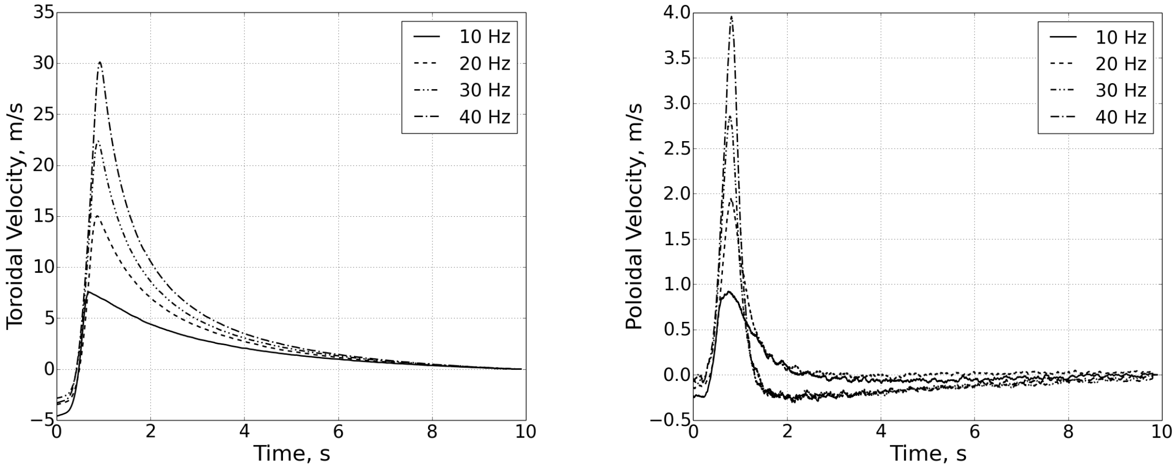

(a) (b)

Figure 45: Mean values of toroidal (a) and poloidal (b) velocity components at different rotation frequencies. Time $t = 0$ corresponds to the beginning of the braking phase. It takes approximately 0.5 s until the channel rotation stops completely and the sodium velocity reaches maximum relative to the channel wall. After the brake the flow decays within 10 s approximately.

Maxima of mean values depend linearly on the rotation frequency (fig.46). At $f_{rot} = 40\ Hz$ $V_{tor} \approx 30\ m/s$ and $V_{pol} \approx 5\ m/s$ that leads to magnetic Reynolds number $Re_m \approx 30$ and hydrodynamic Reynolds number $Re \approx 3 \cdot 10^6$. A level of velocity pulsations also increases if the rotation rate becomes higher (fig.47). These data will be processed further

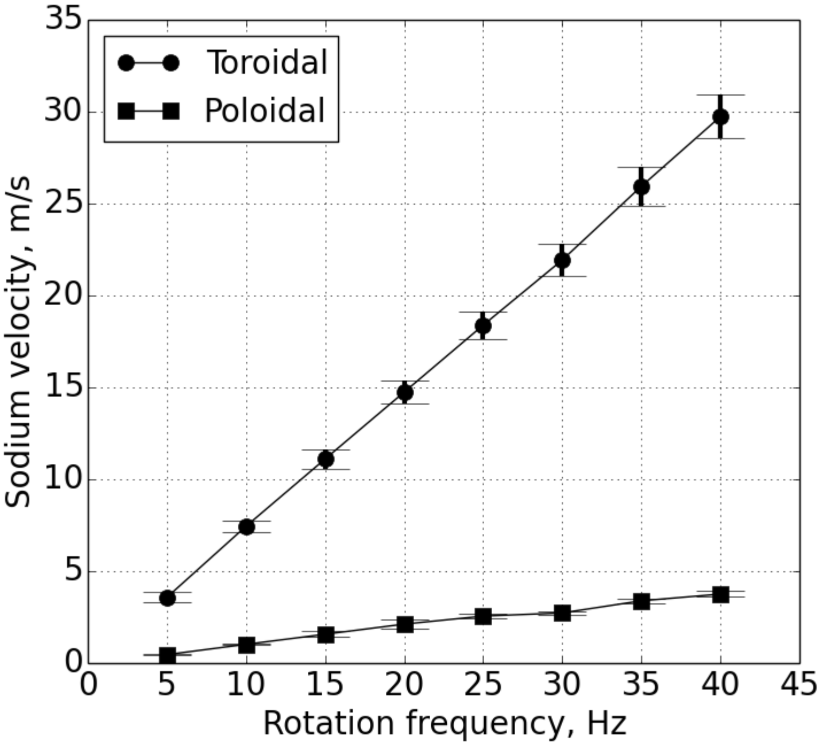

Figure 46: Maxima of V_{tor} and V_{pol} for different rotation frequencies. One observes almost linear growth of velocity depending on the rotation rate.

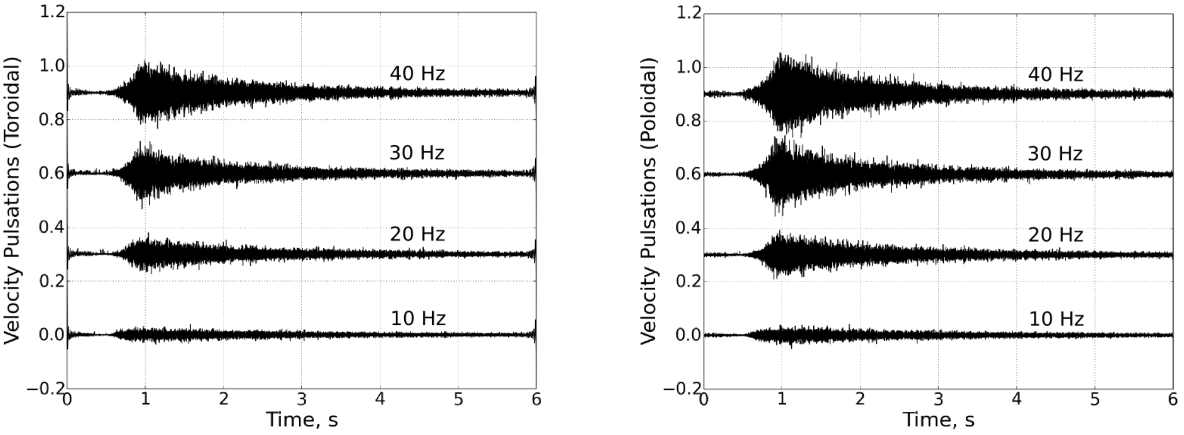

(a) (b)

Figure 47: Pulsations of toroidal (a) and poloidal (b) velocity components at different rotation frequencies f_{rot}. The level of pulsations becomes higher when f_{rot} increases. Although the mean component of V_{tor} is higher (fig.45), pulsations of V_{pol} are stronger.

by an additional Wavelet analysis in Section 4.4.4 where the signals are studied in a time-frequency domain. A more detailed analysis of the flow evolution can be found in [39] and [42].

4.4.2 Induced magnetic field measurements

The value of toroidal and poloidal velocity components (and hence the value of Re_m) depends on the initial rotation rate of the channel. It is convenient to use the following expression which links the rotation frequency f_{rot} in Hz with the magnetic Reynolds number: $Re_m = \alpha f_{rot}$, where $\alpha \approx 0.78\ Hz^{-1}$. Once the desired rotation frequency is reached and the channel is braked, sodium velocity starts to rise. When it reaches maximum, the induced field is the strongest at this moment. The maximum values of b^{tor}/B_0 and b^{pol}/B_0 ratios at different magnetic Reynolds numbers Re_m are shown in fig.49, where $B_0 = 0.1\ T$ is the estimated imposed magnetic field in the fluid near the channel wall. The way of how the data shown in fig.49 is organized needs a detailed explanation. The considered flow has two velocity components: toroidal V_{tor} and poloidal V_{pol}. The rotation frequency of the channel f_{rot} varies in the range from 5 to 40 Hz. Each frequency corresponds to a certain maximum value of V_{tor} and V_{pol}. Since V_{tor} and V_{pol} are the sources for the induced fields b^{tor} and b^{pol}, it is reasonable to plot $b^{tor} = f(V_{tor})$ and $b^{pol} = f(V_{pol})$ on the same figure. In order to use non-dimensional velocities, from V_{tor} and V_{pol} we constructed $Re_m^{tor} = LV_{tor}/\lambda$ and $Re_m^{pol} = LV_{pol}/\lambda$, where λ is the magnetic diffusivity. For convenience $Re_m^{pol} = [0.5 .. 4]$ and $Re_m^{tor} = [3.7 .. 30]$ were combined into $Re_m = [0.5 .. 30]$ to have a simplified form of the x-axis. Remarkably, the ratio $b/B_0 = f(Re_m)$ deviates from the linear law at $Re_m \sim 4$. This is the evidence of a non-linear field expulsion that has been also observed in [43]. However here this effect is much more pronounced. The induced field stops growing linearly because at $Re_m > 1$ the imposed field B_0 is expelled and as a consequence, eddy currents become weaker that diminishes the induced field b. The time-evolution of $b^{tor}(t)$ and $b^{pol}(t)$ is strongly affected by a non-linear temperature drift and therefore is not shown here.

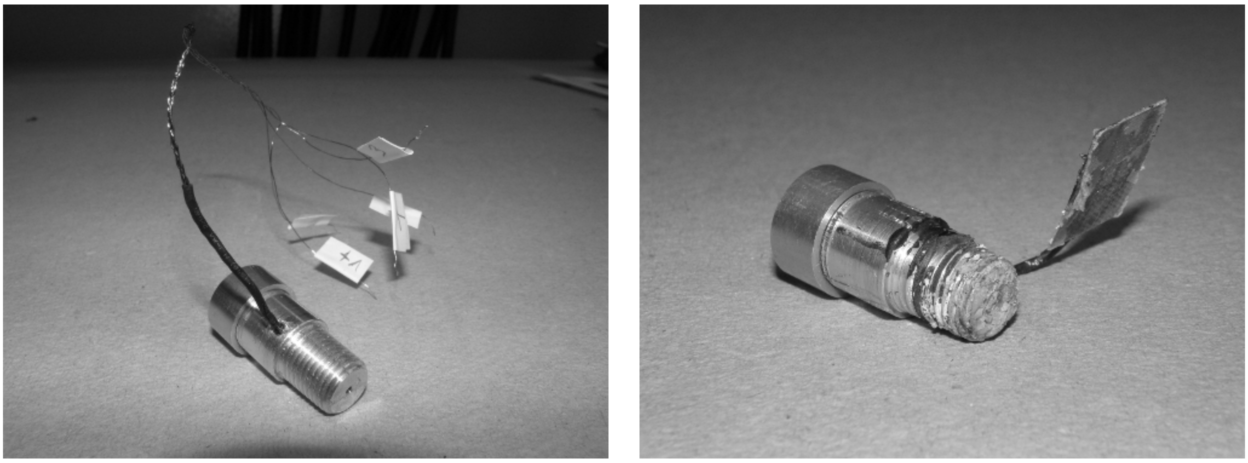
(a) (b)

Figure 48: Measurement probe for the induced magnetic field: before (a) and after (b) tests. Since the probe had a direct access to liquid sodium, an oxidation process slightly damaged the aluminium shell.

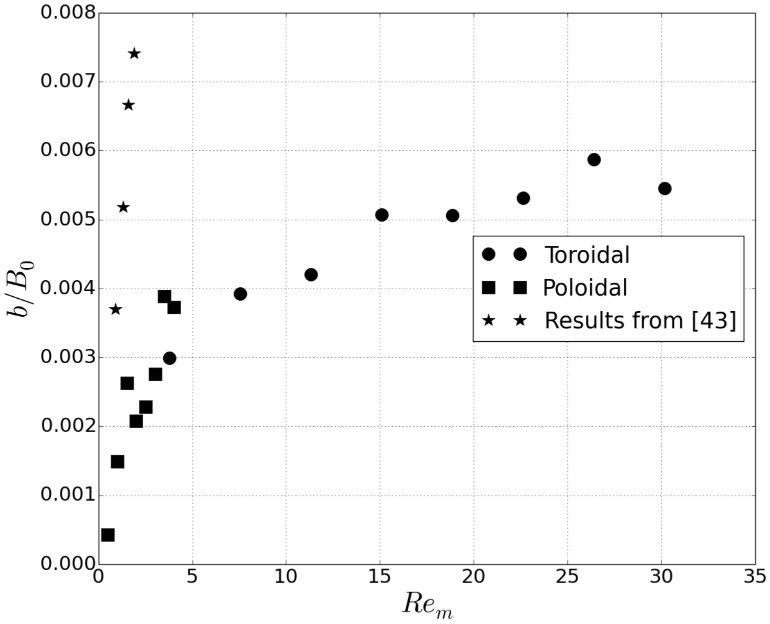

Figure 49: Induced to imposed magnetic field ratio as a function of magnetic Reynolds number. At $Re_m \gg 1$ the imposed field B_0 is expelled that prevents the linear growth of b.

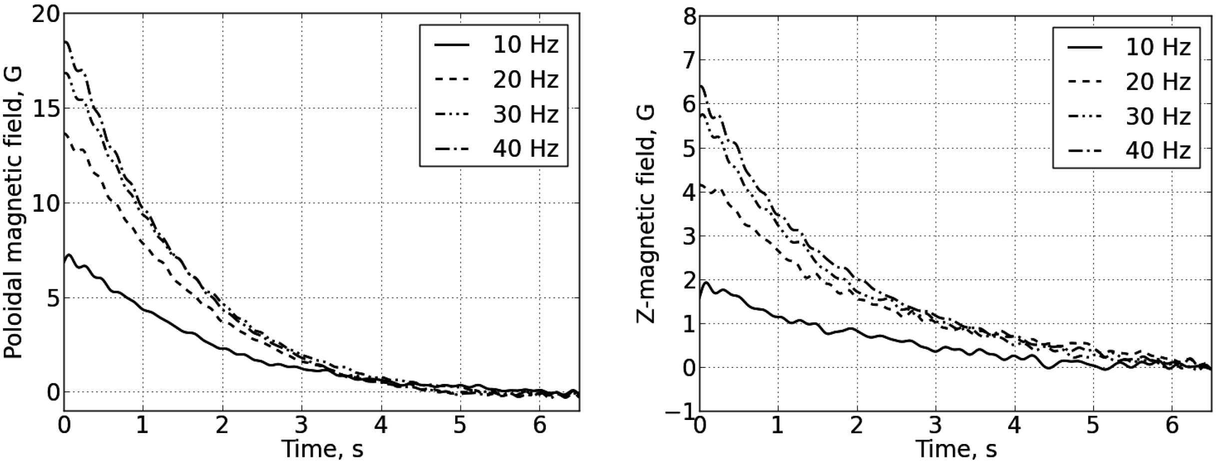

(a) (b)

Figure 50: Evolution of poloidal component (a) and z-component (b) of the induced magnetic field at several rotation frequencies. Z-component has the opposite direction to the magnetization vector of the cubic magnet. Time $t = 0$ corresponds to the end of the braking phase.

4.4.3 Lorentz force measurements

In Section 4.4.2 the long-term measurements of the induced magnetic field were not possible because the signal is affected by temperature variations. In case of the static measurement probe the situation is better since the probe has no direct contact with the liquid metal. Although the main goal of this experiment is to measure the force, to take an advantage of a remote probe position the poloidal $b^{pol}(t)$ and the z-component $b^z(t)$ of the induced magnetic field are also measured (fig.50). Here the z-direction is a direction which is opposite to a magnetization vector of the cubic magnet (fig.39b). At $t = 0$ the channel stops rotating, the flow has the highest velocity and therefore the magnetic field also reaches its maximum value. Then $b(t)$ decays as the velocity tends to zero. As expected, the maximum values of $b(t)$ at $t = 0$ do not increase linearly with the rotation frequency because of non-linear expulsion phenomenon discussed in Section 3.3.3. The expulsion also affects the Lorentz force at high velocities. In this case the induced fields are strong enough to make the imposed field partially frozen in a conductor so that it “runs away” with the flow. It leads to the fact that the linear relationship between force and velocity is not valid (fig.51a). As a consequence, the calibration factor k from (74) becomes a function of Re_m (fig.51b) that complicates a device calibration. Unfortunately, it is not possible to obtain flow at $Re_m \ll 1$ on this setup because at rotation frequencies $f_{rot} < f_{min} = 5Hz$ the flow is very unstable and the data are not reproducible. Therefore we have no data points on fig.51b to show that at $Re_m \to 0$ the factor k tends to some constant velocity-independent value because it depends also on the distribution of magnetic field. However it can be readily seen from any previously published article about LFV-methods (e.g. [13, 34, 35]). Another interesting question is what happens with the Lorentz force at the opposite limiting case when $Re_m \to \infty$? In a flow with extremely high Re_m the field expulsion must be so strong that eddy currents density $j \to 0$ in

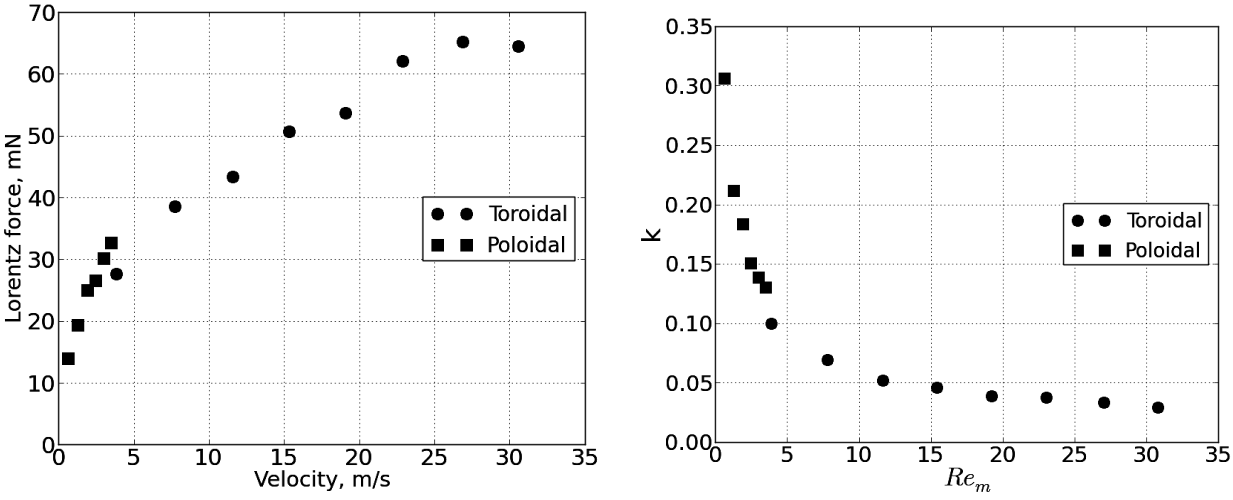

(a) (b)

Figure 51: (a) Lorentz force measurements at different sodium velocities. At the low flow rate the force depends linearly on velocity according to (74) [13,34,35]. At high velocities a deviation from linearity is observed. (b) The calibration constant k in this case becomes a function of magnetic Reynolds number Re_m.

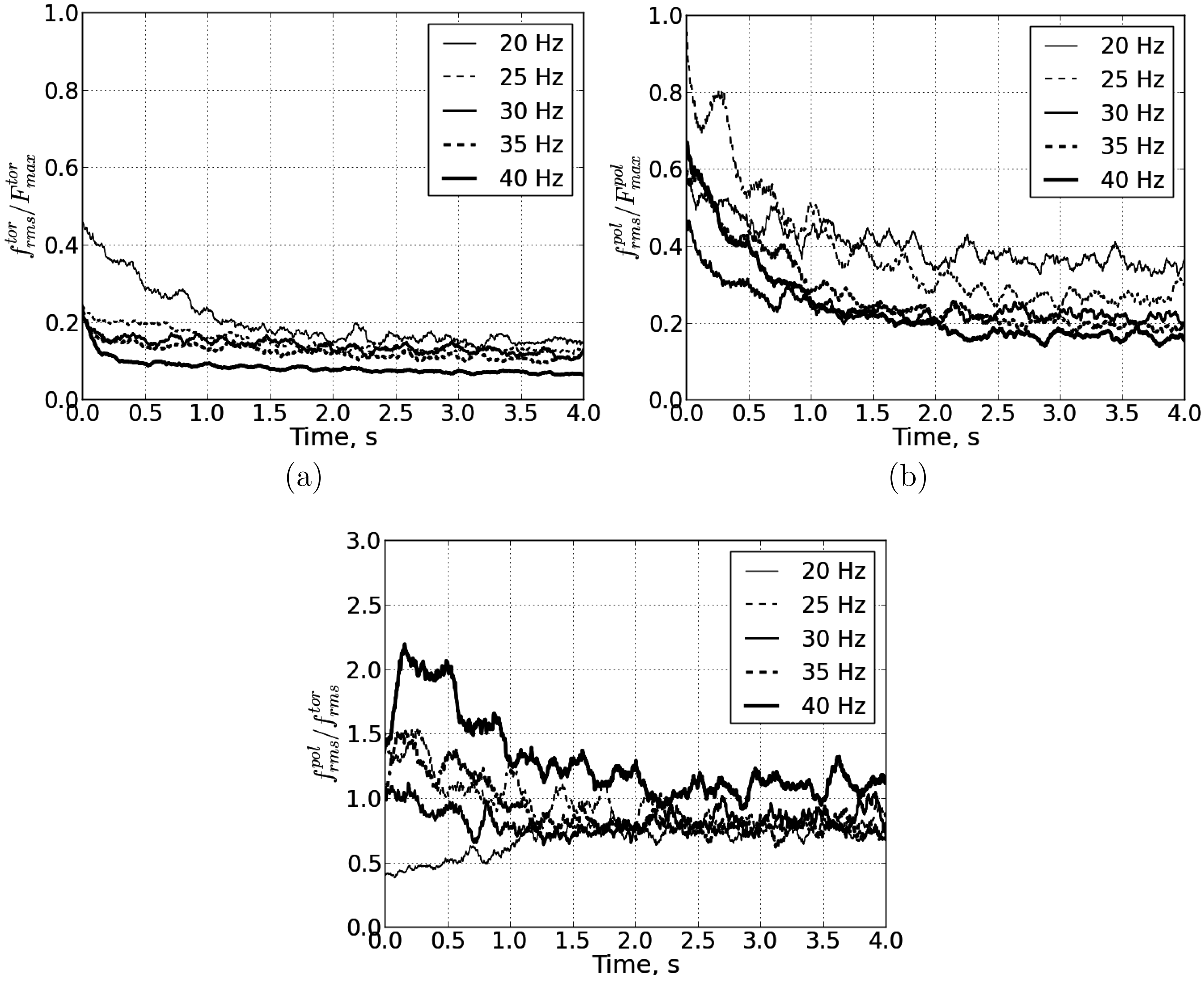

(a)

(b)

(c)

Figure 52: Fluctuation characteristics of toroidal and poloidal Lorentz force components: (a) ratio of rms of toroidal fluctuations to the maximum toroidal force; (b) the same ratio for the pololoidal component; (c) ratio of poloidal to toroidal fluctuations (RMS). Time $t = 0$ approximately corresponds to the end of the braking phase.

the medium. Consequently, the Lorentz force also has to go down to zero. However, at $Re_m > 50$ the effect of magnetic *dynamo* becomes important [44]. It means that the field expulsion superimposes upon the self-generation of the induced magnetic field. The combination of these two phenomena results in a very complex magnetic field distribution. Indeed, this problem is of great fundamental importance but is beyond the scope of this paper.

A good sensitivity of the piezoelectric sensor allows measuring root-mean-square (RMS) of the force fluctuations. It is important to choose a proper moving time-window for the RMS-calculation because the signals are non-stationary. Taking into account that the frequency of turbulent fluctuations F_{fluct} in the considered flow can reach $10kHz$ [30] and by choosing the time-window of $T = 0.1\ s$, the relative error of RMS-calculation $\epsilon = 1/\sqrt{F_{fluct}T} \sim 3\%$ [45] which is low enough to show a general tendency. Usually, RMS of a signal is non-dimensionalized by the mean value of that signal so that a relative level of fluctuations becomes clear. Since the low-frequency component of the force suffers from the charge leakage we can not do so in our case. Instead of that we refer RMS values to the force maxima (fig.51a) reached at the end of the braking phase that corresponds to $t = 0$. When the braking phase is over the force oscillations are strong and then they gradually decay as $t \to \infty$ (fig.52a and fig.52b). Remarkably that although the poloidal force is weaker than the toroidal one, the relative poloidal fluctuations are stronger. It is explained by the same tendency observed in velocity measurements [30]. The ratio of f^{pol}_{RMS} to f^{tor}_{RMS} shows that, basically, fluctuations of both components are either equal at $t > 1$ s (fig.52c) for all rotation frequencies or equally damped by the skin-effect. The last assumption has to be proved in the future.

4.4.4 Wavelet analysis

4.4.4.1 Why wavelets? The widely-used Fourier Transform (FT) is a powerful tool to analyze signals in a frequency domain [46]. However it does not work well if the frequencies vary in time. For example, in case of a chirp signal (fig.53) a frequency spectrum obtained by the standard FT does not show any dominant frequency at all since the latter is continuously changing. Neither can it distinguish whether several different frequencies simultaneously present in the signal or their show up at a certain moment. To solve this problem one has to consider a time-frequency domain where the evolution of all frequency components can be analyzed. One way to do it is to use the Short Time Fourier Transform (STFT) which is the normal FT of the signal multiplied by a window function, e.g. a simple rectangular window. Thereby only a short segment of the signal is analyzed. On the face of it, this method should always work if we properly choose a length of the time-window. The problem is that it is impossible to do in a general way! To understand it, let us consider again the chirp signal. If the time-window is short, the high-frequency part of the signal is well resolved whereas the low-frequency segment suffers poor resolution. In case of the long time-window everything is other way round. The conclusion is that a fixed length of the time-window puts a serious constraint on time-frequency analysis. An intuitive solution is to make this length time-dependent so that the window-function evolves in time with the signal. This idea brings us to the Continuous Wavelet Transform (CWT) which offers very good time and frequency localization at the same time [47, 48].

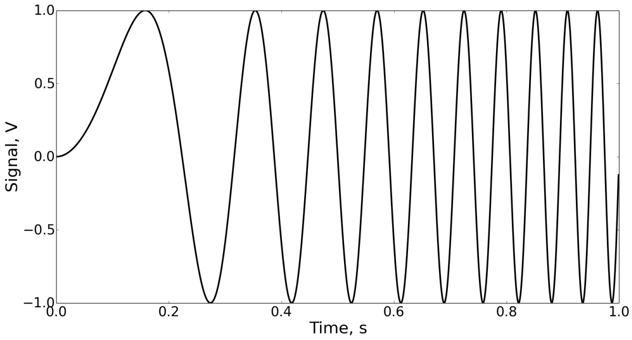

Figure 53: Chirp signal is a simple example of a signal whose spectrum can not be resolved well using Fourier Transform or Short Time Fourier Transform.

4.4.4.2 Continuous Wavelet Transform Continuous Wavelet Transform is defined as [49]:

$$W_\psi f(b,a) = \int_{-\infty}^{\infty} f(t)\overline{\psi_{b,a}(t)}dt, \tag{79}$$

where $\psi_{b,a}$ is a family of wavelet functions, overline denotes complex conjugate, b and a are translation and dilation (or scale) parameters. Wavelet Transform is a procedure of a signal decomposition into basis functions (wavelets), which are constantly being modified while jumping from scale to scale. Strictly speaking, CWT provides rather the time-scale analysis and not exactly the time-frequency analysis. However, $1/a$ can be considered as a measure of frequency and translation parameter b represents the position of the wavelet in time. Among a great variety of wavelet functions the complex *Morlet* (or *Gabor*) wavelet [50] was chosen (80):

$$\psi(t) = \frac{1}{\pi^{1/4}}(e^{i2\pi f_0 t} - e^{-(2\pi f_0)^2/2})e^{-t^2/2} \tag{80}$$

Here f_0 is a central frequency of the mother wavelet. This wavelet is widely used in signal processing [51–53] and is known for minimizing the product of its standard deviations in the time and frequency domain [54]. The real and the imaginary parts of the Morlet wavelet at $f_0 = 4/2\pi$ are shown in fig.54.

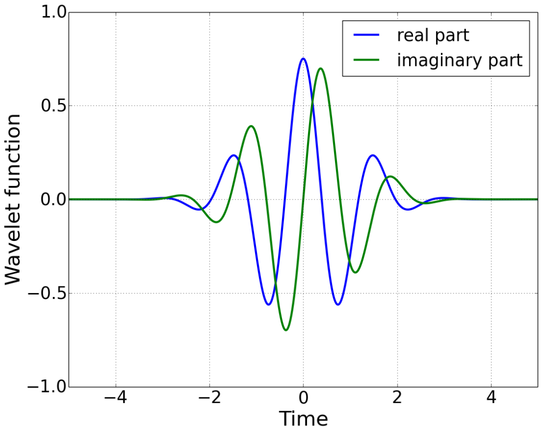

Figure 54: Real and imaginary parts of the Morlet wavelet (80) at $f_0 = 0.64$.

To calculate CWT coefficients a Python-based mathematical library MLPY[1] was used. The corresponding coefficients for velocity and force signals are shown in fig.55.

---

[1] http://mlpy.sourceforge.net/

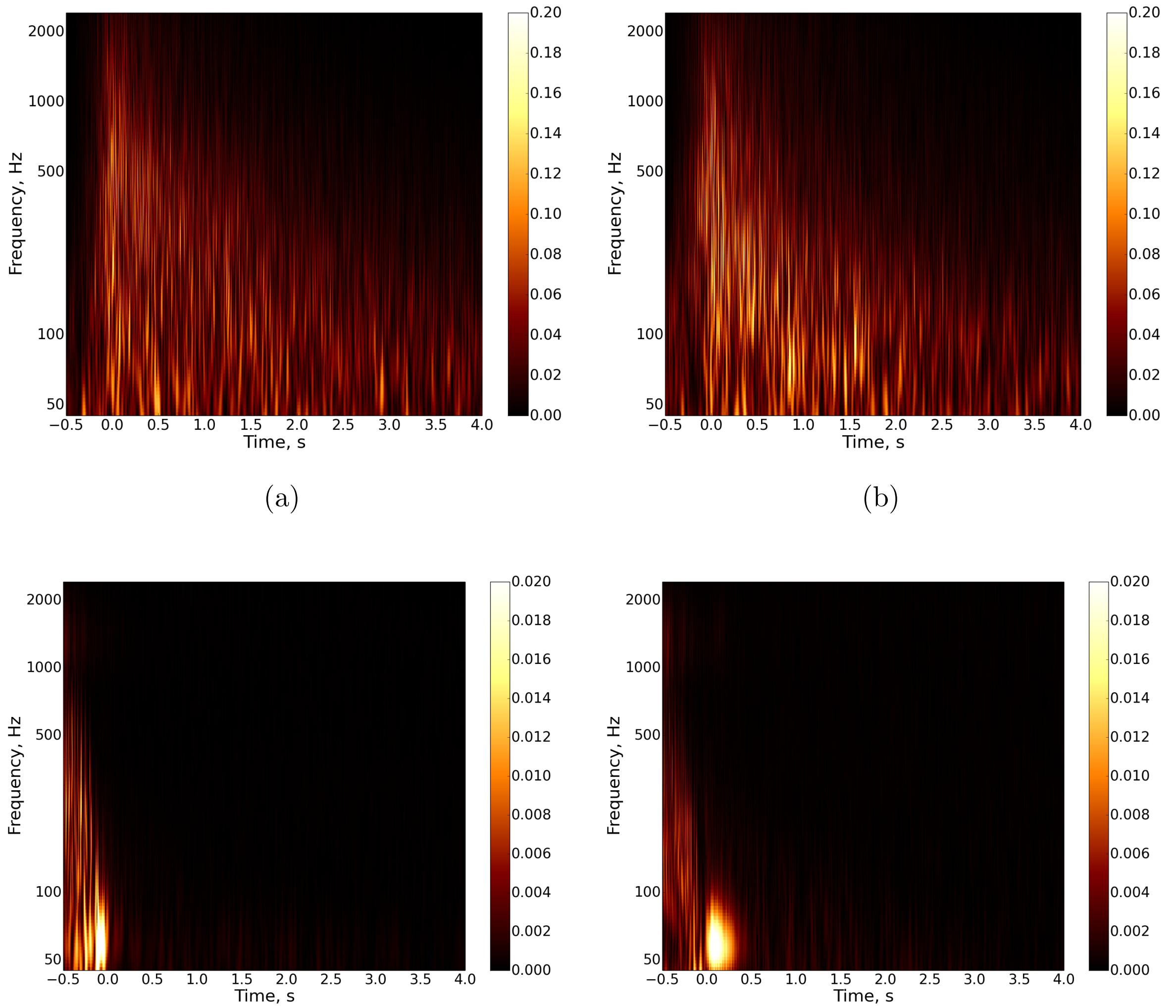

(a)

(b)

(c)

(d)

Figure 55: Continuous Wavelet Transform of V_{tor} (a), V_{pol} (b), F_{tor} (c) and F_{pol} (d) at $f_{rot} = 40\ Hz$. Time $t = 0$ corresponds to the end of the channel braking. The analyzing wavelet function is the Morlet wavelet with central frequency $f_0 = 0.64$. Although the amplitude of toroidal velocity is higher, the pulsations of the poloidal component is stronger. The same stands for the force signal. However, the values of wavelet coefficients in the second case are approximately 10 times smaller. This difference is caused by the skin-effect in the Lorentz force measurements.

4.4.4.3 Discrete Wavelet Transform If we set $a = 1/2^s$ and $b = k/2^s$ for s and k $\in \mathbb{Z}$ in (79), then a generated sparse set of values on the time-scale plane will form Discrete Wavelet Transform (DWT) [49]. The main point here is that CWT is a highly redundant transform because it contains an excessive amount of data to make a perfect reconstruction of a signal from its wavelet transform. To get rid of this redundancy one can define CWT on a discrete set of points. Indeed a part of the information is lost but by choosing proper a and b one can perfectly restore the initial signal. Also a good thing is that a fast algorithm exists [48] and the method can be applied to large data arrays. The main reason of recalling DWT here is in the possibility to define DWT-based cross-correlation function (CCF). The standard way of calculation CCF is computationally demanding [55]. Even the usage of FFT-based convolution will not bring a lot because this method inherits all of the disadvantages of FFT analysis described in Section 4.4.4.1. A promising way to resolve this issue is to use the DWT-based convolution algorithm. The last obstacle here is the lack of time-invariance. It means that DWT of a translated version of a signal differs from the translated version of the DWT of this signal. To overcome this drawback the Undecimated Wavelet Transform (UWT) has to be used. There are several mathematical libraries available which can compute UWT of a given signal. However in order to understand deeply how this algorithm works a new in-house code was written and validated (Appendix B).

4.4.4.4 Undecimated Wavelet Transform First of all, in order to make use of UWT one has to choose a wavelet function. We use here the orthogonal 4-tap Daubechies wavelet [47]. It can not be written down in an analytical form and to construct it one has to use so-called two-scale relations [49]:

$$\phi(t) = \sum_k g_0[k]\phi(2t-k) \tag{81}$$

$$\psi(t) = \sum_k g_1[k]\phi(2t-k), \tag{82}$$

where ϕ is a scaling function and ψ is a wavelet function. Equation (81) defines the scaling function recursively. From [49] the corresponding filter coefficients $g_0 = [0.68, 1.18, 0.32, -0.18]$. The most simple way to get ψ is to use the iteration method, i.e.:

$$\phi_{m+1}(t) = \sum g_0[k]\phi_m(2t-k) \tag{83}$$

Having initialized the process by setting $\phi_0(t) = \delta(t)$, the procedure converges after approximately 10 iterations. Once the scaling function is obtained, one can calculate the wavelet function according to (82) with filter coefficients $g_1[k] = (-1)^k g_0[1-k]$. The result is shown in fig.56.

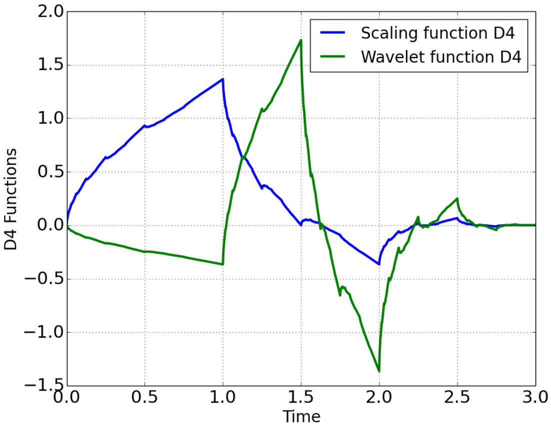

Figure 56: 4-tap Daubechies scaling and wavelet functions ($\phi(t)$ and $\psi(t)$ correspondingly). The function ϕ is calculated by the iteration method and the function ψ is obtained by the two-scale relations.

Although the wavelet function $\psi(t)$ has been obtained, one cannot use the method straightforwardly because it is still a time-consuming process to use (79) even on a sparse set of points. Fortunately, the fast algorithm has been developed which is based on the *multiresolution analysis* [48]. In short, the wavelet coefficients are obtained by passing a signal through a low-pass and a high-pass filters with coefficients h_0 and h_1 correspondingly. It produces two signals out of one. In DWT the output of the low-pass filter is downsampled by 2 and then is subjected the same operation recursively. In UWT the output is not changed but the filter coefficients $h_0[k] = g_0[-k]/2$ and $h_1[k] = (-1)^k g_0[1+k]/2$ are upsampled by 2 at each next step (fig.57). Thereby the time-invariance is achieved. The price that we have to pay is the redundant nature of the algorithm. However, the extent of redundancy here is much less than in case of CWT.

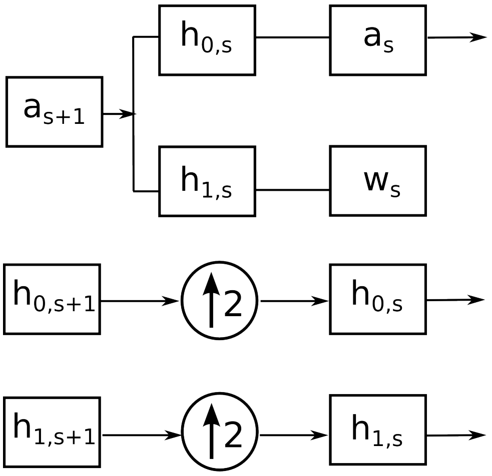

Figure 57: Undecimated Wavelet decomposition algorithm. To obtain the wavelet coefficients w_s a signal a_{s+1} is passed through a low-pass and high-pass filters whose coefficients h_0 and h_1 are upsampled at each next step. In contrast to DWT algorithm, UWT is a time-invariant transform.

The UWT-based cross-correlation function is defined as [56]:

$$W_U C_{f,g}(a,\tau) = \int_0^T \overline{W_U f(b,a)} \cdot W_U g(b+\tau,a) db, \tag{84}$$

where $W_U f(b,a)$ and $W_U g(b,a)$ are Wavelet coefficients of two signals. Then a normalized cross-correlation coefficient can be written as:

$$W_U R_{f,g}(a,\tau) = \frac{W_U C_{f,g}(a,\tau)}{\sqrt{W_U C_f(a,0) \cdot W_U C_g(a,0)}}, \tag{85}$$

where $-1 < W_U R_{f,g} < 1$. Fig.59 shows an example of UWT-based cross-correlation analysis. Likewise one can define the auto-correlation coefficient:

$$AW_U R_f(\alpha,\tau) = \frac{W_U C_{f,f}(\alpha,\tau)}{|W_U C_f(\alpha,0)|} \tag{86}$$

The auto-correlation coefficient reveals the appearance patterns of different frequencies. If $AW_U R_f(\alpha,\tau)$ has a maximum at a certain point (α_0,τ_0) on a (α,τ)-plane it means that a frequency which corresponds to the scale α_0 shows up each τ_0 seconds.

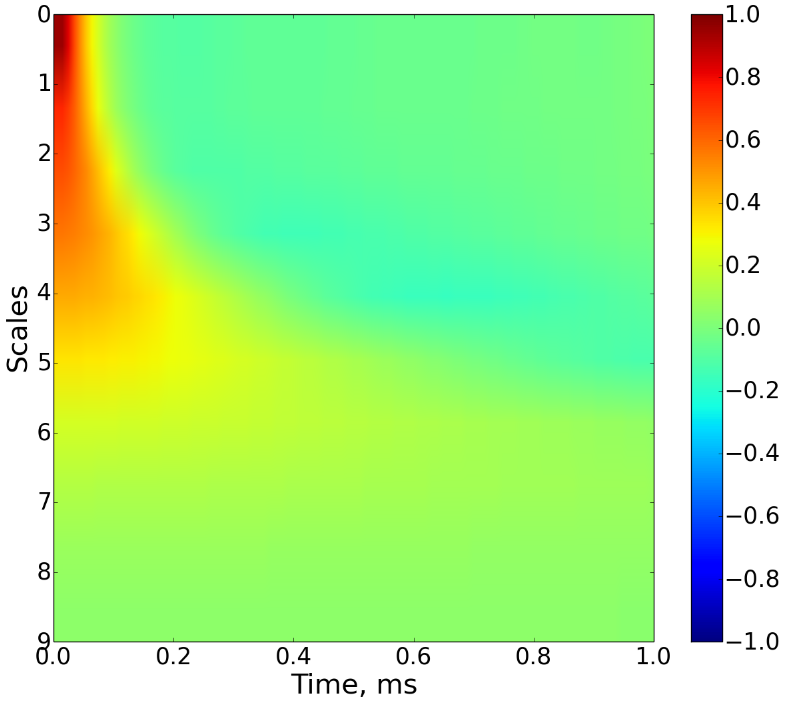

Figure 58: Auto-correlation coefficients of $V_{tor}^{puls}(t)$ at $f_{rot} = 40\ Hz$ for different scales.

Likewise one can calculate auto-correlation coefficients for velocity signals obtained in the experiment that was discussed in Chapter 4. Of course, first of all a mean component has to be subtracted from the original signal to have pulsations only. Fig.58 shows auto-correlation coefficients for V_{tor}^{puls} at each scale.

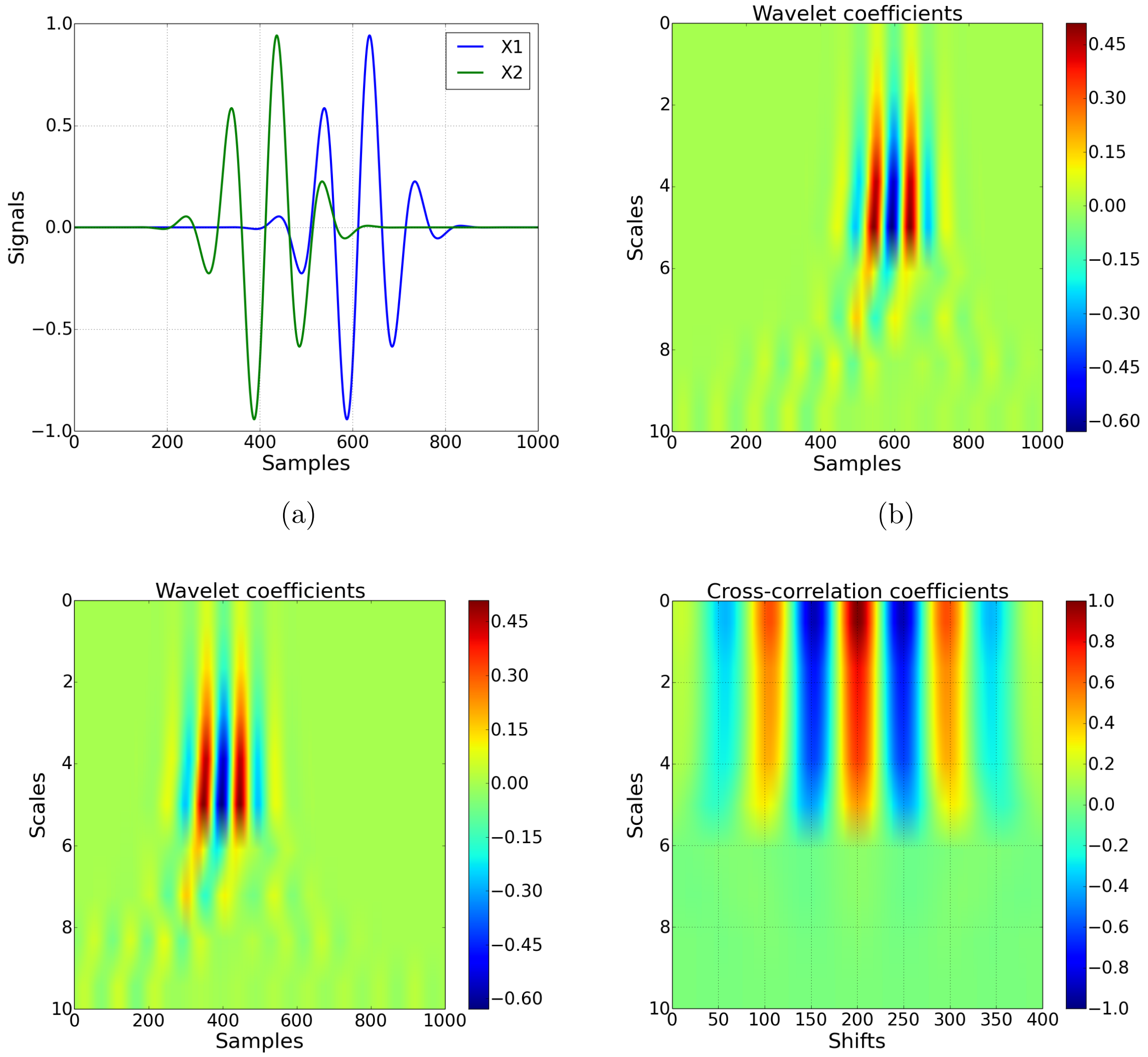

(a) (b)

(c) (d)

Figure 59: Example of a cross-correlation analysis based on Undecimated Wavelet Transform. We apply UWT to two test signals (a) obtaining UWT coefficients $W_U X1(b,a)$ for signal X1 (b) and $W_U X2(b,a)$ for X2 (c) by the algorithm described in Section 4.4.4.4. After that the cross-correlation coefficient $W_U R_{X1,X2}$ is calculated using (85) (d). Local maxima of $W_U R_{X1,X2}$ point to the time lag between frequencies appearance in signals X1 and X2 at each scale.

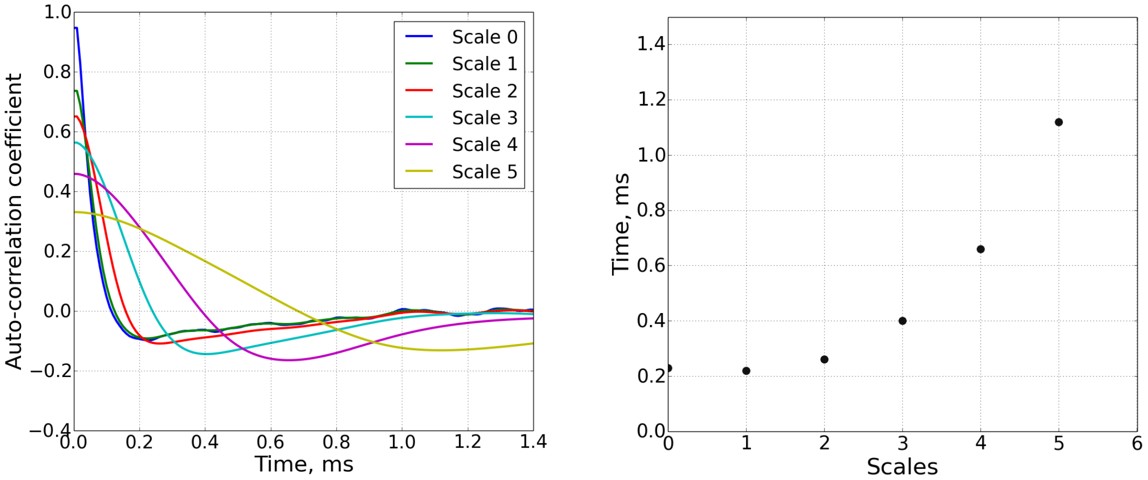

a) b)

Figure 60: Auto-correlation coefficients for V_{tor}^{puls}. Pulsations with lower frequencies appear in the signal less often than pulsations with high frequencies (smaller scales correspond to higher frequencies).

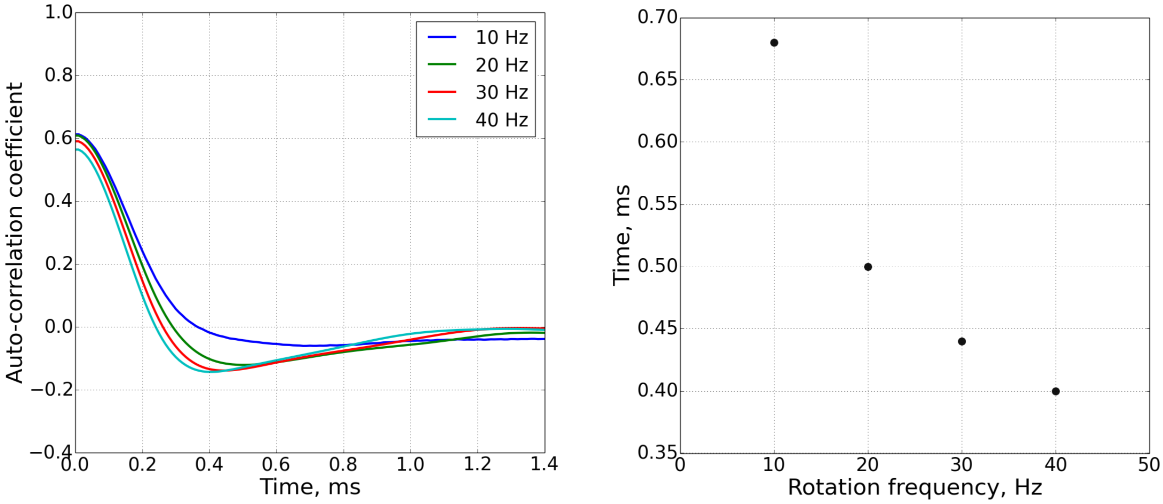

a) b)

Figure 61: Auto-correlation coefficients of V_{tor}^{puls} at scale=4 for different rotation frequencies. The minimum of the curves is shifted towards smaller time lag as the rotation frequency becomes higher. It means that the higher f_{rot}, the more often the pulsation frequencies at scale=4 appear in the signal. The same tendency is observed for all scales.

For a better analysis, it is convenient to split fig.58 into scales (fig.60a) and to calculate minima of each single curve. These values correspond to a characteristic time of appearance of a corresponding frequency in the signal (fig.60b). From these plots one can conclude that high-frequency pulsation bursts in velocity signal appear more often than low-frequency pulsations. Fig.61 shows that pulsations at scale=4 appear more often if the rotation frequency increases. This is true for all scales.

4.5 Error analysis

4.5.1 Velocity measurements

4.5.1.1 Random errors Relative random error in velocity measurements is estimated as:

$$\eta(\bar{X}) = \frac{\delta(\bar{X})}{\bar{X}}, \tag{87}$$

where $\delta(\bar{X})$ is taken from (65). As it has been already mentioned, the flow at $f_{rot} \leq 5\ Hz$ is unstable and the data suffer from poor reproducibility. However the highest error corresponds to $f_{rot} \approx 15 - 20\ Hz$ which is a resonant frequency range for the setup. For $f_{rot} > 30\ Hz$ the relative error $\eta(\bar{X})$ does not exceed 1%. Overall the maximum error is less than 13 %.

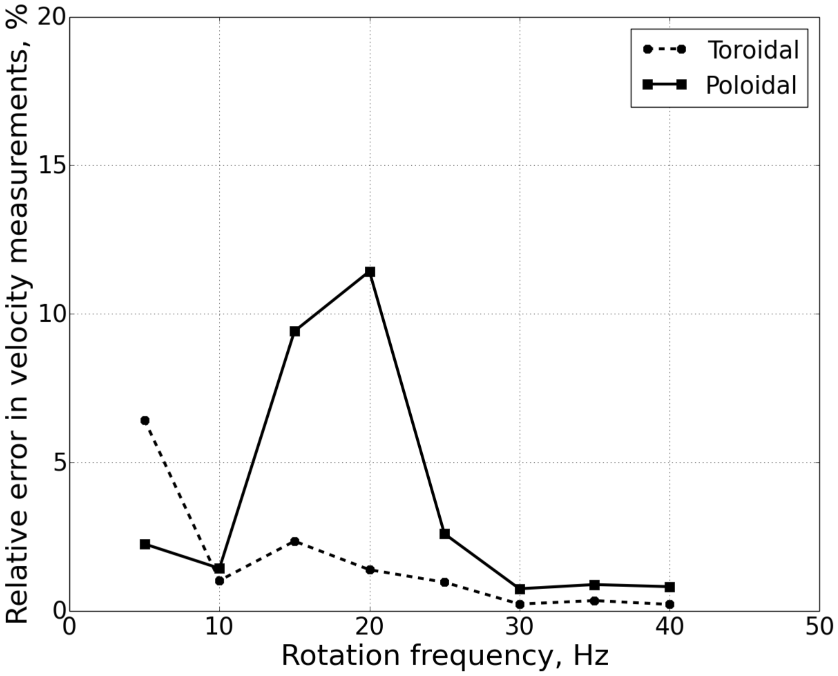

Figure 62: Relative error $\eta(\bar{X}) = \delta(\bar{X})/\bar{X}$, where $\delta(\bar{X})$ is calculated according to (65).

4.5.1.2 Statistical errors Statistical errors in velocity measurements primarily come from non-linearity of the Vives probe output at high sodium velocity. Remarkably but this is again a manifestation of high Re_m effects because the imposed field of the Vives probe becomes distorted by the flow. In [39] the authors estimated the error caused by a deviation of a potential difference from the linear law (fig.63a). Another issue is an assumption about typical time of the flow decay. Since it is unclear what exactly happens in the flow during the braking phase, the initial offset is subtracted such that $V_{tor}(t_0) = 0$, where $t_0 = 10\ s$. Here we imply that $\partial V_{tor}(t_0)/\partial t \approx 0$. The results show that the velocity

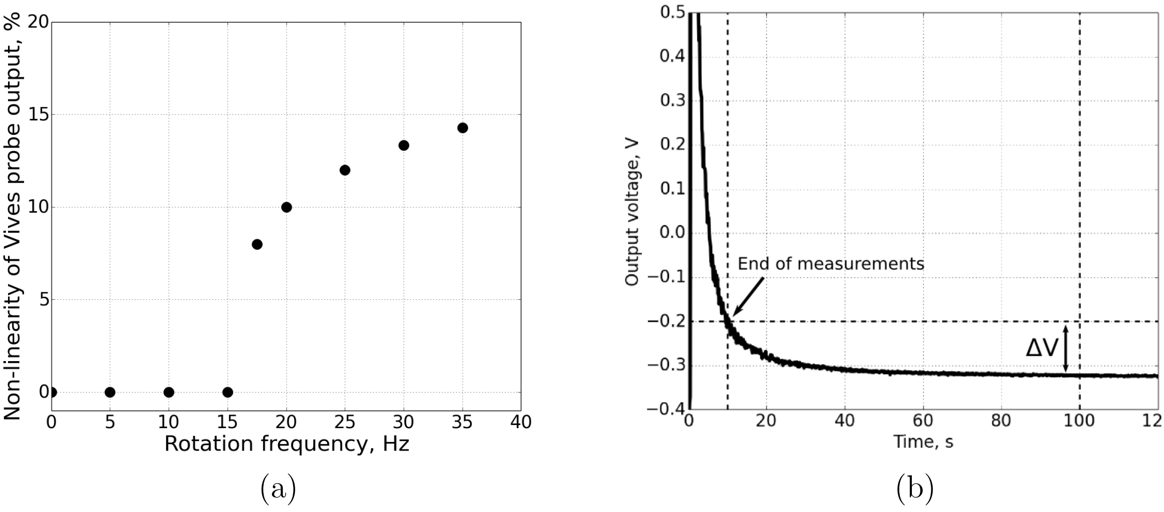

(a) (b)

Figure 63: Statistical errors in velocity measurements. (a) Error in potential difference measurements (calculated from [39]). Below 15 Hz the output of the Vives probe is linear. At $f_{rot} > 17\ Hz$ (i.e. $Re_m > 13$) the signal suffers from non-linearity. The relative error does not exceed 15% in this case. (b) Raw output voltage from the Vives probe corresponding to the toroidal velocity at $f_{rot} = 45\ Hz$. The long run shows that by implying $V_{tor}(t = 10\ s) = 0$ one has the statistical error $\eta(V_{tor}) = \Delta V/V_{max} \approx 4\%$.

decays approximately as t^{-1} and $\partial V_{tor}(t)/\partial t \approx 0\ m/s^2$ at $t \geq 3t_0$ (fig.63b). It gives the relative error about 4 %.

4.5.2 Lorentz force measurements

4.5.2.1 Random errors Fig.64 shows a random error in Lorentz force measurement. Again, at $f_{rot} = 5\ Hz$ $\eta(\bar{X})$ reaches 6-9 % that is caused by a transient character of the flow evolution. At $f_{rot} \approx 20 - 25\ Hz$ an influence of the resonance is observed. This error is less than the error of velocity measurements at the same frequency range. The reason is that axial oscillations of the channel result in high-frequency variations of the Lorentz force. But due to the skin-effect these variations are damped and the measurement system becomes partially immune to such impacts. Measuremets of poloidal component is again worse than the measurements of toroidal one. However one cannot straightforwardly attribute this fact to the less stable poloidal velocity because Lorentz force components were measured in two separate experiments (Section 4.2.4). It is possible that mechanical properties (e.g. eigen frequencies) of the whole measurement system have been changed when the force sensor is turned by 90^o. That can be the reason for a different Lorentz force response.

4.5.2.2 Statistical errors Because of the measurement system complexity it is very difficult to quantify a statistical error. Here possible sources are listed:

1. When the Lorentz force is applied to the magnet and the sensor, a displacement of the aluminium cantilever takes place. Although this impact must be tiny, a finite torsional stiffness of the stand may influence the results.

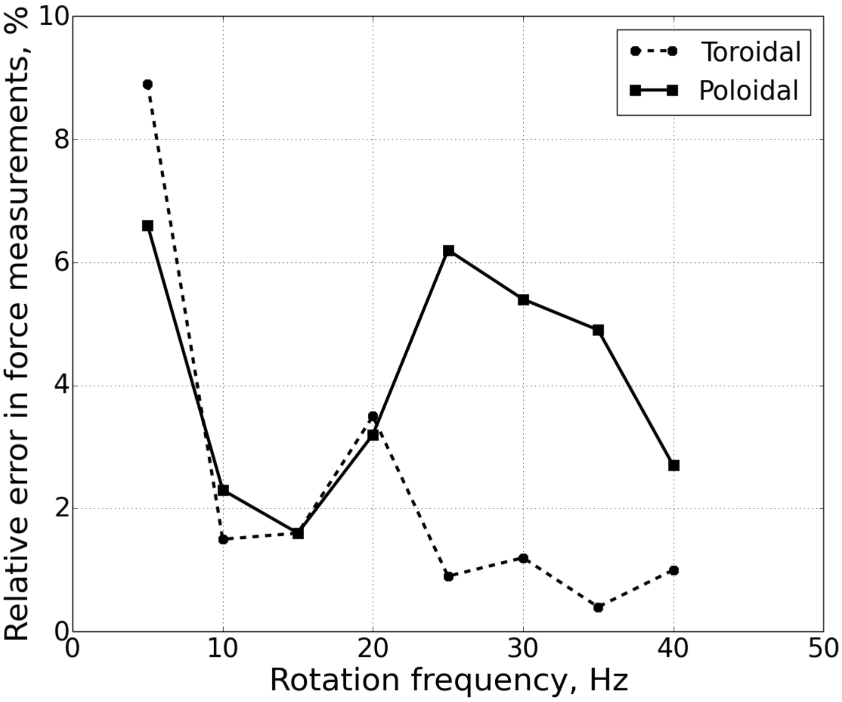

Figure 64: Lorentz force measurement error. Excluding a region of unstable flow at $f_{rot} = 5\ Hz$ the error does not exceed 6-7 %.

2. The charge leakage of the piezoelectric force sensor (discussed in Section 3.2.1) diminishes an output voltage. To compensate it the measured Lorentz force was multiplied by a factor of 1.05 which is calculated from the modeling equation (55). Therefore the error can come from the discrepancy between the model and a real sensor performance.

3. A direction of the magnetization vector of NeFeB magnet might not be aligned exactly orthogonally to the velocity vector. As a consequence, the toroidal force can contribute to the poloidal one.

4.5.3 Induced magnetic field measurements

4.5.3.1 Random errors A random error was estimated likewise it has been done in Sections 4.5.1 and 4.5.2. Fig.65 proves that at high rotation rate the random error is less than 5%. On the contrary, at low rotation frequencies the flow instability increases data scattering, especially in case of the poloidal component.

4.5.3.2 Statistical errors Since the braking time is less than 0.5 s, the signal is not affected by temperature variations. The only error source is the sensor's non-linearity. According to specifications the error does not exceed 2%.

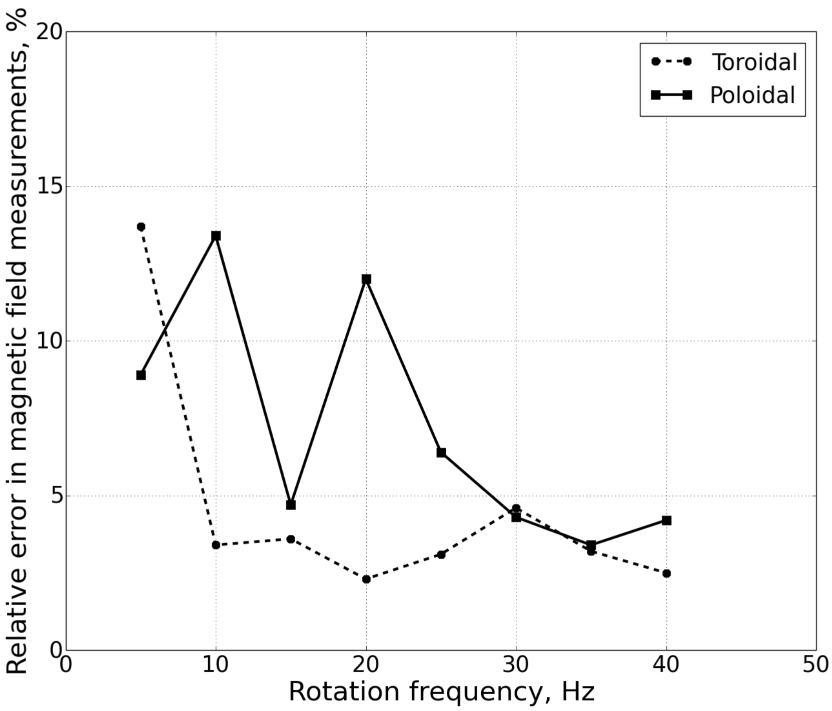

Figure 65: Random error of induced magnetic field measurements. The poloidal component is less stable than the toroidal one. As a consequence, the random error is higher in the first case. At $f_{rot} > 30\ Hz$ the error does not exceed 5%.

4.6 Conclusions

The high-speed nonstationary sodium flow in the toroidal titanium channel is considered. The toroidal and poloidal components of the induced magnetic field were measured at magnetic Reynolds numbers in the range from 0.5 to 30. At $Re_m > 4$ a non-linear growth of the ratio $b/B_0 = f(Re_m)$ is clearly observed. It is the evidence for magnetic field expulsion. The imposed field becomes weaker in the medium and, consequently, the eddy currents go down that leads to a smaller value of the induced magnetic field. Independently, the Lorentz force at the same Re_m range was successfully measured. It was experimentally proved that the linear law (74) is not valid for the high Re_m flow. It was important to figure out that a clear deviation from the linear law starts also at $Re_m \approx 4$. These data are in a good agreement with the induced field measurements. The results lead to the fact that the calibration factor k depends on the conductor velocity. Consequently, a more sophisticated calibration procedure for a customer-oriented device is necessary in this range.

5 Conclusions and Outlook

This work was entirely devoted to the problem of the Lorentz force velocimetry at finite magnetic Reynolds number. First of all, the theoretical approach has been presented. The goal was to obtain an analytical solution for the Lorentz force generated in a conducting solid body at different conductor velocities. Due to the complexity of governing equations we made a number of simplifications. In the beginning, we considered the simplest case when the velocity changes stepwisely. The obtained solution shows a remarkable delay between force and velocity signals characterized by a typical non-dimensional rising time T_{98}. Then we analyzed a smoothly changing velocity input in order to mimic a real body acceleration. Finally, we studied the case of oscillating velocity which forms an MHD analog of the *Second Stokes Problem*. The theoretical study is closed by the chapter devoted to velocity inputs that can not be analytically integrated, e.g. in form of the *error function*. A numerical scheme was used to calculate the generated Lorentz force F_L and the Joule heat Q in a conducting moving body. We proved that the developed theoretical approach allow obtaining $F_L(t)$ and $Q(t)$ for any given velocity $V(t)$ including the case when the latter is experimentally measured. A comparison with the experimental data shows an excellent agreement in time response and significant discrepancy in amplitude. This discrepancy is caused by neglecting a complex three-dimensional distribution of eddy currents since the model was quasi two-dimensional. A possible continuation of the theoretical approach is to consider a truly two-dimensional model when all parameters change in both directions normal to the main velocity vector. Also it would be helpful to find appropriate boundary conditions for the induced magnetic field in case of a cylindrical conductor.

Because of the above mentioned theoretical restriction it was essential to conduct an experiment. By the fast piezoelectric force sensor the Lorentz force generated in the conducting aluminium and copper rods has been measured. The rods were initially immersed in a magnetic field. The finite magnetic Reynolds number Re_m was achieved by accelerating the rods faster than a typical magnetic field diffusion time. In other words, the imposed field had no enough time to diffuse from the medium and the field dynamics was governed to a greater extent by advection. From the observed Lorentz force response one can make an important conclusion for the Lorentz force velocimetry: if a conductor velocity changes faster than a typical magnetic field diffusion time, a force response becomes shorter and has a diminished amplitude. On top of it, these measurements prove that a sudden body acceleration through an imposed magnetic field leads to a generation of the induced field. This field makes the imposed one "frozen" in a conductor so that it is dragged with a moving medium. This phenomenon is directly related to the magnetic field expulsion. In order to improve the results, one has to find the way to obtain high velocity of the solid conductors under laboratory conditions. A solution is to replace translation motion by the rotational one. Perhaps, it is sensible to set up an experiment where a magnet quickly rotates inside a conducting shell. Using a circular array of Hall sensors located between the magnet and the shell one can trace the magnetic field lines evolution depending on the rotation frequency.

The last part of the current research work was the experimental study of the Lorentz force velocimetry at high speed liquid sodium flow. The experiment has been conducted in the framework of a scientific collaboration between TU Ilmenau (Germany) and ICMM

(Russia). The flow was obtained in a toroidal titanium channel that can rotate with a high frequency and can be braked then by a hydraulic system. During the brake the sodium velocity reaches 30 m/s that makes this setup very suitable to study LFV at high magnetic Reynolds number. There were two separate experiments. In the first experiment toroidal and poloidal components of the sodium velocity and the induced magnetic field as a function of Re_m were simultaneously measured. It was shown that after $Re_m \approx 4$ an induced to imposed field ratio experiences a saturation that directly points to the strong field expulsion. In the second experiment two components of the Lorentz force at the same range of Re_m were measured. It was proved for the first time that $F_L(V)$ deviates from the linear law for velocity if the latter reaches significant values. This result is one of most important in the current work. As a next step, a new probe from titanium for the induced magnetic field measurements is going to be manufactured. The advantage of the titanium probe is the diminished influence of the skin-effect on the measurements of turbulent magnetic field pulsations. The difference between conductivities of Al and Ti is $\sigma_{Ti}/\sigma_{Al} \approx 1/30$ and therefore skin depth ratio is $\delta_{Ti}/\delta_{Al} \approx 5.5$. If the field pulsations are not damped one can readily calculate correlation functions between field and velocity signals and make an estimation of turbulent cross-helicity which is an important quantity for dynamo theory [57].

Finally, it is worth stressing the points which must be taken into account while developing a real device for industrial LFV applications at high speed or non-stationary flows. First, one should not expect the linear dependence of the measured force on velocity (fig.51). It means that it is essential to calibrate the device at the whole expected range of velocities covering the case when $Re_m \geq 1$. Second, the diffusion time in any case gives a good estimate of the reliable time response of a measurement system. Although the force signal may reach an asymptotic value faster than the diffusion time (fig.24b), the amplitude of the measured force will suffer from a statistical error caused by the magnetic field advection (fig.23b). All in all, if these two issues are properly addressed the Lorentz force velocimetry can be successfully extended to flows at high magnetic Reynolds numbers.

Nomenclature

Re	Reynolds number
Re_m	Magnetic Reynolds number
N	Interaction parameter
j	Eddy current density $[A\ m^{-2}]$
ϵ	Electrical field density $[V\ m^{-1}]$
m	Mass $[kg]$
V	Conductor velocity $[m\ s^{-1}]$
B_0	Imposed magnetic field $[T]$
b	Induced magnetic field $[T]$
σ	Electrical conductivity $[\Omega^{-1} m^{-1}]$
F	Lorentz force $[N]$
k	Lorentz force calibration factor $[Nm^2 A^{-1} T^{-1}]$
λ	Magnetic diffusivity $[m^2 s^{-1}]$
μ	Magnetic permeability of vacuum $[Hm^{-1}]$
P	Pressure $[Pa]$
ν	Kinematic viscosity $[m^2 s^{-1}]$
ρ	Density $[kg\ m^{-3}]$
L	Characteristic length $[m]$
D	Plate thickness $[m]$
Q	Joule power $[W]$
τ	Advection time $[s]$
t_{diff}	Diffusion time $[s]$
$\tilde{\phi}$	Scalar potential $[V]$
T_{98}	Non-dimensional reaction time
A	Non-dimensional amplitude of the Lorentz force
$\Delta\phi$	Non-dimensional phase shift
Γ	Courant number
t_D	Discharge time constant $[s]$
U_{in}	Input signal $[V]$
U_{out}	Output signal $[V]$
$\widetilde{Lu}$	MHD analog of Lunquist number
Φ	Magnetic flux $[Wb]$
$\delta(X)$	Standard deviation
$\delta(\bar{X})$	Standard deviation of the mean
$\eta(X)$	Relative error $[\%]$
ι	Factor for magnetic field temperature dependence $[K^{-1}]$
T_{melt}	Melting temperature $[^oC]$
f_{rot}	Rotation frequency $[Hz]$
F_c	Centrifugal force $[N]$
F_d	Force experienced during braking $[N]$

t_d	Typical breaking time $[s]$
r_0	Minor radius of the torus $[m]$
R	Major radius of the torus $[m]$
W_ψ	Wavelet transform
$\psi_{b,a}$	Family of wavelet functions
f_0	Non-dimensional central frequency of the mother wavelet
W_UC	Cross-correlation function based on Wavelet transform
W_UR	Normalized cross-correlation coefficient
AW_UR	Normalized auto-correlation coefficient

Subscripts

tor	Toroidal component
pol	Poloidal component
ξ	Non-dimensional Lorentz force
ψ	Non-dimensional Joule power

Superscripts

V	Velocity based parameter
τ	Advection time based parameter
$+$	Clockwise rotation
$-$	Counter-clockwise rotation

Abbreviations

MHD	Magnetohydrodynamics
LFV	Lorentz force velocimetry
RMS	Root mean square
FT	Fourier tranform
$STFT$	Short time Fourier tranform
CWT	Continous wavelet tranform
DWT	Discrete wavelet tranform
CCF	Cross-correlation function

Special functions

$$\gamma(t, Re_{m(\tau)}, \alpha_n) = \exp\left[\frac{1-e^{-\alpha_n^2 t}}{\alpha_n^2} + \frac{e^{-Re_{m(\tau)}t}-e^{-\alpha_n^2 t}}{Re_{m(\tau)}-\alpha_n^2}\right]$$

$$\varepsilon(t, Re_{m(\omega)}, \alpha_n) = \left[Re_{m(\omega)}\sin(Re_{m(\omega)}t) + \alpha_n^2\cos(Re_{m(\omega)}t)\right]/(Re_{m(\omega)}^2 + \alpha_n^4)$$

$$\Psi(Re_{m(\omega)}, \alpha_n) = \sum_{n=0}^{\infty}\frac{Re_{m(\omega)}}{Re_{m(\omega)}^2+\alpha_n^4}/(\sum_{n=0}^{\infty}\frac{\alpha_n^2}{Re_{m(\omega)}^2+\alpha_n^4})$$

Appendix A

Technical characteristics of piezoelectric force sensor PCB 208C01

Performance	
Sensitivity	0.112 V/N
Measurement range (compression)	44.48 N
Maximum static force (compression)	270 N
Upper frequency limit	36 kHz
Non-linearity	$\leq$ 1%
Enviromental	
Temperature range	-54^oC...+ 121^oC
Temperature coefficient of sensitivity	$\leq$0.09 %/^oC
Electrical	
Discharge time tonstant	$\geq$ 50 s
Excitation voltage	18...30 VDC
Constant current excitation	2...20 mA
Physical	
Stiffness	1.05·10$^9 N/m$
Size	15.88 mm x 15.88 mm x 12.7 mm
Weight	22.7 g
Housing material	Stainless Steel

Technical characteristics of magnetic field sensor CYTHS124

Performance	
Sensitivity (in Experiments with Solid Bars)	1 mV/mT
Sensitivity (in Experiments with Sodium)	10 mV/mT
Measurement range	1 T
Non-linearity	$\leq$ 2%
Enviromental	
Temperature range	-55^oC...+ 125^oC
Temperature coefficient of sensitivity	$\leq$0.06 %/^oC
Electrical	
Control voltage	5 VDC
Consuming current	12 mA
Physical	
Size	3 mm x 3 mm x 1 mm
Weight	0.013 g
Housing Material	Plastic

Appendix B

The Python code used for Wavelet analysis.

```
def Cross_Corr_UWT(W1,W2,Q,shift_step,Smax,autosave,folder,save_step):
        '''
        W1,W2 - UWT(W1,W2)
        Smax - max decomposition level. If Smax=0: Smax - the highest possible level
        autosave - True/False
        steps - each N step to save in folder which is automatically created if it has not been done before
        '''
        N=size(W1,1)
        M=int(log2(N))
        if Smax==0: S=M-1
        else: S=Smax
        if (autosave==True):
            if not os.path.isdir(folder):
                os.makedirs(folder+'/SaveFIG')
                os.makedirs(folder+'/SaveTXT')
            temp1=0
            temp2=0
            K=zeros(S)
            for a in range(S):
                for b in range(N):
                    temp1+=W1[a][b]**2
                    temp2+=W2[a][b]**2
               K[a]=sqrt(temp1*temp2)
            for q in range(Q):
                    if (q==0):
                        Corr=zeros(S)
                        print 'Shift = %g / %g' %(q,Q)
                        for a in range(S):
                                temp=0
                                for b in range(q*shift_step,N):
                                        temp+=W1[a][b]*W2[a][b-q*shift_step]
                                Corr[a]=temp/K[a]
                        Corr_new=Corr
                    if (q>=1):
                        print 'Shift = %g / %g' %(q,Q)
                        for a in range(S):
                                temp=0
                                for b in range(q*shift_step,N):
                                        temp+=W1[a][b]*W2[a][b-q*shift_step]
                                Corr[a]=temp/K[a]
                        Corr_new=concatenate((Corr_new,Corr),axis=0)
                        Corr_shaped=reshape(Corr_new,(q+1,len(Corr)))
                        if (q%save_step==0):
                                imshow(Corr_shaped.T,aspect='auto',vmin=-1.0,vmax=1.0)
                                v = arange(-1, 1.1, 0.2)
                                colorbar(ticks=v)
                                close()
```

```
        if (autosave==False):
            temp1=0
            temp2=0
            K=zeros(S)
            for a in range(S):
                    for b in range(N):
                        temp1+=W1[a][b]**2
                        temp2+=W2[a][b]**2
                    K[a]=sqrt(temp1*temp2)
            Corr=zeros([S,Q])
            for q in range(Q):
                print 'Shift = %g / %g' %(q,Q)
                for a in range(S):
                    temp=0
                    temp1=0
                    temp2=0
                    for b in range(q*shift_step,N):
                        temp+=W1[a][b]*W2[a][b-q*shift_step]
                    Corr[a][q]=temp/K[a]
            return S, Corr
```

Listing 1: UWT-based cross-correlation coefficient

```
def UWT(x,Smax):
        x=Zero_Pad_2(x,max_power=50)
        N=len(x)
        M=int(log2(N))
        h0=[0.34, -0.09, 0.16, 0.59]
        h1=[-0.59, 0.16, 0.09, 0.34]
        if Smax==0: S=M-1 # Number of levels
        else: S=Smax
        W=zeros([S,N])
        s=0
        Mode='same'
        while s<S:
                print 'Scale = %g / %g' %(s+1,S)
                if (s==0): a=x
                d=convolve(a,h1,mode=Mode)
                a=convolve(a,h0,mode=Mode)
                W[s][:]=d
                h0=Upsample(h0)
                h1=Upsample(h1)
                s+=1
        return W
```

Listing 2: Undecimated Wavelet Transform

```
def Upsample(x):
    y=zeros(2*len(x))
    y[::2]=x
    return y
```

Listing 3: Upsampling by 2

```
def Zero_Pad_2(x,max_power):
    L=len(x)
    for i in range(max_power):
```

```
        if (2**i>=L):
            z=zeros(2**i-L)
            x=concatenate((x,z),axis=0)
            break
    return x
```

Listing 4: Zero-padding

List of Figures

List of Tables

References

[1] J. D. Jackson, *Classical Electrodynamics.* John Wiley and Sons, New York, 3rd ed., 1962. 641 pages.

[2] S. A. Balbus and J. F. Hawley, "Instability, turbulence, and enhanced transport in accretion disks," *Reviews of Modern Physics*, vol. 70, no. 1, 1998.

[3] E. Priest, *Magnetohydrodynamics of the Sun.* Cambridge University Press, Cambridge, 2014. 576 pages.

[4] H. K. Moffatt, "Electromagnetic stirring," *Physics of Fluids A*, vol. 3, no. 51, 1990.

[5] S. Takezawa, H. Tamama, K. Sugawawa, H. Sakai, C. Matsuyama, and H. .Morita., "Operation of the thruster for superconducting electromagnetohydrodynamic propulsion ship YAMATO1," *Bulletin of the M.E.S.J.*, vol. 23, no. 1, p. 46, 1995.

[6] J. A. Shercliff, *The theory of electromagnetic flow-measurement.* Cambridge University Press, Cambridge, 1962. 146 pages.

[7] C. Rashleigh and R. Marshall, "Electromagnetic acceleration of macroparticles to high velocities," *Journal of Applied Physics*, vol. 49, no. 4, p. 2540, 1978.

[8] P. A. Davidson, *An Introduction to Magnetohydrodynamics.* Cambridge University Press, Cambridge, 2001. 452 pages.

[9] T. Alboussie'‘re, P. Cardin, F. Debray, P. Rizza, J.-P. Masson, F. Plunian, A. Ribeiro, and D. Schmitt, "Experimental evidence of alfven wave propagation in a gallium alloy," *Physics of fluids*, vol. 23, no. 096601, 2011.

[10] J. A. Shercliff, *A Textbook of Magnetohydrodynamics.* Pergamon Press, 1 ed., 1965. 265 pages.

[11] J. R. Reitz and L. C. Davis, "Force on a rectangular coil moving above a conducting slab," *Journal of Applied Physics*, vol. 43, no. 1547, 1972.

[12] N. Barber and M. Longuet-Higgins, "Water movements and earth currents; electric and magnetic effects," *Nature*, vol. 161, p. 192, 1948.

[13] A. Thess, E. Votyakov, and Y. Kolesnikov, "Lorentz force velocimetry," *Physical Review Letters*, vol. 96, no. 164501, 2006.

[14] S. Gorlin and I. Slezinger, *Aeromekhanicheskie izmereniia.* Nauka, Moscow, 1964. 720 pages.

[15] R. J. Adrian, "Particle-imaging techniques for experimental fluid mechanics," *Annual Review of Fluid Mechanics*, vol. 23, pp. 261–304, 1991.

[16] A. W. amd C. Diethold, M. Werner, C. Resagk, T. Frhlich, B. Halbedel, and A. Thess, "Flow rate measurement of weakly conducting fluids using lorentz force velocimetry," *Measurement Science and Technology*, vol. 23, no. 105307, p. 6, 2012.

[17] R. Klein, C. Weidermann, X. Wang, M. Gramss, A. Alferenok, A. Thieme, Y. Kolesnikov, C. Karcher, and A. Thess, “Lorentzkraft-anemometrie fur die berhrungslose durchflussmessung von metallschmelzen, tm-technisches messen,” *Technisches Messen*, vol. 79, no. 9, p. 395, 2012.

[18] O. Reynolds, “An experimental investigation of the circumstances which determine whether the motion of water shall be direct or sinous, and of the law of resistances in parallel channels,” *Philosophical Transactions of the Royal Society*, vol. 174, pp. 925–982, 1883.

[19] C. Weidermann, *Design and laboratory test of a Lorentz force flowmeter for pipe flows.* PhD thesis, Ilmenau University of Technology, 2013.

[20] J. Crank, *The Mathematics of Diffusion.* Oxford University Press, Oxford, 2 ed., 1975. 414 pages.

[21] H. S. Carslaw and J. C. Jaeger, *Conduction of heat in solids.* Clarendon Press, Oxford, 2 ed., 1959.

[22] C. Weidermann, A. Thess, D. Lieftucht, and M. Reifferscheid, “Application of lorentz force velocimetry in continuous casting of steel,” in *Proceedings of the 5th International Congress on the Science and Technology of Steelmaking*, 2012.

[23] F. John, *Partial Differential Equations.* Springer-Verlag, New York, 1 ed., 1982.

[24] J. W. Thomas, *Numerical Partial Differential Equations: Finite Difference Methods.* Springer US, 2 ed., 1998. 460 pages.

[25] P. H. Roberts, *An Introduction to Magnetohydrodynamics.* Longmans, London, 1967. 264 pages.

[26] K. Halbach, “Design of permanent magnets with oriented rare earth cobalt material,” *Nuclear Instruments and Methods*, vol. 169, pp. 1–10, 1979.

[27] J. Dally, W. Riley, and K. McConnell, *Instrumentation for engineering measurements.* Oxford University Press, Oxford, 2 ed., 1993. 608 pages.

[28] I. Sokolov, Y. Kolesnikov, and A. Thess, “Experimental investigation of the transient phase of the Lorentz force response to the time-dependent velocity at finite magnetic Reynolds number,” *Measurement Science and Technology*, vol. 25, no. 12, p. 125304, 2014.

[29] V. G. Vasil’ev, B. G. Karasev, and I. V. Lavrent’ev, “Experimental investigation of a dc mhd-generator,” *Magnetohydrodynamics*, vol. 5, no. 3, pp. 101–103, 1967.

[30] V. Noskov, S. Denisov, P. Frick, S. Khripchenko, D. Sokoloff, and R. Stepanov, “Magnetic field rotation in the screw gallium flow,” *The European Physical Journal B*, vol. 41, pp. 561–568, 2004.

[31] D. J. Griffits, *Introduction to Electrodynamics.* Pearson, USA, 4th ed., 2013. 589 pages.

[32] J. R. Taylor, *An Introduction to Error Analysis.* University Science Books, USA, 2nd ed., 1996. 327 pages.

[33] R. H. Dieck, *Measurement Uncertainty: Methods and Applications.* Instrument Society of America, 4th ed., 2006. 277 pages.

[34] Y. Kolesnikov, C. Karcher, and A. Thess, "Lorentz force flowmeter for liquid aluminum: Laboratory experiments and plant tests," *Metallurgical and Materials Transactions B*, vol. 42B, no. 441, 2011.

[35] A. Thess, E. Votyakov, B. Knaepen, and O. Zikanov, "Theory of the Lorentz force flowmeter," *New Journal of Physics*, vol. 9, p. 299, 2007.

[36] X. Wang, Y. Kolesnikov, and A. Thess, "Numerical calibration of a Lorentz force flowmeter," *Measurement Science and Technology*, vol. 23, p. 045005, 2012.

[37] A. Gailitis, O. Lielausis, E. Platacis, G. Gerbeth, and F. Stefani, "The riga dynamo experiment," *Surveys in Geophysics*, vol. 24, pp. 247–267, 2003.

[38] P. Frick, V. Noskov, S. Denisov, S. Khripchenko, D. Sokoloff, R. Stepanov, and A. Sukhanovsky, "Non-stationary screw flow in a toroidal channel: Way to a laboratory dynamo experiment," *Magnetohydrodynamics*, vol. 38, no. 1-2, pp. 143–162, 2002.

[39] V. Noskov, S. Denisov, R. Stepanov, and P. Frick, "Turbulent viscosity and turbulent magnetic diffusivity in a decaying spin-down flow of liquid sodium," *Physical Review E*, vol. 85, p. 016303, 2012.

[40] I. K. Kikoin, *Tablici Fizicheskich Velichin.* Atomizdat, Moscow, 1976.

[41] H. Kamkar and H. K. Moffat, "A dynamic runaway effect associated with flux expulsion in magnetohydrodynamic channel flow," *Journal of Fluid Mechanics*, vol. 121, pp. 107–122, 1982.

[42] P. Frick, V. Noskov, S. Denisov, and R. Stepanov, "Direct measurement of effective magnetic diffusivity in turbulent flow of liquid sodium," *Physical Review Letters*, vol. 105, p. 184502, 2010.

[43] R. Stepanov, R. Volk, S. Denisov, P. Frick, V. Noskov, and J.-F. Pinton, "Induction, helicity, and alpha effect in a toroidal screw flow of liquid gallium," *Physical Review E*, vol. 73, p. 046310, 2006.

[44] F. Cattaneo and S. M. Tobias, "On large-scale dynamo action at high magnetic reynolds number," *Astrophysical Journal*, vol. 789, no. 70, 2014.

[45] P. Bradshaw, *An introduction to turbulence and its measurement.* Pergamon press, Oxford, 1971.

[46] A. V. Oppenheim and R. W. Schafer, *Discrete-Time Signal Processing.* Pearson Education Limited, pearson new international edition ed., 2013.

[47] I. Daubechies, *Ten Lectures on Wavelets.* Society for Industrial and Applied Mathematics, 1992.

[48] S. Mallat, *A Wavelet Tour of Signal Processing: The Sparse Way.* Elsevier Ltd, Oxford, 2009.

[49] J. C. Goswami and A. K. Chan, *Fundamentals of Wavelets: Theory, Algorithms, and Applications.* John Wiley & Sons, 2011.

[50] P. S. Addison, *The Illustrated Wavelet Transform Handbook: Introductory Theory and Applications in Science, Engineering, Medicine and Finance.* CRC Press, 2002.

[51] T. Lee, "Image representation using 2d Gabor wavelets," *IEEE Transactions on Pattern Analysis and Machine Intelligence*, vol. 18, no. 10, 1996.

[52] C. H. Yuan, F. Zheng, and S. C. Ahalt, "Object tracking using the Gabor wavelet transform and the golden section algorithm," *IEEE Transactions on Multimedia*, vol. 4, no. 4, 2002.

[53] K. L. Mak, P. Peng, K. F. C. Yiu, and L. K. Li, "Multi-dimensional complex-valued Gabor wavelet networks," *Mathematical and Computer Modelling*, vol. 52, no. 10, 2013.

[54] J. Daugman, "Information theory and coding, University of Cambridge, Lecture notes," 2013.

[55] S. Smith, *Digital Signal Processing. A Practical Guide for Engineers and Scientists.* Elsevier Ltd, Oxford, 3rd ed., 2002.

[56] Y. Mizumo-Matsumoto, S. Ukai, R. Ishii, S. Date, T. Kaishima, K. Shinosaki, S. Shimojo, M. Takeda, S. Tamura, and T. Inouye, "Wavelet-crosscorrelation analysis: non-stationary analysis of neurophysiological signals," *Brain Topography*, vol. 17, no. 4, 1995.

[57] N. Yokoi and G. Balarac, "Cross-helicity effects and turbulent transport in magnetohydrodynamic flow," *Journal of Physics: Conference Series*, vol. 318, p. 072039, 2011.

Acknowledgments

The work has been done in the framework of the Project A1 in the Research Training Group 1567 "Lorentz force velocimetry and Lorentz force eddy current testing" supported by Deutsche Forschungsgemeinschaft (DFG).

The actual research would never have been successfully conducted within three years without contributions of the following people. I would like to thank **Prof. André Thess** who has initiated and then supervised my work by giving valuable advices and setting the most important research directions. I am particularly grateful to **Prof. Yuri Kolesnikov** for countless number of times when we met together in order to tackle a problem or to discuss the obtained results. Many thanks to **Prof. Christian Karcher** whose criticism has significantly improved the quality of the research. Only the best words must be said about the colleagues from ICMM (Perm) who I planned and conducted the liquid sodium experiment with. I highly appreciate the efforts of **Prof. Peter Frick** who helped to resolve the organizational issues of the experiment in Perm. I would also like to express my gratitude to **Dr. Vitaliy Noskov** who supervised my scientific stay in Perm and who was continuously coming up with extraordinary solutions of the arising engineering problems. Indeed, I want to give credit to **Alexander Pavlinov** with whom we have been sitting all day long in the lab obtaining the unique data. It is a pleasure to recognize the work done by **Daniel Martschoke**, **Christopher Hahn** and **Rudolph Stephanie** who have prepared under my supervision a solid piece of the experimental equipment for the sodium experiment. I also wish to thank **Alexander Thieme** for his help in the Halbach array assembling and **Dr. Rico Klein** for inspiring me during hard moments. And it goes without saying that I am indebted to our administration office represented by **Colette Hentsch** and **Cindy Karcher** who helped me a lot with the paper work.